Submillimeter wave camera using a novel photon detector technology

A Thesis
Presented to
The Academic Faculty

by

Shwetank Kumar

In Partial Fulfillment
of the Requirements for the Degree
Doctor of Philosophy

School of Applied Physics
California Institute of Technology
Pasadena, California
2007
(Defended December 13, 2007)

Long fellow की कविता Psalm of life का[a] हिन्दी रूपान्तर

मत कहो मुझे यह शुष्क वंचन,
जीवन सपने की छाया है ।
आत्मा प्रसुप्त है आत्मा मृत
जग का स्वरूप भ्रम माया है ।।

जीवन है सत्य जीवन है सार,
मृत्यु ही नहीं इसका अन्त न लक्ष्य ।
नाशवान है है क्षण भंगुर,
आत्मा के प्रति है नहीं सत्य ।।

हर्ष ही नहीं शोक भी नहीं ,
इस जीवन का लक्ष्य निरन्तर ।
बन कर्मवीर अरू हो अग्रसर,
प्रति पल प्रतिदिन प्रगति पथ पर ।।

काल गति तीव्र गन्तव्य अति दूर,
हृदय हमारे सशक्त अरू महान ।
धक धक करते रहते फिर भी,
मरघट को शव करता प्रयाण ।।

विश्व के विशाल रण आंगन में
जीवन शिविर के खुले मैदान में।
मूक पशु मत बन भव वीर विजयी,
जीवन के हर अभियान में ।।

[a] Translation of The Psalm of Life by W.H. Longfellow to Hindi by my grandfather Sri. Ram Chand Bhatia. (Printed with permission)

भविष्य पर मत करो भरोसा
है अतीत की चिंता व्यर्थ ।
वर्तमान ही जीवन है
आश्वस्त हो हो कर्मरत ।।

महापुरूषों की जीवन गाथा,
प्रेरित करती हम बनें महान।
काल रेती पर छोड़ चलें हम,
निज चरणों के अमिंट निशान ।।

कालान्तर में जीवन पथ पर,
कोई दीन और असहाय ।
लख चिन्ह तुम्हारे चरणों के,
पथ भ्रष्ट पथिक पथ पा जाय।।

तदुत्तिष्ठ अरू हो कटिबद्ध,
हर नियति से संघर्ष हेतु ।
कुछ पाता चल और बढ़ता चल,
धर धीरज उत्कर्ष हेतु ।।

राम

ACKNOWLEDGEMENTS

I am truly privileged to have worked with Prof. Jonas Zmuidzinas for my PhD. Jonas' clarity of thought as he approaches science is simultaneously inspirational and humbling. His commitment as a mentor is unparalleled and I will never forget the day he walked into my candidacy exam with an IV stuck to his arm to ensure that he was there for me. I have learnt much from him – science and how to do it well – and hope to continue to do so in future.

This thesis would not be possible without the other members of my research group. I would like to thank Dr. Peter Day who was a great support for me as a co-advisor when Jonas was away. I appreciate Dr. Rick Leduc's inputs on mask designing and fabrication of the devices. Dr. Ben Mazin's work helped in gathering noise data on niobium resonators. Useful discussions with Dr. Megan Eckart helped me in clarifying many detector concepts. Many of the photon detector experiments were carried out with Tasos Vayonakis, who is by far the most meticulous experimentalist I have encountered and I have learnt much from him.

I would like to thank Dr. Simon Radford and my thesis committee, comprising of Dr. David Rutledge, Dr. Marc Bockrath, and Dr. Axel Scherer, for useful suggestions on my thesis.

One of the most memorable parts of my PhD was spent at the IBM Research Center in the summer of 2007 where I found new friends and mentors – Dr. Stuart Parkin, Dr. Mike Gaidis, Dr. Masamitsu Hayashi, and Dr. Rai Moriya. I appreciate Mike nudging me to take up a summer internship in Stuart's group, and candid discussions with him gave me important insights into the nature of industrial research. Stuart has the most contagious enthusiasm for science, and working with him was

really a turning point in my choice of what I wanted to do after my PhD. Masa and Rai taught me a great deal about magnetics. Their understanding of the subject and its issues is unparalleled and I appreciate learning from these gifted experimentalists.

I want to thank my high school friends – especially Nidhi, Neha, and Manish – who have stuck with me through the highs and lows in my career and even on occasion, pretended to feign interest in my research. All my friends at Caltech – especially Meher, Jeff, Chip, Vikram, Nachiket, Uday, Mayank, Prabha, Saha, Sukhada, Pinkesh, and Mansi – made my time here very memorable. Many useful suggestions to the thesis were made by Mansi, Varun and Matt Ferry. I want to thank Dr. Carlo Callegari from whom I learnt a lot, both academically and non-academically, in the early part of my PhD work.

Through the entire time my extended family has been an unwavering source of support and love. I am indebted to the members of Multanimafia for their constant words of encouragement: My cousin sister Kriti was often on the other end of the phone on my bad days. Rohit, my co-beacon of uncertainty has always been no more than a phone call away as well day or night and has tolerated, learnt from, and taught me esoteric jokes. I would not have made it very far without him. Toshi, my dearest sibling whose importance in my life is immeasurable – at some level the only one who truly gets me. My parents have been an endless source of love and encouragement for me. I have learnt much from dad about science, religion, philosophy, and arts in our endless late-night conversations. I hope one day I can match a fraction of his knowledge and wisdom. Mum has showered me with unselfish love and made many a sacrifice so that I had the freedom to do what I so wanted to. Their love has truly been the scaffolding on which my dreams and this thesis have taken shape.

ABSTRACT

Cryogenic photon detectors can be used to make extremely sensitive cameras for submillimeter astronomy. Current detector technologies already have sensitivities limited by the noise due to photon arrival statistics. To further improve the sensitivity and mapping speed of experiments for a wide field survey, focal planes containing tens of thousands of pixels are required. Unfortunately, the current technologies use discrete and massive components which are not easy to integrate into large arrays. This thesis presents a 16-pixel, two-color, submillimeter-wave, prototype camera developed at Caltech and the Jet Propulsion Laboratory using a novel photon detector technology. The camera also uses new designs for other constituent elements – the antenna, transmission line feednetwork, and bandpass filters – to implement the submillimeter pixels. These designs allow integration of the entire camera onto a single chip and conclusively address the problem of scalability while maintaining the sensitivity and noise performance of the current technologies. This thesis explains the design of each of these components and presents the results from experiments conducted to test their performance. Results from the 'first light', obtained by mounting the prototype camera onto the Caltech Submillimeter Observatory (CSO), are also presented.

We have also studied the temperature and power dependence of the resonance frequency, quality factor, and frequency noise of the superconducting niobium thin-film coplanar waveguide (CPW) resonators in order to understand the factors affecting the noise performance of our photon detectors. These experiments were carried out at temperatures well below the superconducting transition ($T_c = 9.2$ K) in an attempt to understand the source of the excess frequency noise of superconducting resonators

which form the sensing element of our photon detectors. The noise decreases by nearly two orders of magnitude as the temperature is increased from 120 to 1200 mK, while the variation of the resonance frequency with temperature over this range agrees well with the standard two-level systems (TLS) model for amorphous dielectrics. These results support the hypothesis that TLS are responsible for the noise in superconducting microresonators and have important implications for resonator applications such as qubits and photon detectors.

TABLE OF CONTENTS

LIST OF TABLES

LIST OF FIGURES

CHAPTER I

INTRODUCTION

1.1 Motivation – Submillimeter Astronomy

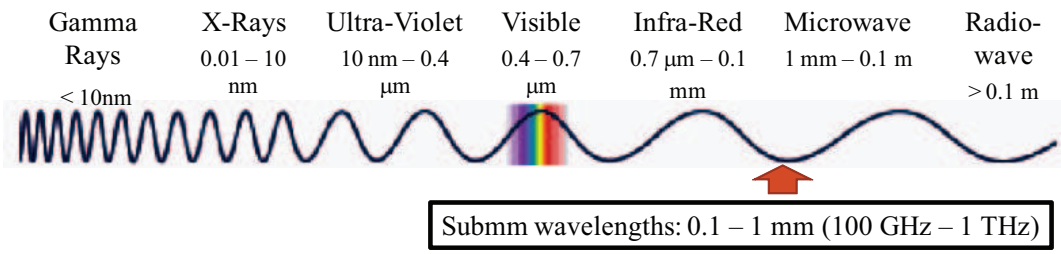

Figure 1.1: The electromagnetic spectrum

Astronomy has historically been dominated by observations in the optical part of the electromagnetic spectrum. There are various reasons why the optical frequency range has been the most extensively studied for centuries [1, 2, 3]. The instrumentation for this band has existed for a long time: The earliest photon detectors were naked eyes, and Galileo used the optical telescope for astronomy for the first time in the 17^{th} century. It is easy to do ground-based astronomy in this band since the Earth's atmosphere is transmissive at these frequencies. However, a strong case can be built for submillimeter astronomy as well, since the Earth's atmosphere is partially transmissive at microwave/radio, submillimeter, and infrared (IR) wavelengths [2]. Furthermore, the optical frequencies form a small part of the entire electromagnetic spectrum (Figure 1.1). They extend from 0.4 μm to 0.7 μm which is less than a decade, while the radio-frequency (RF)/microwave, and submillimeter part of the frequency spectrum extends over many decades (with the submillimeter part of the spectrum extending over a decade, from 100 GHz to 1 THz) [1]. In the past it has been

difficult to do astronomy at submillimeter wavelengths because of the opacity due to water lines in the Earth's atmosphere and lack of high-performance instruments. The problem of opacity due to water lines can be solved by doing ground-based astronomy from high altitude ($\sim$ 14,000 ft), dry regions such as Mauna Kea, where the Caltech Submillimeter Observatory (CSO) is located. The instrumentation and techniques that already exist for the microwave/RF and optical frequency range can not be readily adapted to the submillimeter band.

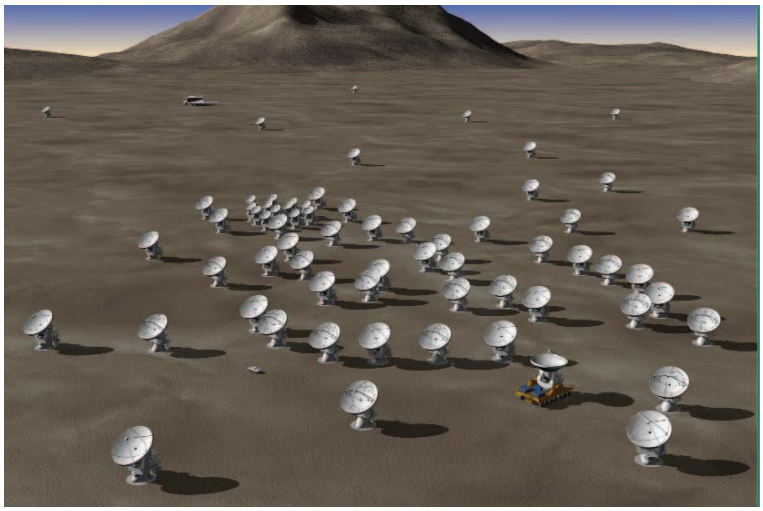

Figure 1.2: Concept view of ALMA (Credit: http://www.eso.org/projects/alma/)

However past two decades have seen tremendous progress in the performance of submillimeter detectors [4, 5] and these changes are ushering in major investments such as the Atacama Large Millimeter Array (ALMA) (Figure 1.2) interferometer and the Caltech Cornell Atacama Telescope (CCAT) (Figure 1.3). ALMA is a $1 billion project which will have very high angular and spectral resolution (30" at 1.3 mm) and will be able to make exquisite images of very small fields [6]. CCAT on the other hand will be a 25 m diameter, high-sensitivity, wide-field-of-view and a broadband telescope [7], and will provide capability for deep, multi-color, wide field surveys which will help choose targets for more detailed follow-ups with ALMA. With these

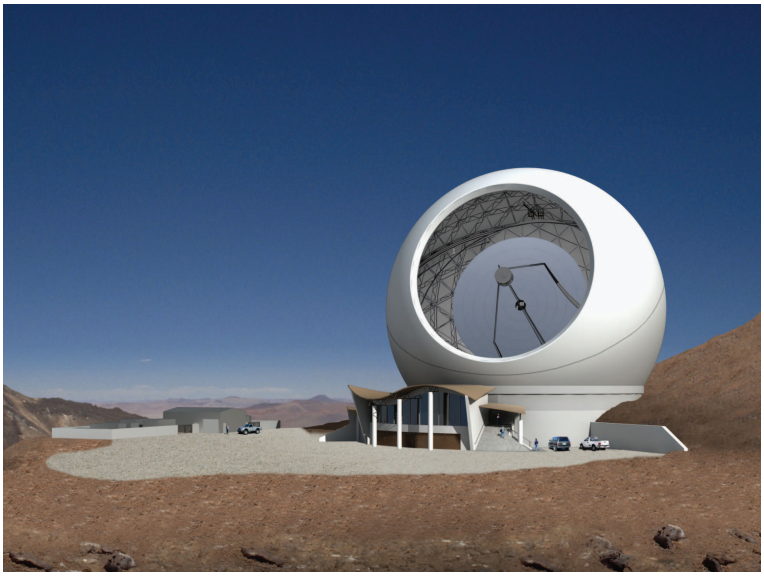

Figure 1.3: Concept view of CCAT at 5600 m on the candidate site near the summit of Cerro Chajnantor, Chile (Credit: M3Engineering)

new technologies, as past experience has shown us, we should expect new, groundbreaking science which will further our understanding of the universe.

Scientifically, the submillimeter band is interesting because some very important astronomical sources radiate strongly at these wavelengths – such as the Cosmic Microwave Background (CMB) radiation, the probing of which can give us deep insights into the beginning, structure, and dynamics of the universe. There are various foreground sources of submillimeter radiation – submillimeter galaxies, regions of very active star formation, and galaxy clusters that can be studied using Sunyaev-Zel'dovich Effect (SZE). In the next section we discuss the science objectives for studying these sources to motivate the development of novel instrumentation at these frequencies.

1.2 Scientific Case for Novel Submillimeter Instrumentation

1.2.1 Submillimeter Galaxies

Figure 1.4 shows an image of the Antennae (NGC 4038/4039) galaxies in the visible, infrared, and submillimeter. These are two low redshift spiral galaxies colliding with each other. In general, such a collision triggers a gravitational collapse resulting in a massive burst of star formation in the region of their interaction. However, the new stars being formed are deep inside molecular clouds and are enshrouded in dust which is opaque to optical frequencies. This prevents us from studying the actual interaction in this band. At longer wavelengths however, the dust becomes transparent since optical depth depends inversely on the wavelength. This allows us to observe the interaction at infrared (IR) and submillimeter wavebands (Figure 1.4 b), c)). Further, the dust in the region reprocesses the light in the optical band – i.e., it absorbs optical wavelengths and re-emits them in IR and submillimeter, thereby increasing the luminosity in these bands. From Figure 1.5, taken using the Spitzer satellite [8], it is evident that there is as much energy in the starlight in cosmic optical background as there is in star light that has been reprocessed by interstellar dust shown in cosmic infrared background making a strong case for observations in these bands.

Recent studies have also shown that in general even dust–corrected UV/optical data do not accurately reflect the bolometric luminosities of the submillimeter galaxies when compared with RF and submillimeter observations [9]. These luminosities can be underestimated by a median factor as much as two orders of magnitude [10]. This has major implications for studying galaxy interactions and star formation models.

Another motivation for doing galaxy surveys in submillimeter bands is that the surveys done using SCUBA have detected a very large number of submillimeter galaxies at very high redshifts [10], hence very early times. This supports a hierachical

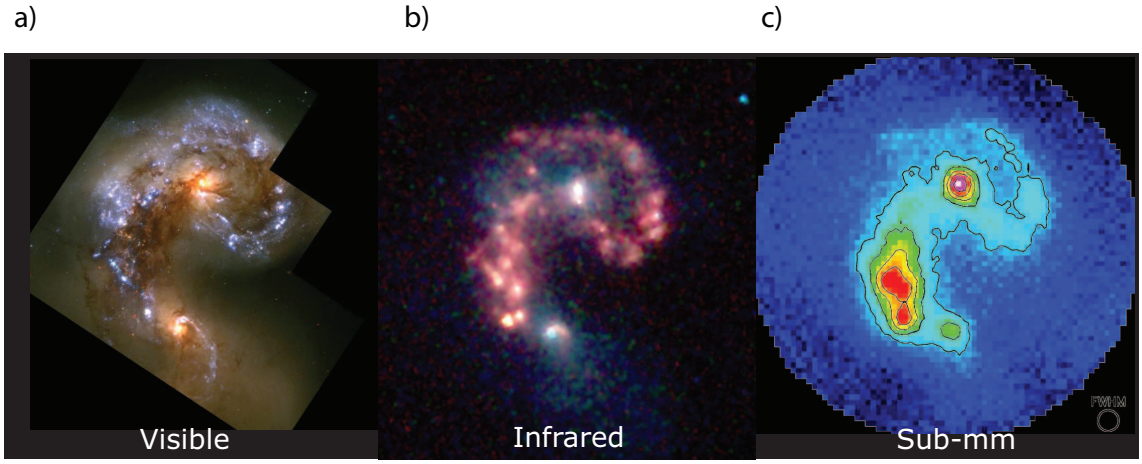

Figure 1.4: Images of the Antennae (NGC 4038/4039) in the visible (left), infrared (center), and submillimeter (right) (Credits: visible [HST,WFPC2], infrared [Spitzer, IRAC], and submillimeter [CSO, SHARC])

model for development of structure in the universe in which galaxy mergers such as those mentioned above are very important and are a major source of star formation. The observed luminosity function, which gives number density of galaxies as a function of luminosity (Figure 1.6), is far larger than what is predicted by the models tuned to explain the observations in the optical bands. These galaxy formation models have needed dramatic changes, including changes in treatment of dark matter halos and galaxy mergers [11], in order to explain the observations in the submillimeter band. To further test the new models incisively, it is required that we probe the high-redshift tail of the galaxy population simultaneously in multiple frequency bands in the submillimeter part of the spectrum.

A major astronomical challenge that may be addressed by simultaneous multiband measurements in the submillimeter is characterization of dust emissivity properties. The dust emissivity in this band is dominated by large grains in thermal equilibrium which are characterised by a temperature and spectral dependence of emissivity modeled simply by an index (β). This characterization is essential to estimate redshifts using radio and submillimeter flux measurements. Since the accuracy

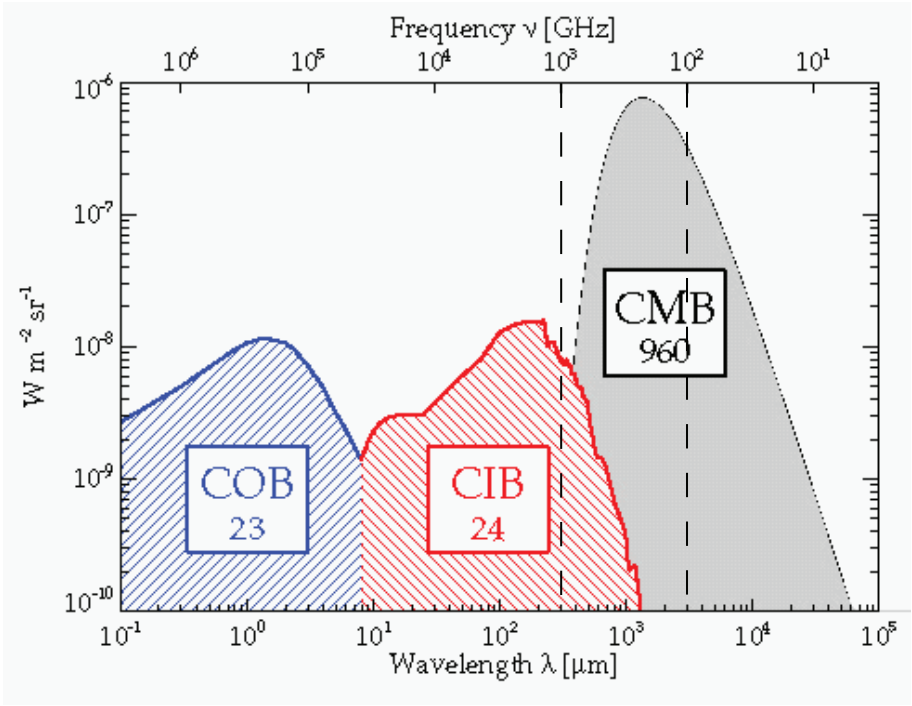

Figure 1.5: Power spectrum of Cosmic Optical, Infrared, and Microwave Background from observations using the instrumentation on Spitzer satellite [8]. The frequency band between the dashed line shows the submillimeter range.

and precision of β are unknown, measuring it for a large sample of galaxies with low redshifts and varying properties – so that the observations are on the Rayleigh-Jeans (RJ) side of the thermal spectral emission density (SED) – will yield its intrinsic dispersion. This will allow us to assign systematic uncertainties to β, hence quantifying systematic uncertainties in the dust temperature and redshift.

1.2.2 Milky Way Galactic Plane Survey

Galactic plane surveys have been undertaken by many teams – specifically using the SCUBAII instrument on the James Clark Maxwell Telescope (JCMT), and Bolocam on CSO. The science goals of these projects are to measure the galaxy-wide rates of star formation, efficiency, triggers, evolution, and timescales of young massive stars [7]. This would obtain the complete inventory of hot and cold dust in the galactic plane. Combining this data with optical, radio, and IR data sets will determine

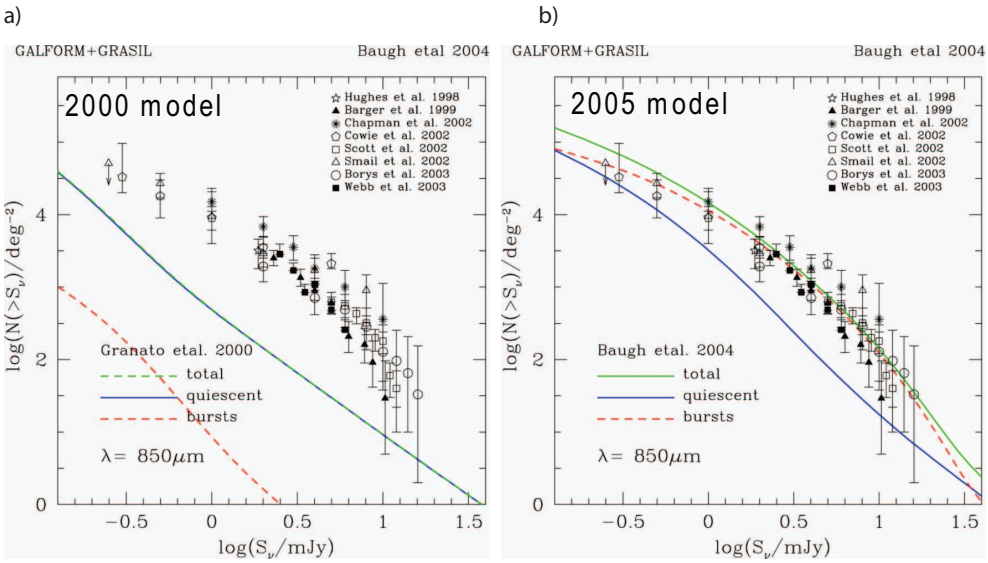

Figure 1.6: Plots of number density vs luminosity with fits based on models constructed (a) without and (b) with submillimeter survey data [11]

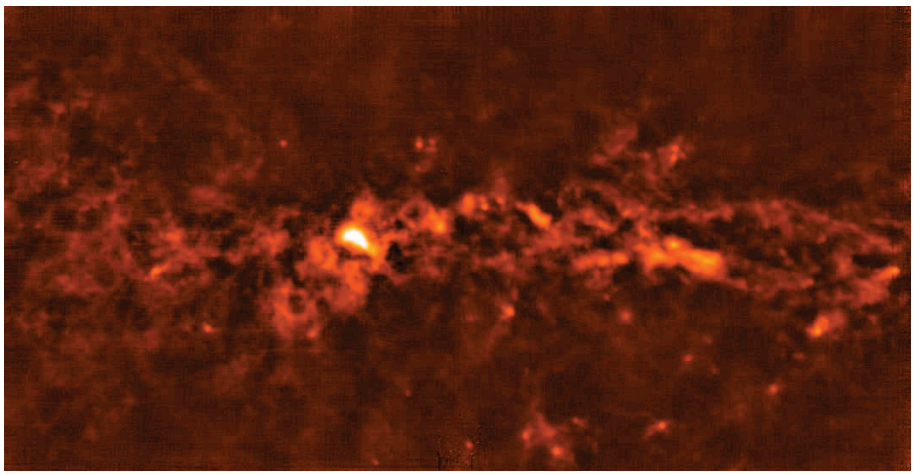

Figure 1.7: An image of the galactic plane using Bolocam in the 1.1 mm wavelength band. The image dimensions are $2^\circ \times 1^\circ$ with the field of view centered at a Galactic longitude of l = 0.5°, latitude b=0°. It contains the Sgr A complex on the right, and Sgr B2 star–forming complex in the left half of the image. (Credits: Dr. John Bally and the Bolocam Galactic Plane Survey Team)

the relative importance of different mechanisms of star formation and their dependence on properties of the inter-stellar medium [7]. Following up these measurements

across the submillimeter band from 350 μm to 1.4 mm will allow sampling of spectral energy distributions to measure bolometric luminosities, dust temperatures, and masses robustly. This would allow testing the hypothesis that the long wavelength spectral emissivity index β can change significantly with temperature. Simultaneous multi-color data would prove to be invaluable for this science.

1.2.3 Sunyaev-Zel'dovich Effect (SZE) Measurements

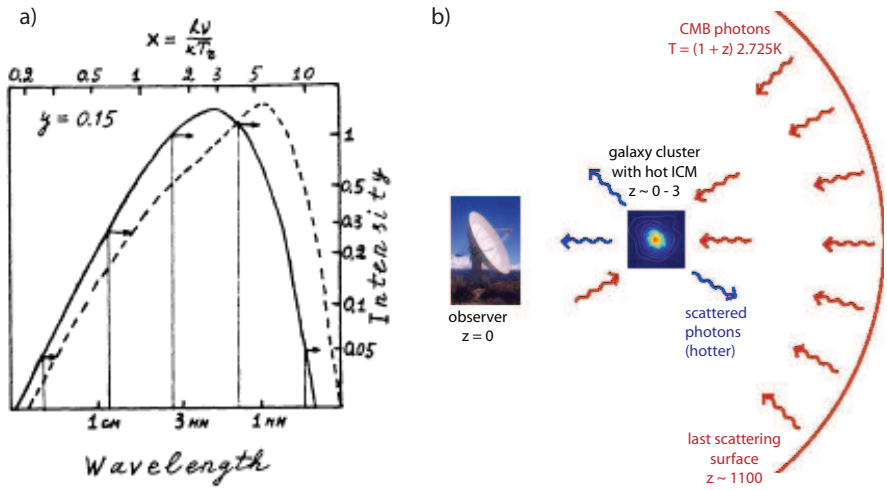

Figure 1.8: a) Original and the shifted spectrum of the CMB photons due to SZ scattering off of the hot interstellar gas. b) Figure illustrating the SZ effect (Credit: Dr. Sunil Golwala)

The Cosmic Microwave Background (CMB) radiation was discovered in 1964 by Wilson and Penzias and is regarded as the most conclusive piece of evidence for the Big Bang Model. In 1989 the COBE satellite measured the CMB and showed that it has a blackbody spectrum with temperature of 2.725 K to 1 part in 10^5 while measuring its primary anisotropies. In 1970, Sunyaev and Zel'dovich predicted that the CMB power spectrum would have secondary anisotropies due to what is now known as Sunyaev-Zel'dovich Effect (SZE). This refers to the Thomson scattering of Cosmic Microwave Background (CMB) photons by hot electrons in the intracluster

medium. This transfers some of the energy from the ionized gas to the CMB photons while conserving the photon number (upscattering). While the effect itself is small and of low probability ($\sim$ 1%), it leads to a measurable change in the frequency spectrum of the radiation and makes it non-thermal, so it effectively seems colder at long wavelengths and hotter at short wavelengths. The temperature shift independent of redshift is given by:

$$\frac{\Delta T_{SZE}}{T_{CMB}} = f(x)y = f(x) \int n_e \frac{kT_e}{m_e c^2} \sigma_T dl \tag{1.1}$$

where $n_e/m_e/T_e/p_e$ are electron density/mass/temperature/pressure, σ_T is the Thomson scattering cross section, k is the Boltzmann constant, c is the speed of light, $dl = cdt$ is the distance along the photon path through the cloud, and $f(x)$ is the spectral dependence with $x = h\nu/kT$. The photon energies get boosted by $\frac{kT_e}{m_e c^2}$, which for temperatures 10^8 K can lead to relativistic increase in the energy. Since the ratio $\Delta T_{SZE}/T_{CMB}$, or equivalently the surface brightness of SZE, is redshift independent it is a powerful way to detect massive clusters at any redshift as long as the experiment has sufficient angular resolution. There is also a second-order kinetic SZE where the CMB photons interact with the electrons that have high energies due to their bulk motion compared to the rest frame of CMB photons.

These effects can be used to constrain cosmological models and probe universal constants in several different ways. Combined with X-ray cluster studies which probe the emission measure of intracluster gas, SZE studies can be used to precisely determine the Hubble constant H_0 and the deceleration parameter q_0 [9, 12]. The SZE combined with the X-ray estimates of gas temperature can be used to estimate the baryonic mass fraction in the galaxy cluster [13]. Using SZE to detect distant clusters allows us to study the large-scale structure and cosmological parameters describing the universe – and might even be useful in constraining the dark matter equation of state [12].

Kinetic SZE can be used to determine the cluster peculiar velocity [13]. These measurements need to be made in the submillimeter band close to 150 GHz to measure the SZ decrement or at 275 GHz to measure the SZ increment. Multi-color capabilities in other bands will be useful for removing the atmospheric noise for increased sensitivity and removing contaminants such as point sources. The next section lists characteristics required in the instrumentation to meet these science goals.

1.3 Instrumentation

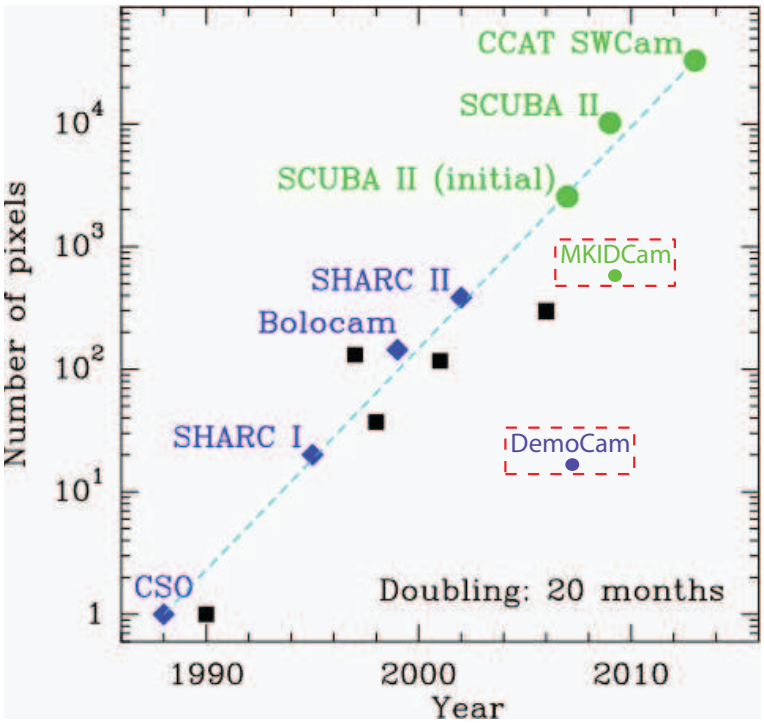

Figure 1.9: The increase in pixel count of almost background limited bolometric submillimeter camera technologies over the past 20 years is seen to follow Moore's law. Also shown in the dotted red boxes are the DemoCam discussed in this thesis and future generation MKIDCam that will complement and compete with SCUBAII using kinetic inductance detector technology [14, 15, 16, 17].

Nearly background limited bolometric submillimeter camera technologies have followed Moore's law (Figure 1.9) and doubled in array size roughly every 20 months or so. Current state of the art is defined by SCUBA at JCMT and Bolocam and

SHARCII at CSO (Figures 1.10, 1.11). These cameras have contributed significantly to our scientific knowledge through galactic plane surveys [18, 19], surveys of submillimeter galaxies [20, 10, 21], and SZE observations [22]. However, these cameras have a few hundred pixels and the technologies being used to implement them are difficult to scale to larger array sizes. Future scientific missions motivated in Sections 1.2.1, 1.2.2 and 1.2.3 will require cameras with tens of thousands of background limited multi-color pixels, if not more.

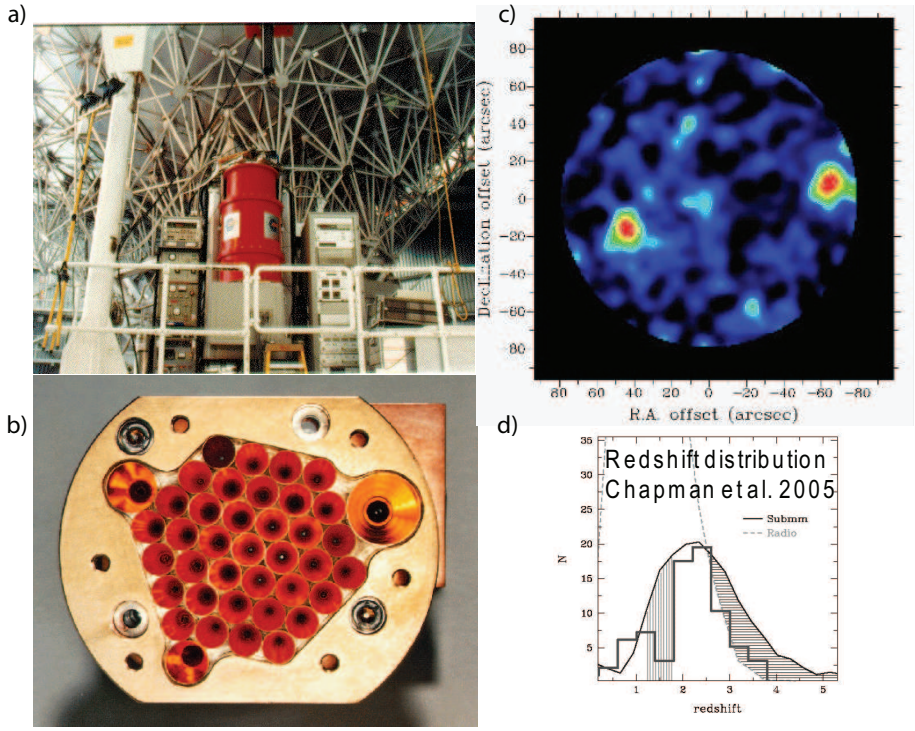

Figure 1.10: a) SCUBA instrument mounted on JCMT. b) SCUBA focal plane top view showing the input feedhorn antenna. c) Maps of submillimeter galaxies detected using SCUBA instrument. d)The redshift histogram of submillimeter galaxy sample observed using SCUBA [10]

Since it is difficult to scale current technologies to those sizes, new technologies need to be developed making it feasible to construct large pixel arrays which allow all the components of a submillimeter camera to be integrable onto a monolithic chip so that scaling is not an issue.

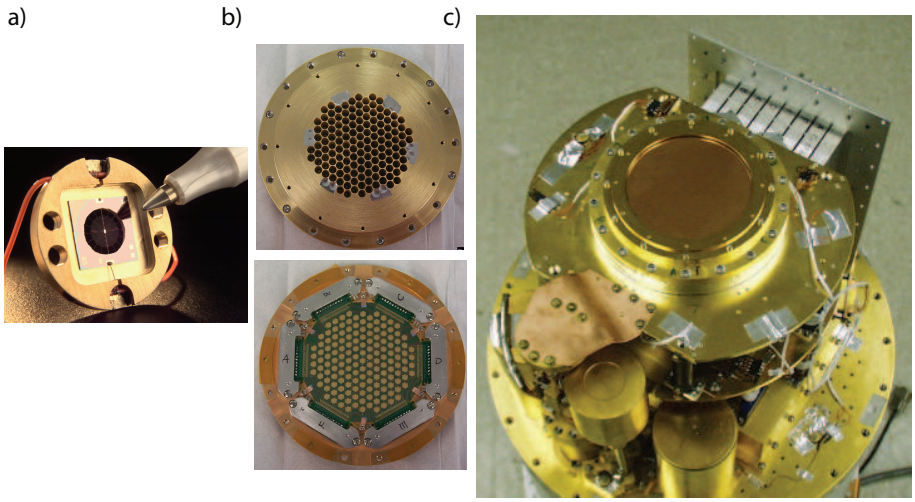

Figure 1.11: a) Bolocam detector b)Bolocam focal plane showing feeds (top) and detectors (bottom) c) Bolocam camera mounted in the dewar with metal mesh filter on the top

This thesis presents a 16-pixel, 2-color camera (DemoCam) which we have designed, implemented and tested. This camera uses novel, planar technologies for pixel components – the antenna, feed network, bandpass filter, and photon detector that allow for the entire camera to be fabricated on a single chip, thereby conclusively addressing the problem of scalability photolithographically while maintaining the sensitivity and noise performance of the other current technologies. Data can be gathered in both the bands simultaneously for all the 16 pixels. The future generations (MKIDCam) will be able to operate simultaneously in all four submillimeter bands (Chapter 4), which is essential for attaining future scientific goals. MKIDCam will be a superior replacement for Bolocam as a facility instrument at the CSO and will have comparable raw mapping speed to SCUBAII, mounted on JCMT, while costing about an order of magnitude lesser. SCUBAII will operate with only two colors, out of which only one will be regularly usable.

Future cameras for CCAT after MKIDCam will have tens of thousands of pixels that will completely cover the telescope field of view (20') which is necessary to make use of its focal plane efficiently. The mapping speed of the instrument increases

linearly with the pixel count. Consequently, compared to the current rate of 1 or 2 submillimeter galaxy detections per night, with MKIDCam the mapping speed will increase approximately by a factor of 6 resulting in detection of around 12 galaxies per night[23] at the CSO. This number will be dramatically higher when the same instrumentation is used on the upcoming CCAT.

Further, by using multi-color camera technologies it will be possible to ensure that the detections made are robust, for example by requiring simultaneous detection in multiple bands to rule out fake detections or omissions. Currently, monochromatic observations are used which are then followed up in different bands by separate instruments. Different instruments typically have different sensitivities and systematics and consequently lead to non-uniformity in data. This leads to discrepancies like spurious detections and omissions in data sets, especially when working close to the noise limit. Use of the multicolor cameras for a single survey will overcome this challenge in multiple ways:

1. It avoids temporal variability – changes in the response due to changes in atmospheric conditions or instrument sensitivity – between the observations.

2. Although sensitivity of the intrument may be limited by other factors such as the atmosphere, telescope quality etc. using a single camera in different bands will lead to nominally uniform detector sensitivities which will make it possible to make the survey depth more uniform at different wavelengths.

3. Systematics are easier to understand and remove between different bands from the same survey.

4. There would be nominally uniform sky coverage while looking at the same location in the sky which will make data in all bands for every covered spatial location available except for the difference in beam sizes which would make the diffraction spot size somewhat different.

Thus with simultaneous, uniformly calibrated photometry in multiple-frequency bands, these issues will be addressed robustly, and interesting candidates (e.g., high-redshift submillimeter galaxies) can be selected from the dataset for more expensive follow-ups (e.g., making detailed maps using the ALMA interferometer).

1.4 Thesis Outline

This thesis presents a 16-pixel, two-color camera implemented using novel planar technologies for the pixel subcomponents - the antenna, submillimeter feed networks and waveguide and the photon detector, that integrate the entire camera on to a single chip. The design is scalable to large arrays even as it maintains the performance metrics of single pixels of current technologies. In Chapter 2 of this thesis we discuss results of noise, resonance frequency and quality factor measurements of superconducting resonators as a function of temperature and readout power of these devices. These are of interest since superconducting microresonators form the sensing element of the photon detectors used in our pixels and understanding the source and mechanism of this noise will allow us to optimize our detectors for better perfomance. Chapter 3 presents the design details of each sub-component (except the bandpass filter) of a single pixel and discusses the measurement setup and results. Chapter 4 details the design of the on-chip bandpass filters and the details of designing a multi-color pixel. The measurements performed on the two-color pixel and the design for the four-color pixel, to be used in future generations of cameras are presented. Chapter 5 presents integration of the 16 two-color pixels on to a single chip and the detector design considerations. An overview of electronics and cryogenics which was used to show the camera its first light on CSO is presented and results from the CSO run showing maps of Jupiter and G34.3 are presented. The final chapter outlines some interesting future directions possible for the work that was done for this thesis.

CHAPTER II

PHYSICS OF SUPERCONDUCTING MICRORESONATORS

2.1 Introduction

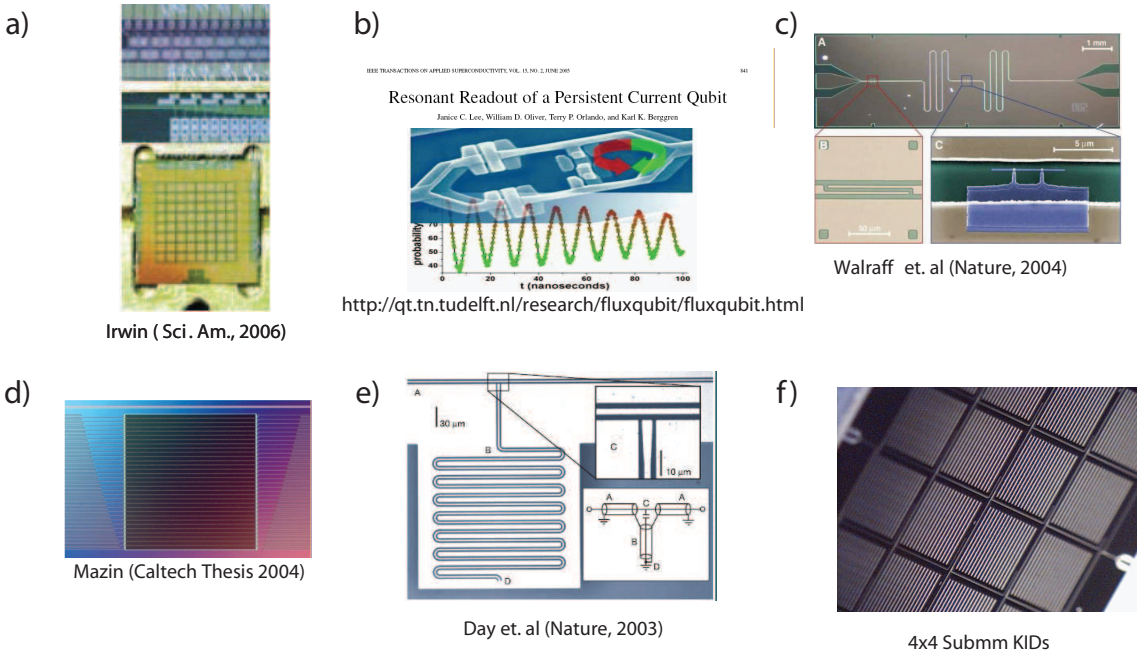

Figure 2.1: A variety of applications for superconducting microresonators are shown: a) Multiplexer for array of SQUIDs [24], b) Persistent current qubit using RF SQUIDs [25], c) Charge qubit coupled to superconducting microwave resonator [26], d) Kinetic Inductance Strip Detector [27], e) Quarter wave superconducting resonator coupled to a CPW feedline [28], f) 16-pixel submillimeter test chip made using Kinetic Inductance Detectors as a presursor to DemoCam

The submillimeter detectors described in this thesis use superconducting microresonators as the sensing element. However, the superconducting microresonators are versatile devices with diverse applications. They have been used for making SQUID multiplexers [24], qubits [26, 29], photon detection [28, 30, 31], and for studying basic

physics [32, 33, 34]. As SQUID multiplexers they find applications in making multiplexed readouts for large pixel count arrays of low-temperature detectors needed for novel particle and material physics, astronomy, and material science [24] (Figure 2.1a,b). In quantum computing superconducting microresonators have been used for reading out charge qubits [26], resolving the number states of microwave photons [35], stabilising flux qubits [36], and reading out RF qubits [29]. There are also proposals for making quantum memories [37] (Figure 2.1c) and coupling to polar molecules [38] using them, and they have also been used to investigate a variety of basic physics problems from non-linear oscillators [32] and their applications for making parametric amplifiers and squeezed states [33] to the physics of the Casimir effect [34].

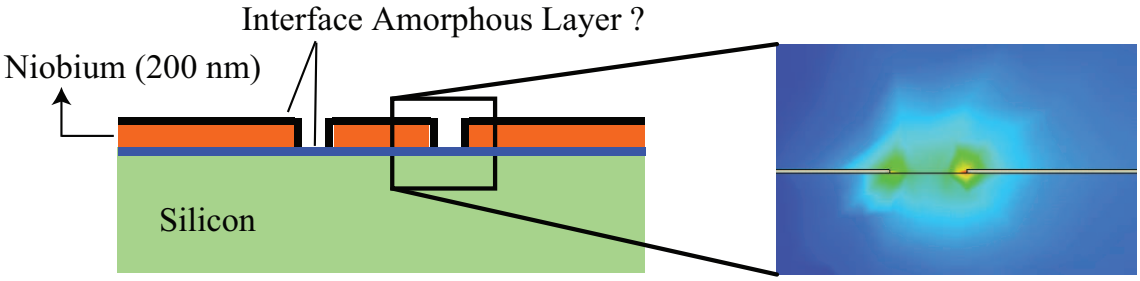

Figure 2.2: a) Cross section of the CPW geometry. The center conductor is made of superconducting metal (Nb) and is separated from the metallic ground plane through air slots deposited on a substrate – typically silicon or sapphire. b) HFSS simulation of the electromagnetic field of CPW line shown in cross section. High field regions are seen close to the metal edges – TLSs in these regions with dipole moment pointing in direction of the field and energy splitting resonant with the field will couple to it most strongly.

The early experiments in our group proceeded by noting that, instead of using superconductors close to their transition temperature as bolometric detectors [39], the kinetic inductance effect may be used to readout the change in the quasi-particle density of a superconducting film produced as a consequence of absorption of pair-breaking photons. This can be done by fabricating a thin film resonator using the superconductor and measuring the change in its resonant response to a microwave probe signal [40, 41, 42]. Indeed, the detector proof of principle was demonstrated

by energy-resolved detection of a 6 keV X-ray photon [28, 31, 43]. However, the experiments showed an unexplained excess noise which limited the performance of our detector [28, 27] and will in general limit the sensitivity of any experiment using the superconducting resonator as sensing or readout element. This noise has been measured and is seen to be primarily in the resonator frequency jitter or equivalently, the phase direction [44]. While the exact source of origin and the mechanism of noise generation is unknown, a likely possibility is that the noise is produced by two-level systems (TLS) in the amorphous native oxide layers on the metal films or susbstrate surfaces [45, 44] that couple to the electromagnetic field of the resonator through dipole coupling (Figure 2.2).

Indeed, TLS models provide a quantitative explanation for the unusual thermal, ultrasonic, and dielectric properties of amorphous materials at low-temperatures [46, 47, 48, 49], and recent qubit experiments [45] have focused attention on the important role of TLS in superconducting microcircuits. The TLS level populations and relaxation rates should vary strongly with the device temperature T, and the level populations of near-resonant TLS should saturate [44] for sufficiently strong resonator excitation power $P_{\mu w}$.

This chapter presents the measurements of the temperature and power dependence of the resonance frequency, quality factor, and frequency noise of superconducting niobium thin-film coplanar waveguide (CPW) resonators. In order to focus on the role of the dielectric materials, the measurements were carried out at temperatures well below the superconducting transition temperature ($T_c = 9.2$ K). We find that the frequency noise of the resonators is strongly temperature dependent, decreasing by nearly two orders of magnitude as the temperature is increased from 120 to 1200 mK, approximately described by a power law $T^{-1.76}$. We also find that the resonance frequency has a significant variation over this temperature range which agrees well with the standard two-level system (TLS) model for amorphous dielectrics. Hence,

measurements of the power and temperature variation of resonator frequency and noise, as presented in this chapter, provide an important test of the TLS hypothesis and do indeed suggest that the TLS are responsible for the noise in superconducting microresonators. These results have important implications for optimizing device design for use as qubits and photon detectors.

2.2 Experimental Introduction

We studied quarter-wavelength resonators made using coplanar waveguide (CPW) geometry [28, 44]. These have a center metal conductor separated from the ground plane by two air slots on either side, with most of the electromagnetic field residing in the slots (Figure 2.2).

Figure 2.3 shows the equivalent circuit and a photograph of an actual device very similar to the ones that were measured. The resonators are capacitively coupled to a CPW feedline and are measured using a standard IQ (In-phase and Quadrature-phase) homodyne mixing technique [28, 27] (Figure 2.4). With proper calibration, the complex output voltage of the IQ mixer, $Z = I + jQ$, is proportional to the forward scattering parameter S_{21}. For excitation frequencies far removed from the resonance frequency f_r, the microwave signal passes unimpeded through the feedline, but close to f_r the resonator loads the feedline resulting in a transmission null. Equivalently, in the complex plane when the microwave synthesizer's frequency f is swept through the resonance, $Z(f)$ follows a circular trajectory [44]. As explained in more detail below, the resonator's frequency f_r and quality factor Q_r may be extracted by fitting an analytical expression to the measured trajectory $Z(f)$. The combined noise of the resonator and readout electronics may be measured by setting the synthesizer frequency f to the resonance frequency f_r, then digitizing and analysing the fluctuations $\delta\xi(t) = [\delta I(t), \delta Q(t)]^T$[28, 27, 44]. The noise of the readout electronics may be measured separately by tuning the synthesizer frequency off resonance.

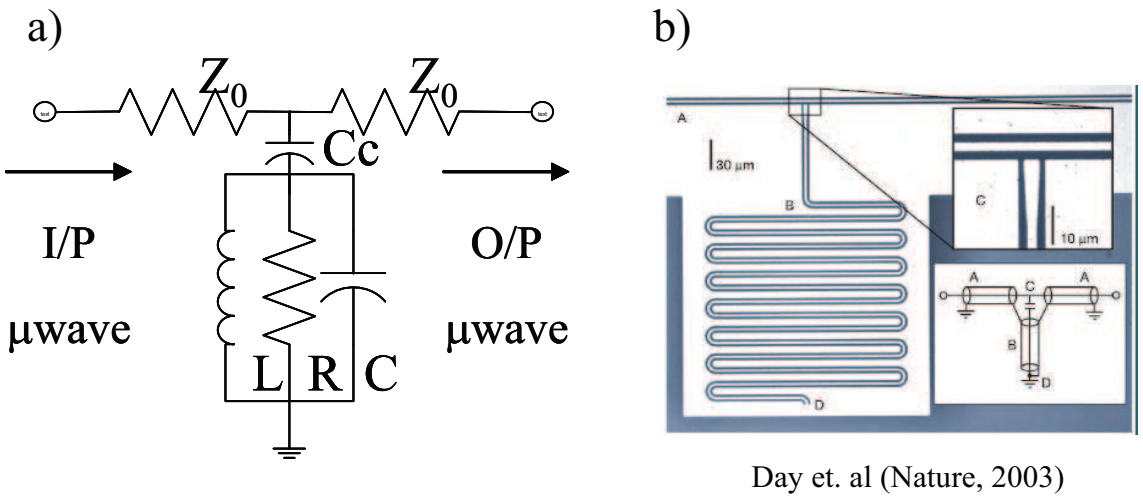

Day et. al (Nature, 2003)

Figure 2.3: a) Equivalent circuit for superconducting resonator device shown in b). Transmission line of imepdance Z_0 represents the feedline. Resonator is represented by parallel LCR circuit connected in shunt and capacitively coupled to the through line. b) Photograph of superconducting resonator [28]. Top view of the device is shown. White color is the thin film of superconducting metal, Aluminum. Blue is the substrate, Silicon. Meandered structure open circuited at the top and short circuited to the ground at the bottom is the quarter-wave transmission line resonator. Also shown on top is the CPW feedline.

2.3 Device Details

The device we studied was fabricated on a high-resistivity ($\rho \geq 10$ kΩ cm) silicon substrate by patterning a 200 nm thick niobium film using a photoresist mask and an SF_6 inductively-coupled plasma (ICP) etch. The CPW feedline has a 10 μm wide center strip and 6 μm gaps between center strip and the ground plane. For the resonator, these dimensions are 5 μm and 1 μm respectively. The resonator length is 5.8 mm which results in a resonance frequency of 4.35 GHz. The coupling strength between the resonator and feedline is set lithographically by the length of the coupling section, and is characterized by the quality factor Q_c that would be measured if no other losses were present. In general, a number of dissipation mechanisms contribute to the measured quality factor Q_r according to the familiar equation $Q_r^{-1} = Q_c^{-1} + Q_{sup}^{-1} + Q_{sub}^{-1} + Q_{rad}^{-1} + ...$, where Q_{sup} is contributed by superconductor loss, Q_{sub} is

from substrate loss, Q_{rad} describes radiation loss, etc. For the device studied here, our measurements indicate $Q_c = 5 \times 10^5$.

2.4 Experimental Setup

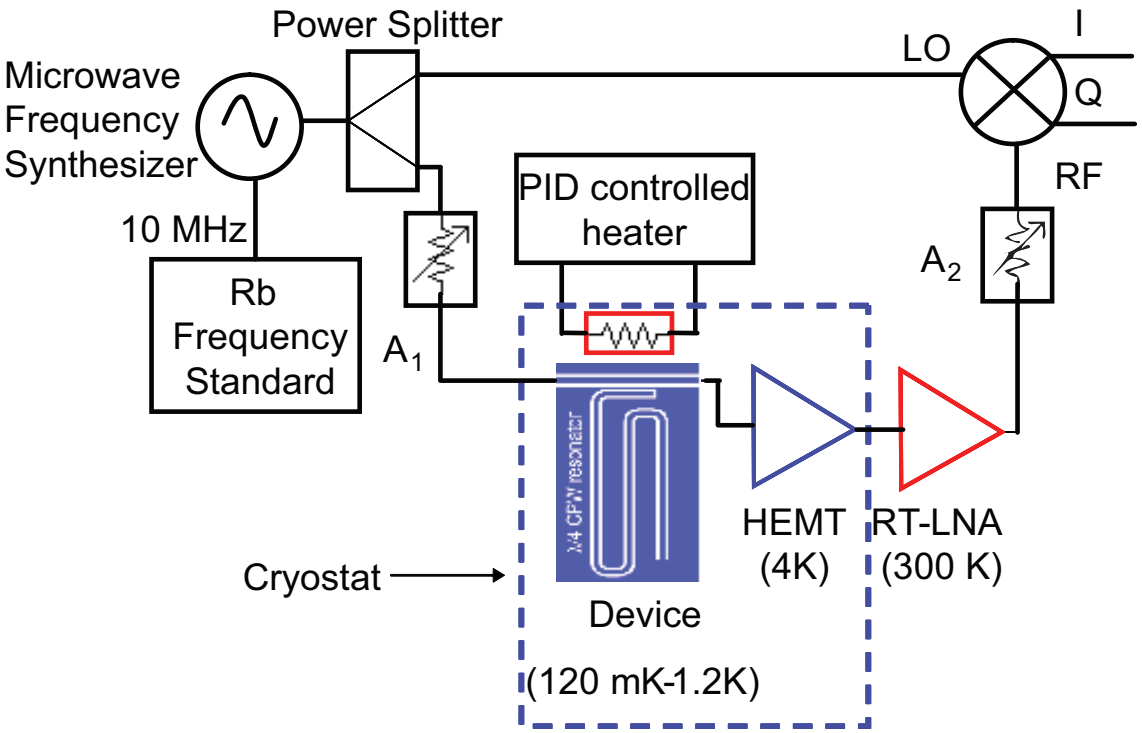

Figure 2.4: Block diagram for the experimental setup

The device was cooled to a base temperature of 120 mK using a dilution refrigerator [50]. A calibrated RuO_2 thermometer [51] was mounted on the copper sample enclosure and read out using an AC resistance bridge [52]. The temperature accuracy of this system is quoted to be $\pm$ 5 mK. The temperature was controlled using a heater attached to the mixing chamber of the dilution refrigerator and controlled using the PID feedback loop of AC resistance bridge[27]. To avoid frequency drifts, the microwave synthesizer [53] is stabilized using a rubidium standard [54]. The microwave power level $P_{\mu w}$ driving the resonator is adjustable over a wide range by using a programmable step attenuator A_1 before the signal enters the cryostat. After passing

through the device, the microwave output signal is amplified using a cryogenic HEMT amplifier which operates at 4 K and has a noise temperature $T_n \simeq 4K$, followed by another microwave amplifier at room temperature. The signal level is then adjusted by a second step attenuator A_2; by keeping the sum of the attenuations $A_1 + A_2$ constant (in dB), the signal entering the RF port of the IQ mixer is kept near the optimum level, avoiding both saturation and unnecessary noise. The output voltages of the IQ mixer are amplified, digitized with 16-bit resolution at a sampling rate of 250 kSa/s, and stored for further analysis.

2.5 Experiment

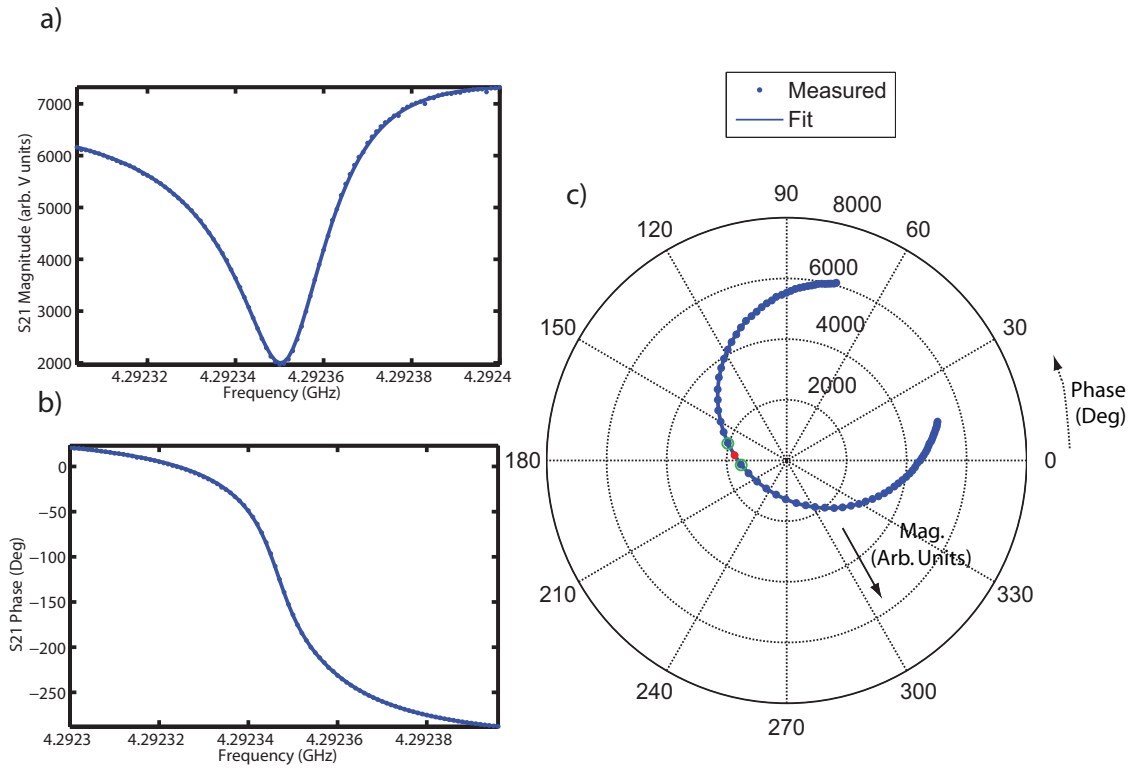

Figure 2.5: a) Amplitude vs frequency response of a quarter-wave resonator. b) Phase vs frequency response of a quarter-wave resonator. c) Response of the quarter-wave resonator plotted in the complex plane as frequency is swept through resonance. Red dot shows the on-resonance point. This resonator had a resonance frequency = 4.2924 GHz, Quality factor = 114,300.

The frequency sweep data $Z(f)$ and the time series (noise) data $\delta\xi(t)$ were recorded at device temperatures of 120 to 1200 mK in 40 mK steps, and power levels at the device of -108 to -72 dBm in 4 dB steps. For each combination of temperature and power, the freqency sweep data $Z(f)$ were used to determine the resonator frequency f_r and quality factor Q_r along with their uncertainties by complex least-squares fitting to the following nine-parameter model:

$$Z^{(model)}(f) = (A_0 + A_1\delta x)\ \exp[i(\phi_0+\phi_1\delta x)]\ \left[\frac{S_{21}^{(min)} + 2jQ_r\delta x}{1 + 2jQ_r\delta x}\right] + A_2\ \exp[i\phi_2]. \quad (2.1)$$

Here $\delta x = (f - f_r)/f_r$ is the fractional frequency offset, $A_0 + A_1\delta x$ allows for a linear system gain variation over the small frequency interval in the vicinity of the resonance, $\phi_0 + \phi_1\delta x$ represents a similar linear phase variation (mostly cable delay), and A_2 and ϕ_2 represent the output offset voltages of the IQ mixer in the absence of RF input. The resonator's physical response is given by the term in the large square brackets, which maps to a circle in the complex plane as the frequency offset δx is varied. This response is characterized by f_r and Q_r, and has an amplitude of nearly unity away from resonance but falls to the minimum amplitude $S_{21}^{(min)} = 1 - Q_r/Q_c$ at the center of the resonance.

The analysis of the time series noise data $\delta\xi(t)$ follows previous work [44] and proceeds by separating the data into time subintervals and calculating the Fourier transforms $\delta\xi(\nu)$ for each subinterval, followed by time (subinterval) averaging in order to obtain the frequency-domain noise covariance matrix $S(\nu)$, defined by $\left\langle \delta\xi(\nu)\delta\xi^{\dagger}(\nu')\right\rangle = S(\nu)\delta(\nu - \nu')$. The real part of this matrix is diagonalized at each frequency, which yields the noise spectra for amplitude (dissipation) and phase (frequency) fluctuations. In general, the amplitude noise is consistent with the noise floor of the electronics system as measured off resonance. Therefore, we subtract the amplitude noise spectrum from the phase noise spectrum in order to estimate the resonator's contribution to the measured phase noise. This subtraction is unimportant at low temperatures

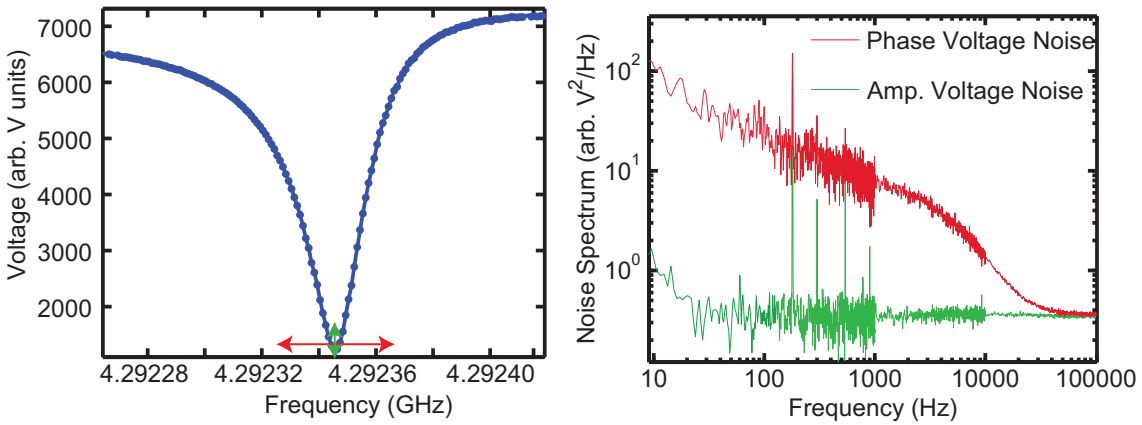

Figure 2.6: a) Resonator frequency response magnitude showing frequency (phase) and amplitude noise directions. b) Resonator amplitude and phase noise voltage spectrum

and high power levels, where the resonator's phase noise is dominant, but is helpful when fitting the temperature dependence of the noise in order to avoid introducing an extra fit parameter representing the level of the noise floor (See Figure 2.7).

2.6 Results

2.6.1 Frequency vs Temperature

The measured resonance frequency f_r is plotted as a function of temperature in Figure 2.8. Specifically, we plot the frequency shift $\delta f_r(T, P_{\mu w}) = f_r(T, P_{\mu w}) - f_r(120\text{ mK}, \text{-72 dBm})$, for two values of readout power $P_{\mu w}$, -72 dBm and -92 dBm. Note that the resonance frequency increases with temperature. In contrast, the variation of the superconductor's surface reactance with temperature as predicted by the Mattis-Bardeen theory [55] would cause a frequency shift (dashed curve in Figure 2.8a) that is several orders of magnitude smaller and opposite in sign. However, the data fits quite well to the functional form predicted by two-level system (TLS) theory [49]. Above 900 mK, this fit can be further improved by including the Mattis-Bardeen contribution according to the following model, since effects of superconductivity start

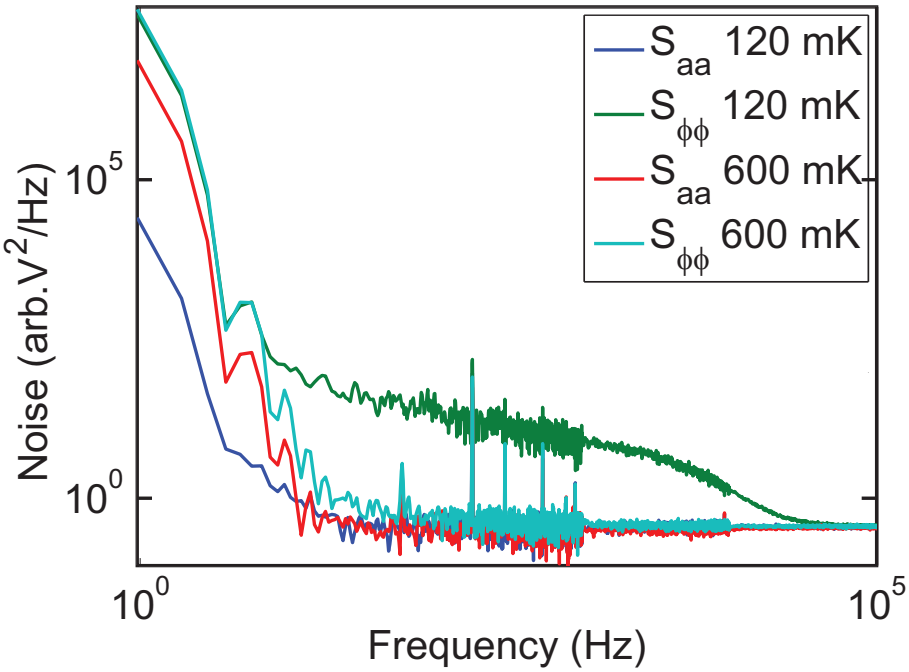

Figure 2.7: Resonator amplitude and phase noise spectrum at 120 mK and 600 mK. Amplitude voltage noise (S_{aa}) is consistent with noise floor of the readout. Phase voltage noise ($S_{\phi\phi}$) at 600 mK is seen to be lower than at 120 mK and closer to the noise floor.

becoming significant close to $T_c/10$:

$$\frac{\delta f_r^{(model)}(T, P_{\mu w})}{f_r} = C_1(P_{\mu w}) + C_2(P_{\mu w}) \left[\mathrm{Re}\, \psi \left(\frac{1}{2} + \frac{h f_r}{2\pi i k_b T} \right) - \log \left(\frac{h f_r}{k_b T} \right) \right] + \frac{C_3}{4} \left[\frac{\sigma_2(T) - \sigma_2(0)}{\sigma_2(0)} \right] . \quad (2.2)$$

This model is specified by three parameters at each power level. The first parameter $C_1(P_{\mu w})$ allows a small power-dependent shift of the resonance frequency f_r relative to f_r(120 mK, -72 dBm). The second parameter $C_2(P_{\mu w})$ is the coefficient for the term arising from linear TLS response theory [56] and is allowed to vary with power to account for possible saturation of TLS whose frequencies are close to the resonator frequency. The third parameter C_3 represents the kinetic inductance fraction of the CPW line [57] and should be independent of power. The difference plot between the overall fitted and measured data indicates that the fit matches the data to within the measurement accuracy of the system. This is set by our temperature readout.

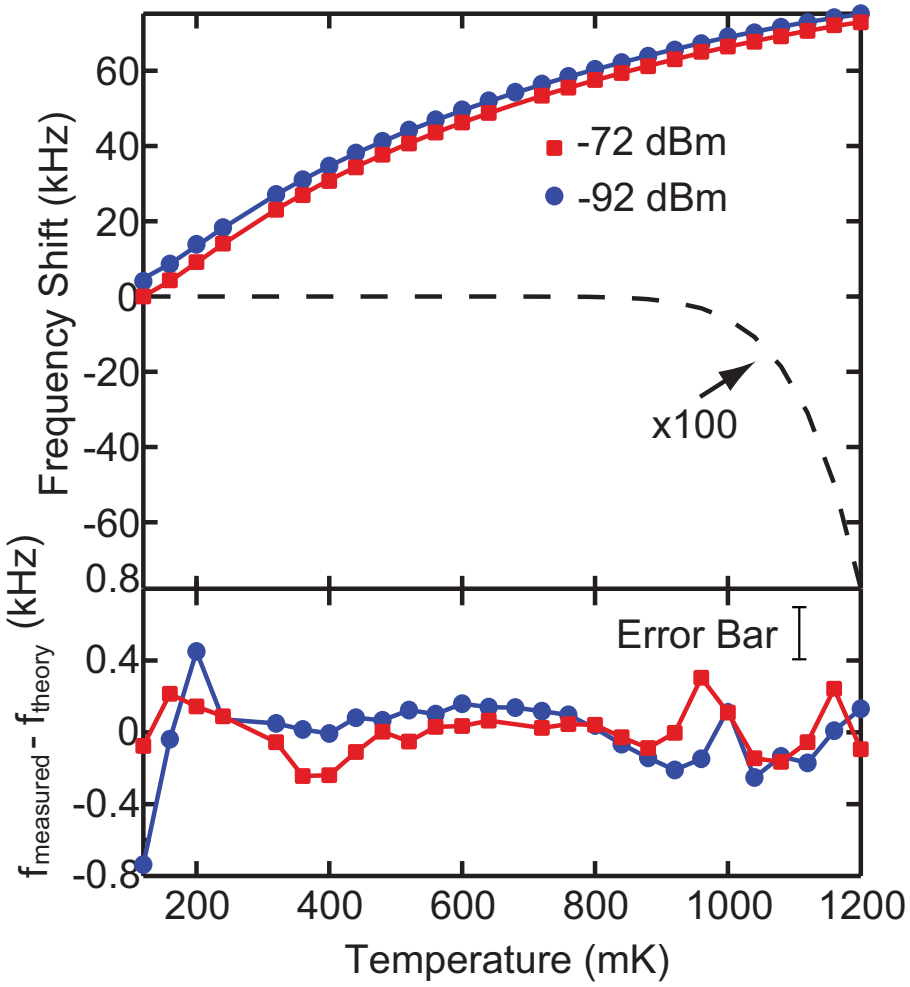

Figure 2.8: (a) Resonance frequency shift vs temperature for -72 dBm (Red) and -92 dBm (Blue) readout power. Dashed line shows the prediction of frequency shift using Mattis-Bardeen theory scaled up by a factor of 100. Solid lines represent fits to the data using TLS theory and Mattis Bardeen theory. (b) Difference plot between the data and the fits

The data was fitted for readout power values from -72 dBm to -92 dBm (steps of -4 dBm) to extract the coefficient values as a function of power. The value of kinetic inductance fraction was indeed found to be constant ($C_3 = 0.104 \pm 0.021$) as a function of power, in close agreement with the theoretical value [57] $C_3 = 0.125$. Meanwhile, $C_1 = 1.948 \pm 0.002 \times 10^{-5}$ at -72 dBm and $1.902 \pm 0.002 \times 10^{-5}$ at -92 dBm, while $C_2 = 9.09 \pm 0.02 \times 10^{-6}$ and $9.39 \pm 0.02 \times 10^{-6}$ for -72 and -92 dBm, respectively. The coefficient C_2 is a measure of the number of TLS that are coupled to the resonator.

This relationship may be quantified in terms of the microwave loss tangent δ of the amorphous TLS material and the $|\vec{E}|^2$-weighted volume filling fraction η (see eq. (2.3), (2.4)) of that material according to $C_2 = \eta\delta$. Typical amorphous materials have loss tangents of order $\delta \sim 10^{-3}$. Assuming a uniform distribution of TLS on the surface of the resonator, perhaps due to surface oxides, a reasonable oxide thickness of ~ 10 nm would be consistent with a filling factor of $\eta \sim 10^{-2}$ which we estimate.

2.6.2 Frequency vs Power

Figure 2.9 shows the power dependence of the resonance frequency shift in more detail. For a fixed temperature T, we find that the frequency shift δf_r scales with power approximately as $P_{\rm int}^{0.3}$, where $P_{\rm int} = 2Q_r^2 P_{\mu w}/(\pi Q_c)$ is the resonator's internal microwave power. TLS theory [58] predicts a $\sqrt{P_{\mu w}}$ dependence for the frequency shift. However, the resonators have a spatially dependent field which has not been included in the theory. For a fixed $P_{\mu w}$ the temperature dependence of the resonance frequency shows a peak at about 240 mK, in general agreement with the TLS theory [58].

2.6.3 Effects of TLS on Resonator Frequency and Quality Factor

Using basic electro-magnetic theory and considerations for energy stored and lost in the resonator in one cycle we have the expression for frequency shift and resonator quality factor as:

$$\frac{\delta f_r}{f_r} = \frac{2 f_r \varepsilon_0 Z_0 L}{V^2(0)} \int dx \int dy \left|\bar{E}(x,y)\right|^2 Re[\delta\varepsilon_d(x,y)] \tag{2.3}$$

$$\frac{1}{Q} = \frac{2 f_r \varepsilon_0 Z_0 L}{V^2(0)} \int dx \int dy \left|\bar{E}(x,y)\right|^2 Im[\delta\varepsilon_d(x,y)]. \tag{2.4}$$

Here f_r is the resonance frequency, ε_0 is the free space permittivity, Z_0 is the characteristic impedance, L is the resonator length, $V(0)$ is the voltage at open circuited end of CPW, $\bar{E}(x,y)$ is the electric field distribution in x-y plane - perpendicular to

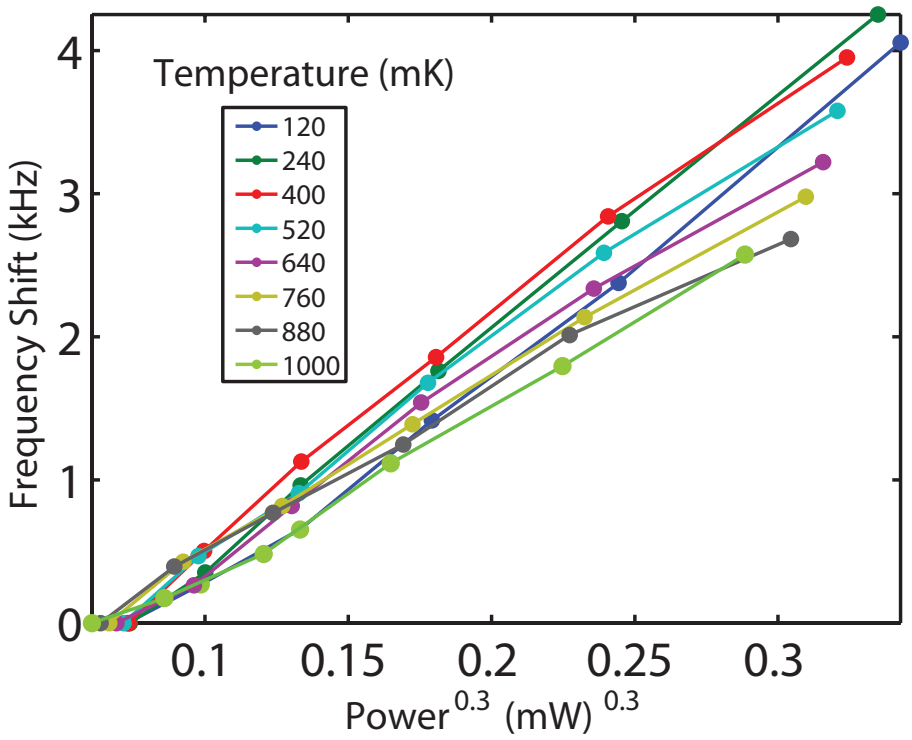

Figure 2.9: Resonance frequency shift ($\delta f_r(T, P_{int})$) vs resonator's internal microwave power (P_{int}) at constant temperature. The frequency shift ($f(T, P_{int}) - f(T, P_{int}^{min})$) is plotted on the y-axis where P_{int}^{min} is the minimum internal microwave power of the resonator.

direction of wave propagation in the resonator, and $\delta\varepsilon_d$ is the change in dielectric constant with temperature due to changes in TLS dynamics.

From the TLS theory we have [49]

$$\delta\varepsilon_d(x,y) = \frac{4\delta_l(x,y)\varepsilon_d}{\pi}\left[\psi\left(\frac{1}{2}+\frac{hf_r}{2\pi i k_b T}\right) - \ln\left(\frac{hf_r}{2\pi k_b T}\right)\right] \tag{2.5}$$

where ψ is the digamma function, δ_l is the material loss tangent purely dependent on material parameters as:

$$\delta_l(x,y) = \frac{d_0^2 \bar{P}(x,y) K_0 \pi}{2\varepsilon_0 \varepsilon_d} \tag{2.6}$$

where d_0 is the dipole moment of the TLS, $P(x,y)$ is the position dependent density of states, and K_0 is a material dependent parameter.

Using the expressions $Z_0 = \sqrt{\frac{\mathcal{L}}{\mathcal{C}}}$ and $f_r = \frac{v_p}{4L} = \frac{1}{4L\sqrt{\mathcal{L}\mathcal{C}}}$, where $\mathcal{L}$ and $\mathcal{C}$ are

inductance and capacitance per unit length, v_p phase velocity, and defining normalised electric field $\bar{E}_n(x,y) = \bar{E}(x,y)/V(0)$

$$\frac{1}{Q} = \frac{\varepsilon_0}{\mathcal{C}} \int dx \int dy \varepsilon_d(x,y) \bar{E}_n^2(x,y) \delta_l(x,y) \tanh\left(\frac{hf_r}{2k_bT}\right). \tag{2.7}$$

Similarly the TLS contribution to the frequency shift can be written as:

$$\frac{\delta f_r}{f_r} = \frac{2\varepsilon_0}{\pi\mathcal{C}} \int dx \int dy \varepsilon_d(x,y) \bar{E}_n^2(x,y) \delta_l(x,y) \left[\psi\left(\frac{1}{2} + \frac{hf_r}{2\pi i k_bT}\right) - \ln\left(\frac{hf_r}{2k_bT}\right)\right]. \tag{2.8}$$

By comparing the second term in expression equation (2.2), (2.7), and (2.8), and accounting for saturation of the TLSs due to microwave power [56] we can write the relation between frequency shift coefficient C_2 and Q_{TLS} as:

$$Q_{TLS} = Q_0 \coth\left(\frac{hf_r}{2k_bT}\right) \sqrt{1 + \frac{P_{\mu w}}{P_{critical}(T)}} \tag{2.9}$$

where $Q_0 = 2f_r/\pi C_2$ and $P_{critical} \sim \coth\left(\frac{hf_r}{2k_bT}\right) T^\beta$. Figure 2.10 indicates that this formula does not describe the data well; it does however, capture the decrease in Q_r as the temperature is increased, especially at low temperatures.

The interpretation of this data in the context of a TLS model is made difficult by the fact that the microwave readout power levels used in our experiment are sufficiently high to saturate the dissipation [44, 45, 58]. In contrast, the resonance frequency is much less susceptible to TLS saturation [58] and can still provide a robust technique for probing TLS effects. Although microwave power could have been reduced to avoid TLS saturation, at these low powers the resonator noise drops below the HEMT amplifier noise floor. Measuring the temperature dependence of frequency noise is a key result of this chapter.

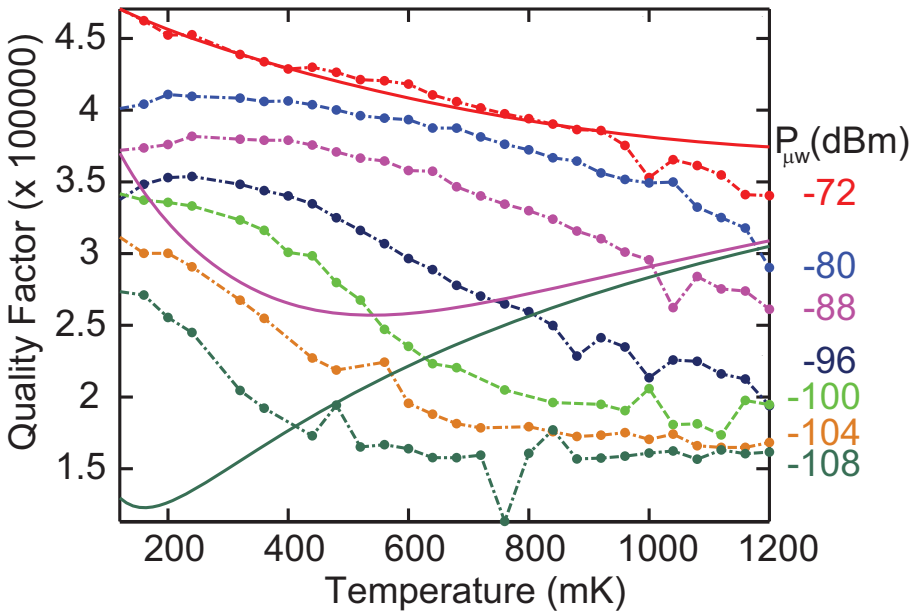

Figure 2.10: Resonator quality factor (Q) vs temperature (T) for different microwave readout powers in dBm ($P_{\mu w}$). The dotted lines show the measured value of the quality factor while the solid lines show the values calculated using the TLS theory, while accounting for the temperature dependence of critical readout power as shown in equation 2.9.

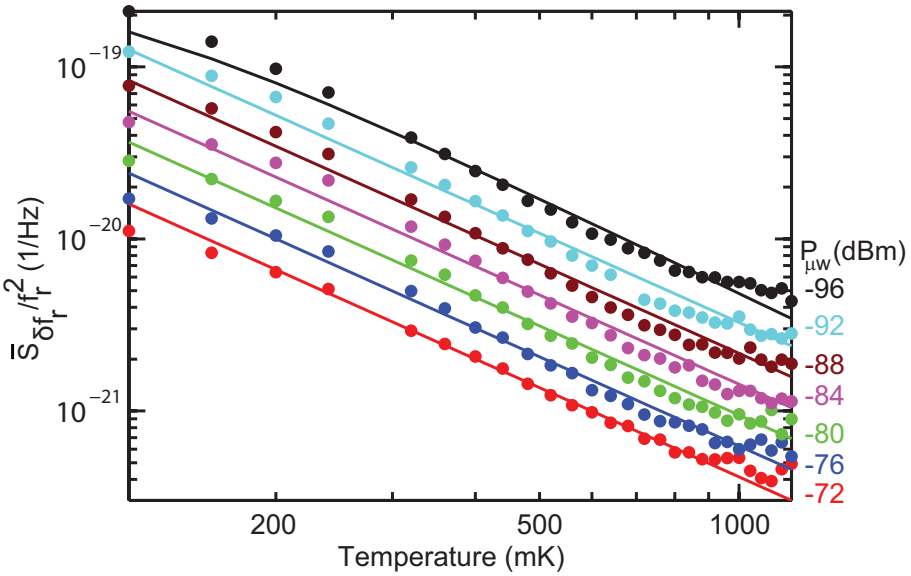

Figure 2.11: Average fractional frequency noise ($\bar{S}_{\delta f_r}(\nu)/f_r^2$) vs temperature ($T$) for different microwave readout powers ($P_{\mu w}$) (in dBm)

2.6.4 Frequency Noise vs Temperature

The temperature and power dependence of the resonator was quantified by first calculating the fractional frequency noise spectrum [44], $S_{\delta f_r}(\nu)/f_r^2$, which was then averaged over the range 200–300 Hz, a clean portion of the spectrum well above the HEMT noise floor at low temperatures. The resulting values are plotted in Figure 2.11. This demonstrates the very strong temperature dependence of the noise; as the temperature is increased from 120 mK to 1200 mK the noise decreases by almost two orders of magnitude. The overall trend is reasonably well described by the following power law form:

$$\frac{\bar{S}_{\delta f_r}(\nu)}{f_r^2} = AT^{\alpha}P_{\mu w}^{\beta} \tag{2.10}$$

with the indices $\alpha = -1.73 \pm 0.02$, $\beta = -0.46 \pm 0.005$ consistent with previous work [44]. An equivalently good fit is obtained by using a functional form motivated by using the TLS theory [58]:

$$\frac{\bar{S}_{\delta f_r}(\nu)}{f_r^2} = AT^{\alpha}P_{\mu w}^{\beta}\tanh^2\left(\frac{\hbar\omega}{2k_bT}\right) \tag{2.11}$$

with $\alpha = 0.14 \pm 0.02$ and $\beta = -0.46 \pm 0.005$. The values for these coefficients are consistent with the values obtained for power law coefficients, since at high temperatures $\tanh^2\left(\frac{hf_r}{2k_bT}\right)$ scales as $1/T^2$.

2.7 Conclusion

In conclusion, both the resonance frequency and resonator noise show substantial variation at temperatures far below the superconducting critical temperature. Furthermore, the variation of the resonance frequency is well described by TLS theory with plausible values for loss tangent and filling factor. Combined together, these results strongly suggest that the resonator noise is also due to TLS and not related to

the superconductor. The temperature dependence of this noise has important practical implications. For instance, if the TLS origin of the noise is correct, designing resonators to operate in the regime $f_r << 2kT/h$ could result in lower noise and improved performance.

CHAPTER III

PIXEL DESIGN

3.1 Introduction

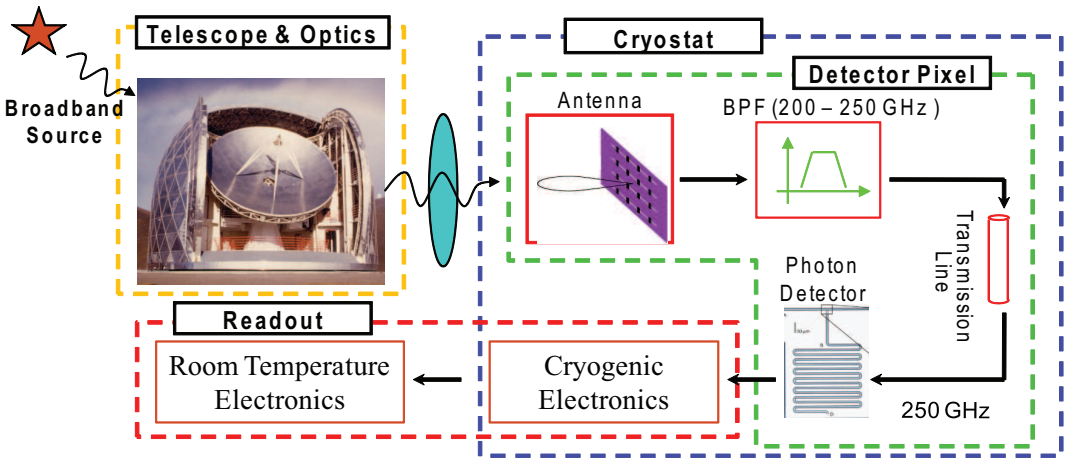

Figure 3.1: Schematic of a submillimeter detector system showing its constituent components

Figure 3.1 shows the schematic for a system used for submillimeter astronomy. The telescope collects the radiation from a distant source and illuminates the detector array which is readout by electronics that together with the array forms the camera. The photon detectors and a part of their readout circuitry typically work at cryogenic temperatures due to the stringent performance requirements. For our devices the operating temperature is close to 220 mK and the camera, along with a part of the readout circuitry, is housed inside a cryostat. This chapter concentrates on the design of a submillimeter camera pixel with the aim of finally designing the 16-pixel, two-color camera discussed in Chapter 5.

A submillimeter pixel is comprised of 4 sub-components:

1. Antenna – To efficiently couple the broadband submillimeter radiation coming from the telescope to the detector,

2. Bandpass filters (BPF) – To reduce the bandwidth of light to frequencies of interest before transmitting it to the detector. Its primary purpose is to remove the frequencies at which the atmosphere is opaque (see Chapter 4) so that they do not load the detector and degrade its performance,

3. Submillimeter transmission line – To transmit the filtered radiation from the bandpass filters to the photon detector,

4. Photon detector – To act as a sensor for submillimeter radiation.

Each of the above components can be designed using different technologies. Figure 3.2 compares two different implementations of a 16-pixel camera. The top image shows Arcminute Cosmology Bolometer Array Receiver (ACBAR) [59] which is an extremely sensitive multifrequency, millimeter-wave receiver that has been used for measurements of the temperature anisotropies of the CMB and SZE in galaxy clusters. This instrument has been extremely successful in generating a wealth of data which has been used to investigate the cosmological parameters by measuring both, the primary anisotropies from the big bang and secondary anisotropies generated by the SZE [60, 61]. The bottom image shows a demonstration camera (DemoCam) whose future generations will be used for observing submillimeter galaxies, undertaking galactic plane surveys and measuring SZE.

The remainder of this section discusses the possible alternate designs for the submillimeter pixel components that are typically used in current instruments and inspite of excellent performance prevent a scalable architecture which is required for future cameras.

Figure 3.2 shows that one of the designs that can be used for implementing an antenna is by using metal feedhorns. While these have excellent performance, they

are massive, large, and add to the thermal mass of the focal plane. Further, they directly focus the submillimeter light on to the detector, which limits the absorption area of the detector to λ^2 due to diffraction limits. DemoCam implements antenna on chip using multi-slot, planar geometry [62]. This results in a small thermal mass. Further, it has a narrow beam since it combines light from multiple slots, resulting in a large effective area (A_{eff}) for the antenna, as explained in Section 3.2. This allows us to couple the light from the telescope directly to the device without any interceding on-chip optics (e.g. fly's-eye lenses [63]) and greatly enhances scalability. Another major advantage of the antenna design is its multi-octave bandwidth.

The band pass filters can be implemented using metal-mesh filters in conjunction with IR blocking materials such as flurogold and teflon [64]. We have implemented on-chip, lumped-element, superconducting band-pass filters for the DemoCam. The advantages and disadvantages of the two approaches are discussed in Chapter 4.

ACBAR uses hollow metal waveguides as submillimeter transmission lines, which may be replaced by low-loss, superconducting microstrips [65] implemented on the same substrate as the rest of the pixel. These microstrips pass submillimeter signal below 700 GHz with high efficiency, but are lossy for higher frequencies and can be used for filtering out infrared (IR) wavelengths.

The photon detectors used in ACBAR are bolometers made from gold-plated silicon nitride micro-mesh absorbers with neutron transmutation doped (NTD) germanium thermistors [66]. These are very sensitive but require separate JFET preamps and readout wiring for each detector, which rapidly becomes impractical for large arrays. It is possible to make multiplexed readouts for bolometers that use superconducting Transition Edge Sensor (TES) thermistors [39], but the multiplexing chips are fabricated separately and then bump bonded to the camera chip making it expensive, complicated, and lowering the yield [24]. We use a novel superconducting photon detector technology - Microwave Kinetic Inductance Detectors (MKIDs) [27]

which is a powerful new approach to making large arrays. These arrays can be easily read out using just two microwave coax cables by frequency division multiplexing. The fabrication process for our devices is relatively simple compared to bolometers both in terms of being monolithic and requiring fewer mask layers allowing for higher yields, lower costs and greater scalability.

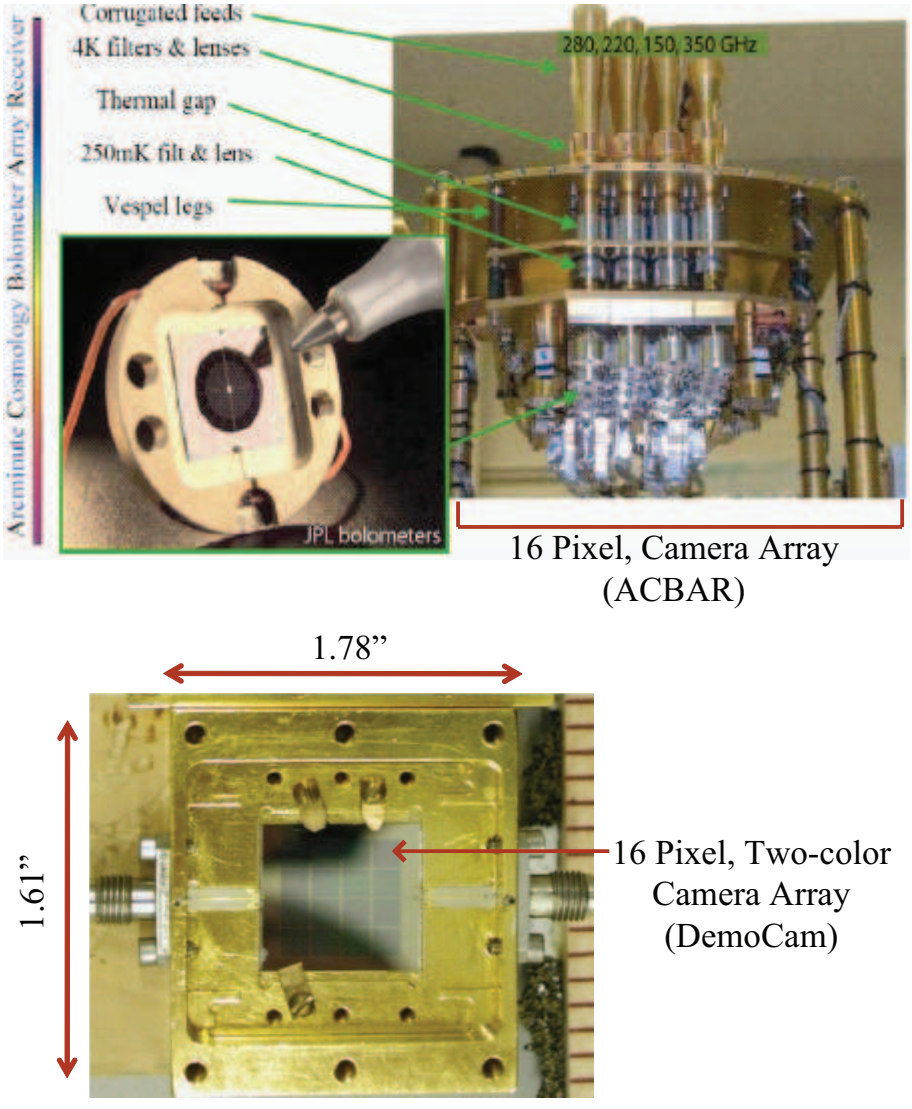

Figure 3.2: Comparing 16-pixel cameras made using two different technologies for constituent elements

The next few sections discuss the designs of each of these components.

3.2 Multi-slot Antenna

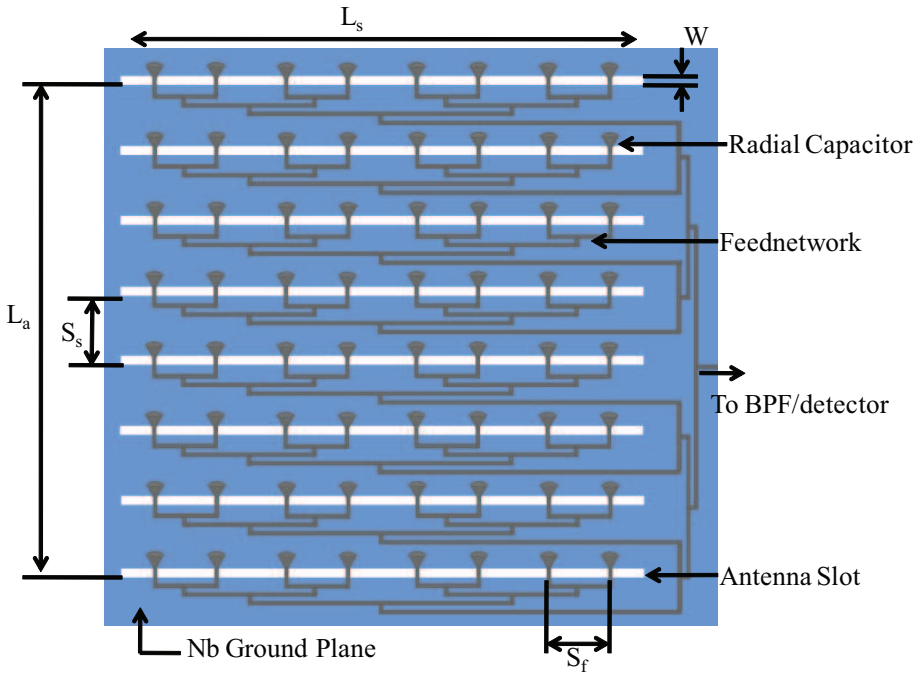

Figure 3.3: Schematic of multi-slot antenna. Blue regions are where the niobium metal is deposited. White regions are where a slot has been etched into the niobium and the substrate can be seen. Grey color shows the wiring (top) layer of the microstrip structure, also made out of niobium. The drawing shows 8 slots and 8 taps on each slot for clarity, the actual antenna has 16 slots and 16 taps on each slot. The parameters defining the antenna geometry are slot length L_s, array length L_a, number of slots N, and number of taps on each slot M. These are related to distance between slots S_s and distance between taps S_f as $S_s = L_a/(N-1)$ and $S_f = L_s/M$, respectively. t is the slot width. The values of these parameters for our antenna design are tabulated in Table 3.1

This section briefly presents the antenna design which is detailed in [62]. The antenna has a design beam width of 19° full width half maximum (FWHM) at 250 GHz. Frequencies in the range 200 - 400 GHz are of interest since they coincide with one of the atmospheric passbands (Chapter 4).

The antenna is implemented by etching 16 slots in a 2000 A thick niobium film deposited on a high-dielectric-constant substrate, e.g., Si ($\varepsilon_d = 11.9$). Each of the slots is bridged by 16 microstrip taps (Figures 3.3, 3.4). The microstrip design is presented

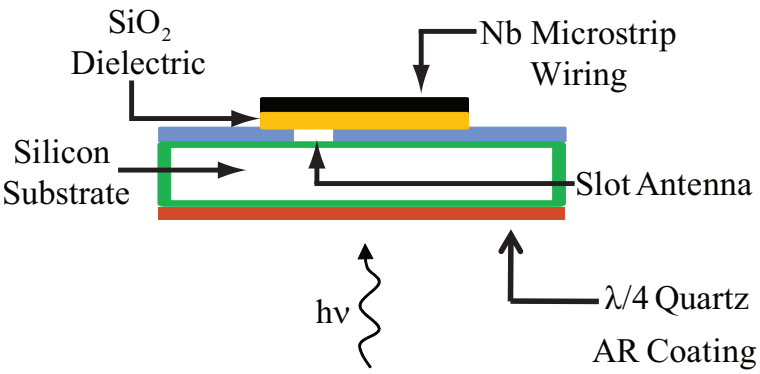

Figure 3.4: Side view of the antenna

in the next section. When electromagnetic radiation impinges on this structure it excites currents in the ground plane and electric fields in each of the slots. The submillimeter power from the slots is collected by the microstrip taps bridging them. The broadband short (shown as the radial capacitor on top of the taps in Figure 3.3) forces the power to flow in the direction of binary tree power combining network.

Figure 3.4 shows the sideview of the antenna. It shows that the antenna is illuminated from the substrate side. This results in a higher coupling efficiency since most of the the antenna beam resides in the substrate since it has a higher dielectric constant than vacuum. The front-to-back ratio, the ratio of the integrated beam power on the substrate side to the vacuum side, is given by $\sqrt{\varepsilon_d}$, for a narrow beam antenna [62]. The antenna efficiency for a silicon substrate, assuming a perfect anti-reflection (AR) coating is:

$$\eta_f = \frac{\sqrt{\varepsilon_d}}{1+\sqrt{\varepsilon_d}} = 78\% \tag{3.1}$$

The material used for the antireflection coating between vacuum and substrate to increase the antenna efficiency should ideally have a dielectric constant $\varepsilon_{AR} = \sqrt{\varepsilon_d} = 3.4$. A convenient choice of material for this purpose is quartz, with $\varepsilon_{AR} = 3.8$. The ideal thickness for the AR coating can be calculated using the quarter-wave resonance

condition $t_a = \dfrac{\lambda_0}{4\sqrt{\varepsilon_{AR}}} = 154\ \mu$m, where λ_0 is the wavelength of interest in free space (1200 μm at 250 GHz).

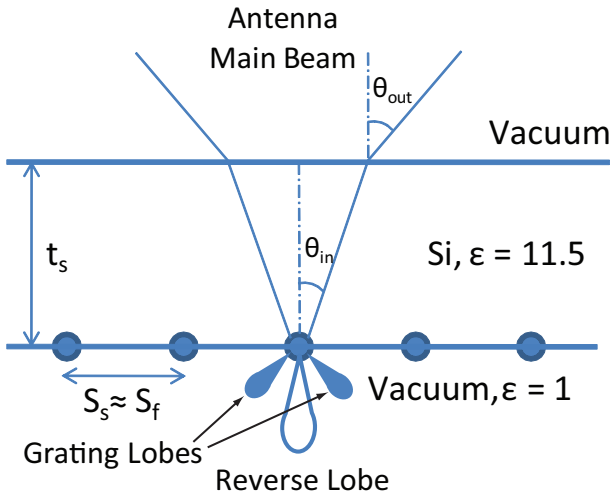

Figure 3.5: Antenna beam pattern using a diffraction grating model

The antenna was designed to couple efficiently to the telescope optics. This is done by ensuring that the beam from the telescope optics matches the antenna beam pattern well. A convenient way to characterize the beam angle is the F-number, defined as $F = 1/2 \tan\theta_{out}$ where θ_{out} is FWHM beam angle outside the substrate (Figure 3.5). For the first on-telescope demonstration of our camera the coupling optics from the Bolocam instrument [15] were used and the antenna was designed for an $F = 3$ beam at 250 GHz.

The beam width is determined by the overall size of the antenna, and the beam matching condition translates to antenna size $L_{s,a} \sim F\lambda_{optics}$. More precisely, note that if the array of slots and taps is dense compared to wavelength of interest, for uniform slot excitation the far-field beam pattern of the slot array is expected to be same as the far field diffraction pattern of a uniformly lit aperture given by [62]:

$$\frac{dP}{d\Omega} \propto \mathrm{sinc}^2\left(\frac{\pi L_s}{\lambda_0}\sin\theta\cos\phi\right)\mathrm{sinc}^2\left(\frac{\pi L_a}{\lambda_0}\sin\theta\sin\phi\right) \tag{3.2}$$

Antenna Parameters	
Slot length (L_s)	3.2 mm
Array Length (L_a)	3.2 mm
Number of slots (N)	16
Number of feeds (M)	16
Slot Width (W)	20 µm
Slot Spacing (S_s)	200 µm
Feed Spacing (S_f)	187.5 µm
Substrate Si, Dielectric Constant (ε_d)	11.5
Substrate thickness (t_s)	500 µm
AR coating, Dielectric Constant (ε_{AR})	3.8
Quartz thickness (t_a)	154
Frequency range	100 – 416 GHz
Beam angle ($2\theta_{out}$) @ 300 GHz, FWHM	16.8°

Table 3.1: Dimensions for the antenna layout

where $\Omega = (\theta, \phi)$ are the usual polar co-ordinates, and λ_0 is the free space wavelength. Combining this expression with definition for the F-number the antenna length is given by [62]:

$$L_{s,a} = 0.886 F_{-3dB} \lambda_0 \tag{3.3}$$

where $F_{-3dB} = 3$ defines the FWHM beam size. We get a slot and array length of 3.2 mm. The final value used for slot length was 3 mm due to layout considerations. The array slot and tap spacing is determined using high-frequency response of the antenna. At high frequencies the discreteness of elements constituting the antenna leads to a diffraction grating-like behavior (Figure 3.5). This results in the formation of grating sidelobes, which cause power to be lost into the substrate modes, reducing

the antenna efficiency. The antenna beam pattern in the plane perpendicular to the slots depends on the array factor given by [62]:

$$A(\Omega) = \frac{\sin(Nt/2)}{\sin(t/2)} \tag{3.4}$$

where

$$t = 2\pi\sqrt{\varepsilon_d} S_s \sin\theta_{out}/\lambda_0 \tag{3.5}$$

and S_s is the slot spacing. The array factor has a strong peak as $\theta_{out} \to 0$, $A(\Omega) \to N$. It also has peaks at $t = \pm 2n\pi$ where n is a positive integer. These are the grating sidelobes and to prevent their formation, accounting for the finite beam width, the required condition is given by [62]:

$$S_s \leq \frac{\lambda_0}{\sqrt{\varepsilon_d}} \left(1 - \frac{1}{N}\right) \tag{3.6}$$

which gives the expression for minimum number of slots to prevent appearance of sidelobes as [62]:

$$N \simeq \frac{L_{s,a}\sqrt{\varepsilon_d}}{\lambda_{0,min}} + 2. \tag{3.7}$$

A similar expression can be obtained for the minimum number of taps required [62]. To satisfy these conditions using a binary tree feed network we need 16 slots and 16 taps on each slot for our antenna design for $\lambda_{0,min} = 721\ \mu m$ ($f_{max} \sim 416$ GHz). Equation (3.5) can be used to calculate the upper cutoff frequency of the antenna based on its beam pattern. The lower cutoff frequency for the antenna can be calculated by using the fact that at long wavelengths the beam becomes broader until finally it violates the condition for total internal reflection. The main beam does not reach its null before critical angle for $\lambda_{max} = L_{s,a}$, as may be checked by substituting $\sin\theta = 1/\sqrt{\varepsilon_d}$ in expression for t. This gives us 100 GHz as the antenna lower cutoff

frequency. Finally, the approximate width for each of the slots was determined using a method of moments calculation. The antenna has an impedance of $\simeq 20\ \Omega$ for a slot width of 20 μm at 250 GHz [62]. These numbers, along with other dimensions for our antenna design, are tabulated in Table 3.1.

3.3 Microstrip and feed network Design

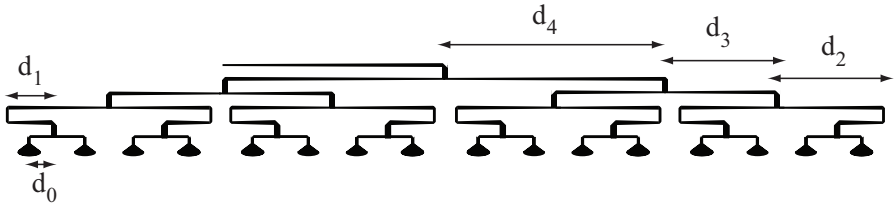

Figure 3.6: Feed network schematic with 16 taps

This section explains the design of binary tree feednetwork which combines the submillimeter power from each of the taps and the slots of the antenna and brings it out into a single output microstrip.

Figures 3.6 and 3.7 show schematics of the layout for the microstrips used to implement the feednetwork. The power from the 16 taps on a single slot are combined in a 4-level binary tree. To ensure in-phase power combination, the network is designed so that the distance from output microstrip to each of the taps on any slot is equal. The microstrips are implemented using a 4000 A thick SiO_2 dielectric and a 2000 A thick niobium wiring layer. The antenna taps were simulated using SUPERMIX [67], a software that simulates superconducting circuit elements and a width of 2.5 μm was chosen to obtain an impedance of 20 Ω at 250 GHz. This value is close to the antenna impedance as is needed to optimise the coupling of the millimeter signal. The SiO_2 dielectric constant value for the SUPERMIX simulations was assumed to be $\varepsilon_d = 4$. This value is close to the bulk value and is well corroborated by the bandpass filter measurements (Chapter 4). The niobium bandgap is 700 GHz which allows us

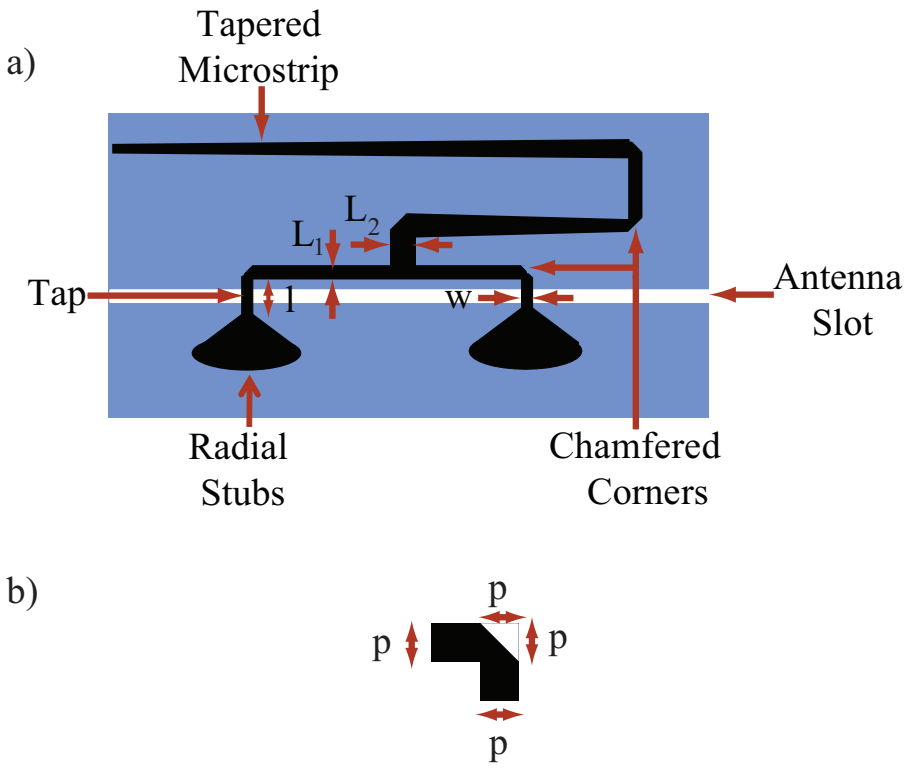

Figure 3.7: a) Feed network schematic. Blue shows the niobium deposited on the silicon substrate which is seen in white in the antenna slot. Black shows the niobium wiring layer and the geometry of the feednetwork. b) Schematic of chamfered corner of the microstrip

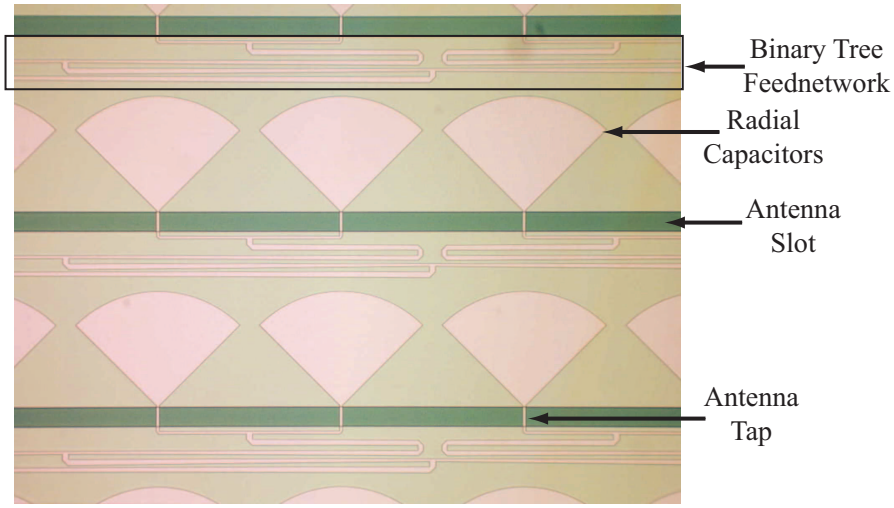

Figure 3.8: Optical image of the antenna slot and the feednetwork taken under the microscope

Tap Power Combining Network			
t	26.5		
w	2.5		
	Length	Start Width	Stop Width
d_0	95	2.5	2.5
d_1	170	5.8	4.8
d_2	360	4.8	2.5
d_3	372	5.8	2.5
d_4	744	5.8	2.5
d_5	1632	5.8	2.5
Slot Power Combining Network			
t	20		
w	2.5		
	Length	Start Width	Stop Width
d_0	101.5	2.5	2.5
d_1	170	5.8	4.8
d_2	377	4.8	2.5
d_3	397	5.8	2.5
d_4	797	5.8	2.5

Table 3.2: Table with dimensions for the feednetwork corresponding to Figures 3.6 and 3.7

to transmit signals up to 700 GHz with low loss. However, higher-frequency signals would make niobium lossy and degrade the antenna efficiency.

At each level of the binary tree, two microstrips merge to form a single microstrip and summing the submillimeter power carried by them in the procees. The width of the resultant microstrip is increased from original value of L_1 (= 2.5 μm) to a new value L_2 (= 5.8 μm) (see Figure 3.7) so that the admittance of the combined microstrip section is equal to the sum of the admittance of individual sections. The width of the new microstrip is then adiabatically linearly reduced to the original value of L_1 to ensure that the final microstrip width at the taps remains within the

lithographic limits and to keep the impedance of the output microstrip the same as the impedance of the antenna taps.

All microstrip corners are chamfered to reduce added reflections due to the extra corner capacitance [68]. The chamfer is a made at 45° and the geometry is shown in Figure 3.7b. Also, visible in Figures 3.6 and 3.7 the first binary tree level is made with an added microstrip section instead of directly combining the two microstrips as is done at higher levels. This is seen as an extra, u-shaped microstrip section that allows us to taper down the microstrip over 530 μm. If the microstrips were directly joined as in the remaining sections, this distance would be reduced to $\sim$ 180 μm resulting in added reflections and poor coupling of the submillimeter signal [69].

The microstrip loss is dominated by the dielectric loss tangent which, for SiO dielectric mictrostrip feednetwork, has been measured to be around 10^{-3} [65]. The loss was found to be almost constant $\sim$ 0.5% per guide wavelength (λ_g) at 1.5 K [65]. We expect similar loss tangents for for the SiO_2 dielectric films used in our feednetwork. The total length of the feednetwork and output microstrip is $\sim 18\lambda_g$ which should result in loss of around 10% from the feednetwork.

Figure 3.8 shows an image of the feednetwork implemented on the camera pixel. Table 3.2 gives the actual dimensions of the feednetwork that was finally used.

3.4 Beam Map Measurement

The antenna and the feednetwork were characterised by measuring the antenna beam pattern. This was done using the optical setup whose schematic is shown in Figure 3.9. The pixels were illuminated using a 400 C blackbody source mounted on an x-y stage. The blackbody source was raster scanned in front of the dewar windows and the detector response was readout for the measurement. A combination of polytetrafluoroethylene (PTFE) and fluorogold windows was used in the optical chain for blocking the out-of-band infrared radiation.

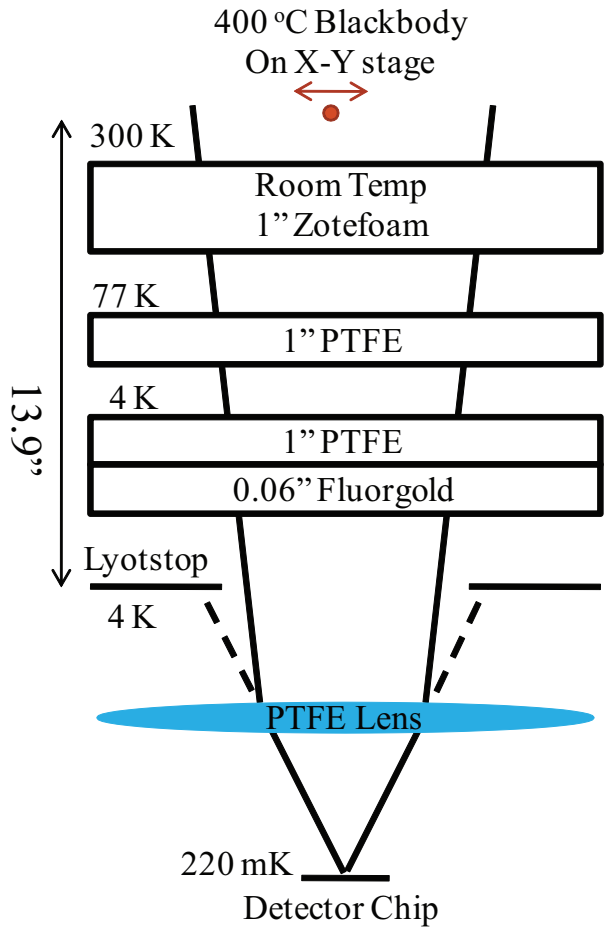

Figure 3.9: Optical chain used to measure the beam maps

The figure also shows a lens was used in the optical chain. The cryostat used to measure the beam maps was adapted from an existing setup and had windows smaller than the beam size. The lens was needed to ensure that the main beam was not blocked by the dewar winows. This arrangement will reduce the efficiency of coupling to the telescope optics due to beam mismatch and will be rectified for future cryostat designs. The lens has a diameter 3.67" and a radius of curvature of 75 mm for the parabola on both sides. The maximum thickness was 32.45 mm. PTFE has a refractive index of 1.44. The distance between Lyot stop and the pixel was twice the lens focal length, such that the location of the antenna beam waist is at the same location as the Lyot stop. The Lyot stop is a cold surface (4 K) with an aperture in

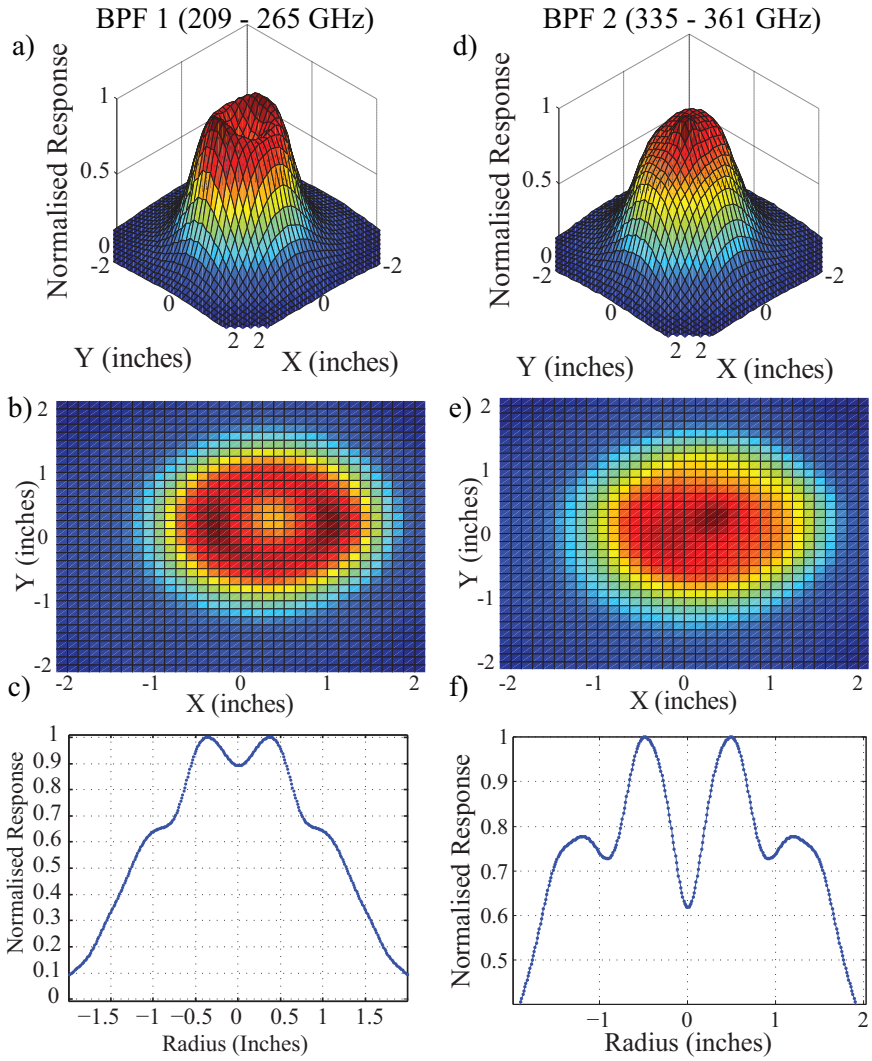

Figure 3.10: a), b), d), e) show 3D (top) and 2D (bottom) contour maps for the antenna beams. x and y axes show the location on the antenna beam and z axis (color in the 2D map) shows the normalised antenna response at the location. c), f) show ZEMAX simulations for the same. All the plots are at a distance of 13.9" from the Lyot stop. The plots in the left column are for the 209-265 GHz band and in the right column are for 335-361 GHz band.

the center, which terminates the antenna diffraction sidelobes but lets the antenna main beam pass through the aperture.

Figure 3.10 shows the beam maps for the antenna in the two frequency bands (209-265 GHz, 335-361 GHz). The contour plots are the actual data with the blackbody source 13.9" away from the Lyot stop. The bottom two plots are the simulations for

the same optical configuration as used to take the beam maps using ZEMAX [70]. The near-field simulations done using ZEMAX result in fringes in the calculated response which have been smoothed using a box car function. Residues of these smoothed out fringes are still visible as, for example, the dip at the center of the 335-361 GHz band (Figure 3.10 f)). However, the beams are seen to be well defined with sharp skirts. The measured FWHM value of the beam matches the ZEMAX simulations well, with a beam diameter of 2.45" ($2\theta_{out} = 10°$).

We notice a slight dip at the center of the beam for the first BPF band (209-265 GHz) and a small hump for the second BPF band (335-361 GHz) in the measured response. These features may be a result of making the beam map measurements in the near field. The far field is 40" away and at that distance a 400 C blackbody gives a poor signal-to-noise ratio, which results in poor quality beam maps. A stronger source (1000 C) will be used in the far field for further studies. But the results for simulations and measured beam maps are seen to be in good agreement, and the quality of beam maps was good enough to use the pixel for first demonstration of the camera on the sky (Chapter 5).

3.5 Photon Detector Design

The photon detectors used to detect the submillimeter wave signal were implemented using Kinetic Inductance Detector (KIDs) technology [27] developed in our group at Caltech and JPL. This section outline the physics and operating principles of these devices.

3.5.1 Physics of Microwave Kinetic Inductance Detectors

KIDs are pair-breaking, superconducting photon detectors. Electrons in the ground state of a superconductor are bound together to form Cooper pairs. This results in an energy gap in the electronic density of states, similar to semiconductors. The energy gap is typically a couple of meV and falls in the submillimeter frequency range. The

table 3.3 lists the values for some typical superconductors. When photons with energy higher than the Cooper pair binding energy (2Δ) are absorbed in a superconductor, the Cooper pairs are broken resulting in the formation of single electron quasi-particles (Figure 3.11). This quasi-particle density perturbation causes a measurable change in the surface impedance of the superconductor, which can be used to make a photon detector.

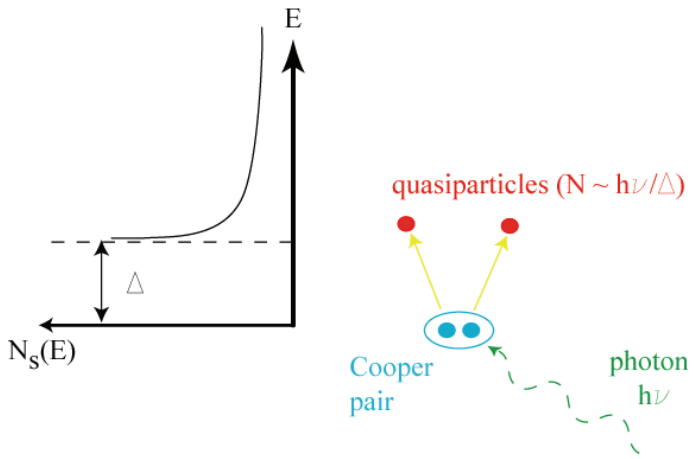

Figure 3.11: Schematic to explain Cooper Pair breaking in superconductors due to photon absorption. Cooper pairs at the Fermi energy break into quasi-particles when struck by a photon with energy $h\nu > 2\Delta$.

Figure 3.12 plots the change in surface reactance (δX_s), surface resistance (R_s), and quasi-particle density (n_{qp}) of the superconductor as a function of the temperature. The dependence of the thermal quasi-particle density on temperature can be

Superconductor	Energy Gap (meV)	Energy Gap (GHz)
Aluminum	0.375	90
Tantalum	1.45	350
Niobium	2.9	700

Table 3.3: Energy gaps of some typical superconductors in meV and GHz

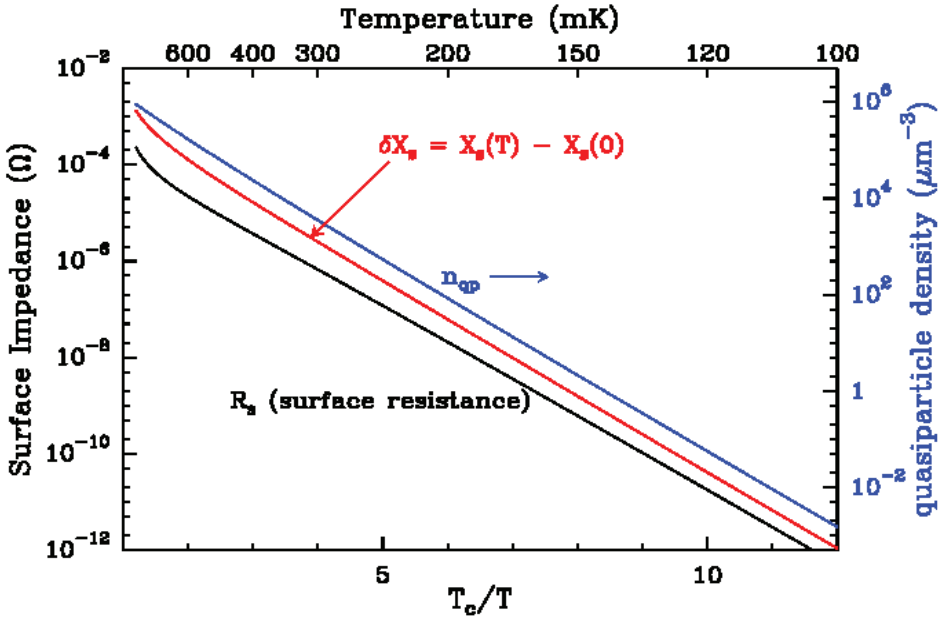

Figure 3.12: A plot showing surface resistance, change in surface reactance, and quasi-particle density in aluminum as a function of temperature at 10 GHz (Credit: Prof. Jonas Zmuidzinas)

calculated using:

$$n_{qp}(T) = 2N_0\sqrt{2\pi k_B T\Delta(0)}e^{-\Delta(0)/k_B T} \tag{3.8}$$

where N_0 is the single spin density of states at the Fermi energy, k_B is the Boltzmann's constant, $\Delta(0)$ is the energy gap at 0 K and T is the temperature. For Aluminum $N_0 = 1.72 \times 10^{10}/eV/\mu\text{m}^3$ including the electron-phonon enhancement factor [27].

The surface impedance change with temperature can be calculated using the Mattis-Bardeen theory [55]. The figure shows that the δX_s, R_s and n_{qp}, all decrease exponentially with the temperature which indicates that the responsivity of the detector remains constant so long as it is operated well below critical temperature of the superconductor. This can shown more rigorously as follows. The response of the superconductor to pair breaking submillimeter radiation may be quantified by change in surface impedance per change in quasi-particle density as:

$$\mathcal{R}_{nqp} = \frac{\delta L_s}{\delta n_{qp}} \tag{3.9}$$

For thin films the fractional change in surface inductance depends on fraction change in imaginary part of conductivity (σ_2) as:

$$\frac{\delta L_s}{L_s} = -\frac{\delta \sigma_2}{\sigma_2} \tag{3.10}$$

$\mathcal{R}_{nqp}$ can then be written as:

$$\mathcal{R}_{nqp} = -\frac{L_s}{\sigma_2}\frac{\delta \sigma_2}{\delta n_{qp}} \tag{3.11}$$

Using Mattis-Bardeen theory we have, assuming temperature much lower than superconductor's transition temperature:

$$\frac{\delta \sigma_2}{\delta n_{qp}} = -\frac{\sigma_2}{2N_0\Delta(0)}\left(1 + \sqrt{\frac{2\Delta(0)}{\pi^2\hbar\omega}}\right) \tag{3.12}$$

Using $L_s = \dfrac{1}{\sigma_2 t}$, for thin films, t being the film thickness, we get the final expression for $\mathcal{R}_{nqp}$ as:

$$\mathcal{R}_{nqp} = \frac{\delta L_s}{\delta n_{qp}} = \frac{1}{2N_0\Delta(0)\sigma_2 t}\left(1 + \sqrt{\frac{2\Delta(0)}{\pi^2\hbar\omega}}\right) \tag{3.13}$$

which is nearly independent of the temperature so long as the film is well below its superconducting transition temperature implying the same for the responsivity of the photon detector.

Small changes in Z_s of the superconductor (e.g., Al) can be sensitively measured by fabricating a transmission line resonantor out of it. The transmission line resonator is made using the coplanar waveguide geometry similar to that discussed in Chapter 2 and are readout using a similar homodyne measurement scheme. The ideal resonator response is given by (Figure 3.13):

$$S_{21}(\delta x) = \left[1 - \frac{Q_r}{Q_c}\frac{1}{1 + 2jQ_r\delta x}\right] \tag{3.14}$$

where $\delta x = \dfrac{f - f_r}{f_r}$, where f is the microwave readout frequency and f_r is the resonance frequency, Q_r and Q_c are the resonator total quality factor and coupling quality factor, respectively.

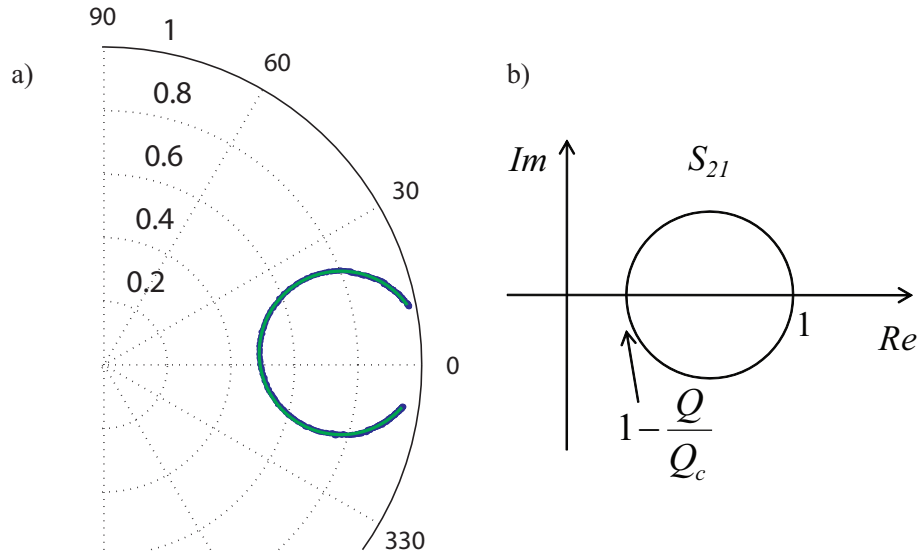

Figure 3.13: a) Polar plot of S_{21} data (thick blue line) and the fit (thin green line). The resonator has a resonance $f_r = 5.334$ GHz and $Q_r = 9866$. b) A schematic of the S_{21} plotted in complex plane

The magnitude of the complex response is seen as a dip in the microwave forward scattering parameter (S_{21}) at the resonance frequency (Figure 3.14). The figure also shows change in the response of the resonator as it is exposed to the submillimeter radiation of increasing intensity. The submillimeter radiation for this experiment was generated using a blackbody source whose temperature can be varied from 4 to 20 K in steps of 2 K. As the temperature of blackbody is changed the resonance frequency of the device changes by approximately 30 KHz for every 2 K change in blackbody temperature. The total change in the device resonance frequency and quality factor is 300 KHz and 1400 over the temperature sweep range starting with initial values

of 5.334 GHz and 9866, a fractional change of 5.6×10^{-5} and 0.1419, respectively. This happens due to the increase in surface impedance and quasi-particle number consistent with the trend in Figure 3.12. The total bandwidth of the resonator is close to 500 KHz and the above changes in Q_r and f_r are easily discernible.

The responsivity of the resonator can then be calculated as change in S_{21} per change in submillimeter power (P_{opt}) and can be written as:

$$\mathcal{R} = \frac{\delta S_{21}}{\delta x}\frac{\delta x}{\delta L_s}\frac{\delta L_s}{\delta n_{qp}}\frac{\delta n_{qp}}{\delta P_{opt}} \tag{3.15}$$

where $\frac{\delta L_s}{\delta n_{qp}}$ is given by equation 3.13 and $\frac{\delta n_{qp}}{\delta P_{opt}}$ defines the efficiency of the optical chain. Differentiating equation 3.14 we have

$$\frac{dS_{21}}{d\delta x} = \frac{Q_r^2}{Q_c}\left[\frac{d(1/Q_r)}{d\delta x} + 2j\right] \tag{3.16}$$

The total quality factor of the resonator is given by the usual formula $1/Q_r = 1/Q_c + 1/Q_i$ where the power lost to the outside world through the coupler limits Q_c and the resonator internal losses limit Q_i (See Table 3.4). The expression for Q_r is $Q_r = \frac{Q_cQ_i}{Q_c+Q_i}$ and the responsivity scales as $\mathcal{R} \sim \frac{Q_cQ_i^2}{(Q_c+Q_i)^2}$ which for small values of Q_c scales as $\mathcal{R} \sim Q_c$ and for large values of Q_c scales as $\mathcal{R} \sim 1/Q_c$. It is easily shown that the responsivity maxima occurs at $Q_c = Q_i$ by checking for the extremum of Q_r^2/Q_c with respect to Q_c where Q_i is the internal quality factor of the resonator under loaded conditions (See Table 3.4). The differential term inside the brackett in equation 3.16 is the change in the Q_r with the change in f_r due to change in the quasi-particle density due to the photon absorption and can be calculated using the Mattis-Bardeen theory.

3.5.2 Resonator Design

Figure 3.15 shows the photon detector. A hybrid design is used for the resonator where most of the coplanar waveguide is made using niobium superconductor but the

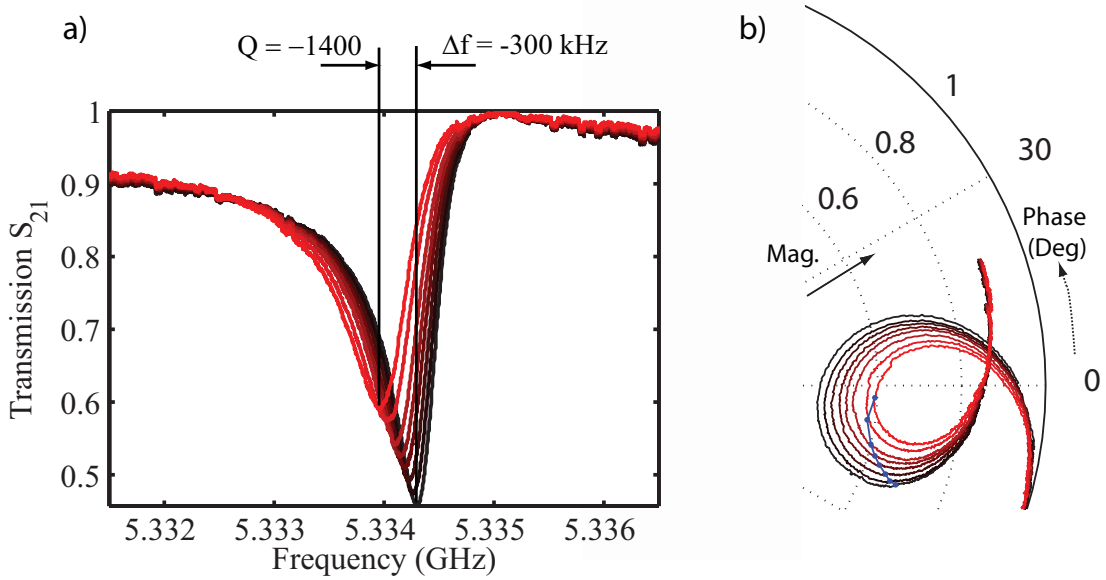

Figure 3.14: The forward transmission $|S_{21}|$ with change in submillimeter signal power. a) shows the change in magnitude of the response while b) plots the response change in the complex plane (similar to Figure 2.5). Blue lines and dots show the change in the complex response at a constant readout frequency. The measurement was performed using the circuit shown in Figure 2.4. As the submillimeter power is increased by raising the illuminating blackbody temperature from 4 to 20 K the curves are shown in color changing from black to red. The data shown is for a hybrid resonator (see Section 3.5.2) made using a 20 nm thick film of aluminum on sapphire substrate. The total length of the resonator is 3.5 mm

Mechanism	Approx. Q
Substrate loss	1,000,000
CPW radiation	1,000,000
Submm Microstrip Coupling	100,000
300 K Optical loading	15,000
Coupler length (150 μm on Si)	15,000

Table 3.4: Table for effects limiting resonator Q

sensitive short-circuited end of the resonator where the photons are absorbed is made out aluminum. Thickness of the niobium film is 2000 Å while that of aluminum

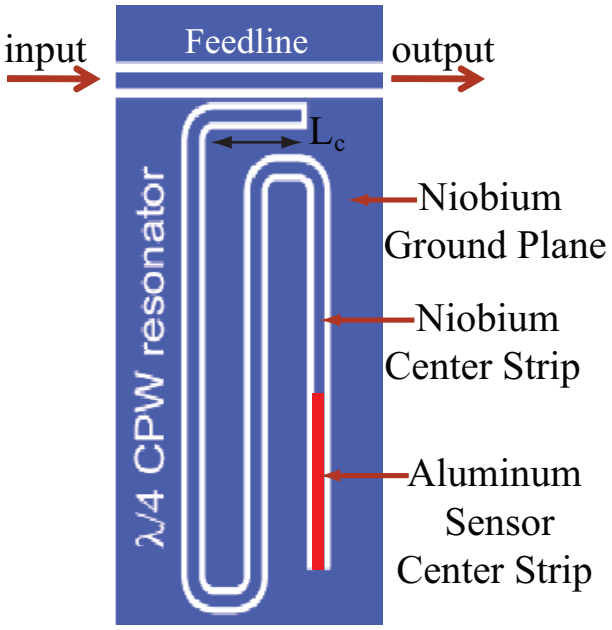

Figure 3.15: Schematic of a hybrid coplanar waveguide resonator used as a photon detector

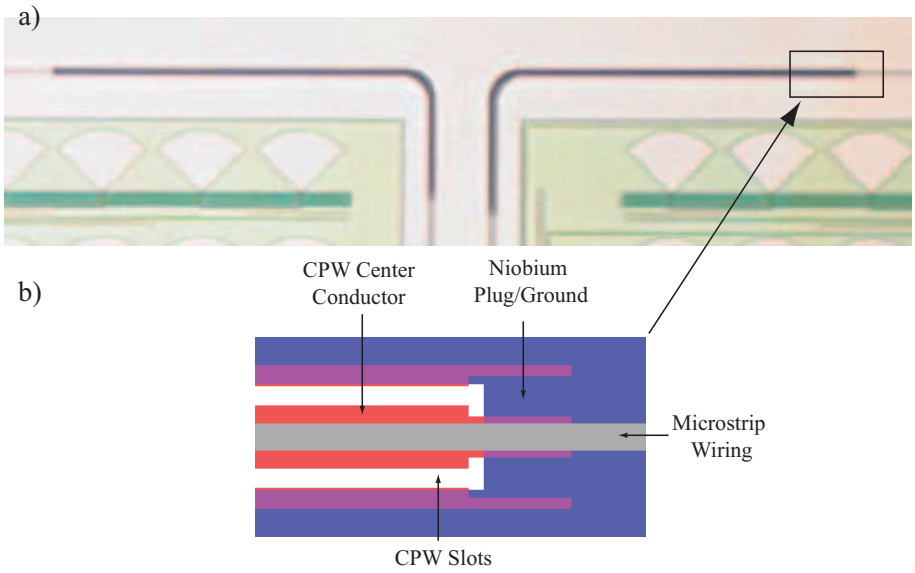

Figure 3.16: a) Picture of the submillimeter coupling section of the MKIDs with microstrip from the bandpass filter running over the aluminum part of CPW center strip. b) Schematic close up (not to scale) of submillimeter coupling end of the MKIDs. niobium ground plane is shown in blue. Aluminum layer is shown in orange, while the niobium wiring layer is shown in grey

Geometry (Center-Slot) (μm)	Coupling Constant (μm/GHz)^2
6-4	3.5×10^{10}
6-3	3.57×10^{10}
6-2	3.79×10^{10}
7-1	4.55×10^{10}
5-0.5	5.67×10^{10}
5-1	6.6×10^{10}

Table 3.5: Table for coupling strength for different CPW geometries

film is 200 Å. This design is necessary since making the entire coplanar waveguide using aluminum would cause the sub-mm radiation to couple to the resonator directly instead of through the antenna, feed network and bandpass filter channel since the thin aluminum film impedance matches the free space impedance well. This design also allows us to separate the two functionalities of photon absorption and detection in to two separate parts of the resonator allowing more freedom for design.

In addition to the coplanar waveguide geometry (i.e., the center conductor width and the slot spacing), the resonator design is completely specified by its resonance frequency, coupling quality factor, and length of the aluminum section. The total length of the resonator determines its resonance frequency. The resonator Q may be limited by multiple effects listed in Figure 3.4. We empirically know that the best substrates have given us internal Qs of close to 1 million. Coplanar waveguide radiative losses limit Qs to about the same order of magnitude [71], depending on the geomtery. Q limitations due to coupling to the submillimeter circuit can be estimated using SUPERMIX to be close to a 100,000. Calculations show, however, [72] that optical loading due to 300 K atmospheric emission will limit the Q to about 15,000. The coupling quality factor governed by the coupler length should match this value for maximum responsivity.

3.5.2.1 Total Length

Once the resonance frequency of the resonator has been specified the length of the resonator can be calculated using:

$$L = \frac{c}{4f_r\sqrt{\varepsilon_{eff}}} \tag{3.17}$$

where c is the speed of light and ε_{eff} is the effective dielectric constant seen by the electro-magnetic wave travelling in the CPW and ideally includes effects of superconductivity as well [57]. ε_{eff} can be estimated as $\varepsilon_{eff} = (\varepsilon_d + 1)/2$ where ε_d is the substrate dielectric constant.

3.5.2.2 Coupler Length

The coupler length can be ascertained by calculating the coupling capacitance between the feedline and coupling section of the resonator. The feedline geometery used was 10 μm center strip and 6 μm slots. The resonators used had a center strip of 6 μm and 2 μm slot width. Both the co-planar waveguides were separated by a 2 μm ground plane. In order to calculate the resonator Q_c the feedline and coupling section of the resonator can be simulated as a 3-port network (Figure 3.17) with coupling between port 1 and 3 defined by scattering parameter S_{31} related to the resonator Q_c as:

$$Q_c = \frac{\pi}{2\left|S_{31}\right|^2}. \tag{3.18}$$

Using the layout shown in Figure 3.17 the 3-port network may be simulated using SONNET to calculate the scattering parameter for different coupler lengths (L_c) and f_r. Assuming a linear dependence of transmission parameter S_{31} on f_r and L_c, which physically corresponds to a capacitive coupling between the resonator and the feedline it can be written as [73]:

$$S_{31} = Af_rL_c + Bf_r + CL_c + D. \tag{3.19}$$

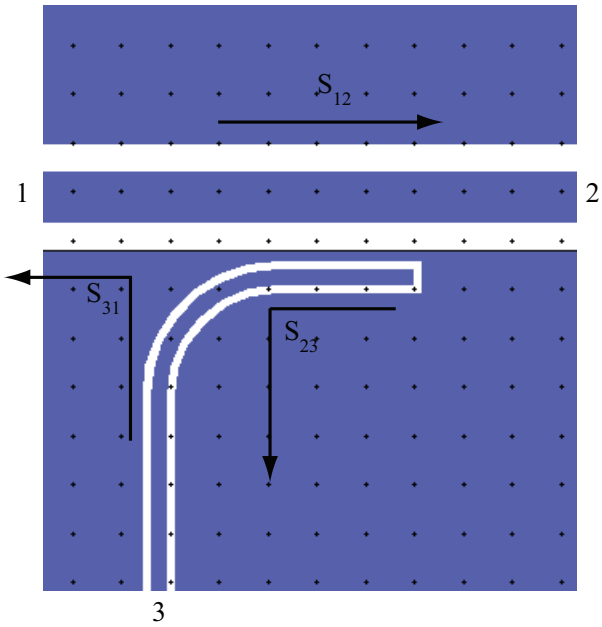

Figure 3.17: Three port network with ports 1 and 2 feedline input and output ports and port 3 the end of coupling section of the resonator

The data is fitted to the model in equation 3.19 to extract parameters A, B, C, and D [73]. Since the coupling is primarily capacitive for our design (Chapter 5), $Af_rL_c >> Bf_r, CL_c, D$. L_c for a given Q_c can then be calculated using:

$$L_c(\mu\text{m}) = \frac{1}{\text{f}_\text{r}(\text{GHz})}\sqrt{\frac{\text{A}}{\text{Q}_\text{c}}}. \tag{3.20}$$

Values for A are tabulated for different CPW geometries in Figure 3.5. Using these values and resonance frequency in GHz gives coupler lengths in μm.

3.5.2.3 Resonator-microstrip Submillimeter Overlap

The submillimeter radiation is coupled to the resonator by running the microstrip line over the CPW center strip as shown in Figure 3.16. The bottom layer for the microstrip is made using the aluminum part of CPW while the top layer remains niobium, with SiO_2 dielectric in between. The length of the aluminum section is decided by the length of overlap required to dump most of the submillimeter power from the

Device Parameters Inputs	
Frequency (GHz)	200
Temperature (K)	0.22
Characteristic Impedance (Ω)	24
Niobium Film Parameters Inputs	
Gap Voltage (mV)	2.9
Critical Temperature (K)	9.2
Resistivity (μΩ-cm)	2.5
Thickness (A)	2000
Aluminum Film Parameters Inputs	
Resistivity (μΩ-cm)	2.82
Thickness (A)	200
SiO_2 Dielectric Parameters Inputs	
Dielectric Constant	4
Loss Tangent	0.0001
Microstrip Properties Outputs	
Characteristic Impedance (Ω)	27.81
Propagation Constant (/mm)	5.03+j 9.6
Power Fraction Absorbed Outputs	**Length (mm)**
0.9	0.297
0.95	0.368
0.99	0.53
0.999	0.76

Table 3.6: Design parameters for the submillimeter coupler

microstrip to the CPW. This was calculated using SUPERMIX, and the length of CPW and microstrip overlap required to dump close to 100% of the submillimeter power at 200 GHz was determined to be 1 mm. The table 3.6 shows the parameter values used for the SUPERMIX simulations and the corresponding outputs.

Making the submillimeter coupling section long will result in microwave (4-12

GHz) readout signal to leak out from the coupler and lower the quality factor of the resonator, but for the low coupling quality factors close to 15,000 used in our designs this is not a major issue.

Also it is essential that the section of aluminum under the ground plane and the CPW resonator be electrically connected using niobium and not aluminum to prevent the quasi-particles in the center strip from escaping into the ground and lowering the response of the device. The details of the 'niobium plug' which prevents this from happening are as shown in Figure 3.16b.

3.6 Fabrication Steps

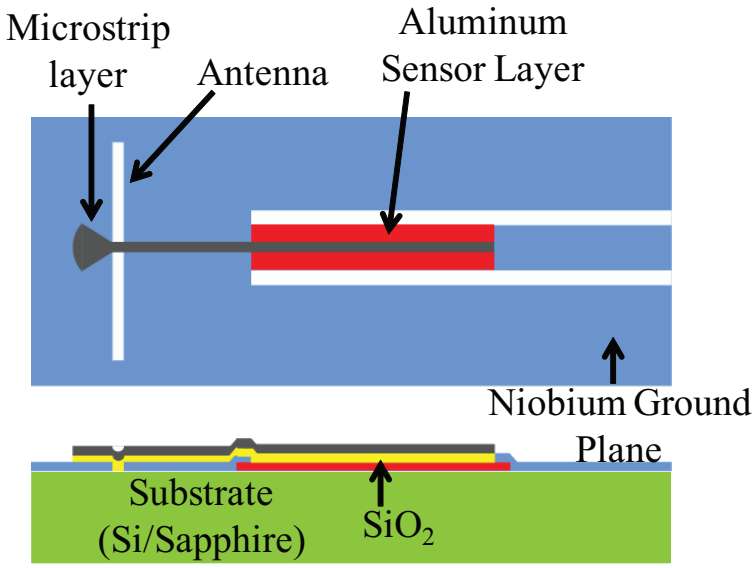

Figure 3.18: Schematic of pixel showing the various layers required for pixel fabrication

Figure 3.18 shows the various layers of material used to fabricate the pixel. The aluminum sensor layer is first deposited on the silicon (or sapphire) substrate using DC magnetron sputtering. The sensor layer is then patterned using photoresist and BCl_3/Cl_2 inductively coupled plasma (ICP) etching. The niobium ground plane is deposited using DC magnetron sputtering. The ground plane is patterned using

photoresist and SF_6 ICP etching. SiO_2 is deposited by RF magnetron sputtering with a substrate bias. The vias on the niobium ground plane are patterned using photoresist and CHF_3/O_2 ICP etching. The wiring layer of the niobium microstrip is deposited using DC magnetron sputtering and is patterned using BCl_3/Cl_2 ICP etching. The dielectric is removed using photoresist and CHF_3/O_2 ICP etching. Finally, CPW is patterned using photoresist and BCl_3/Cl_2 ICP etching.

3.7 Conclusions

We have designed and tested various components necessary to implement a submillimeter pixel on chip. The antenna was implemented using a multi-slot structure on chip. The antenna has a narrow beam and does not require any extra on-chip optics to couple the light from the telescope. The submillimeter power from the antenna slots is combined using binary tree feednetwork which brings it out into a single output microstrip which then passes it through inline BPFs (see Chapter 4). The antenna and the microstrip were implemented using niobium and SiO_2 dielectric. The photon detectors were implemented using microwave kinetic inductance detectors. The submillimeter power is coupled from the output microstrip to the detector by running the microstrip over the shorted end of MKIDs made out of aluminum. The detector response is measured as change in the transmitted readout microwave signal using a through line capacitively coupled to the resonator. The complete layout of the single pixel schematic is shown in Figure 3.19. Figure 3.20 shows a photograph of an actual pixel taken using the optical microscope.

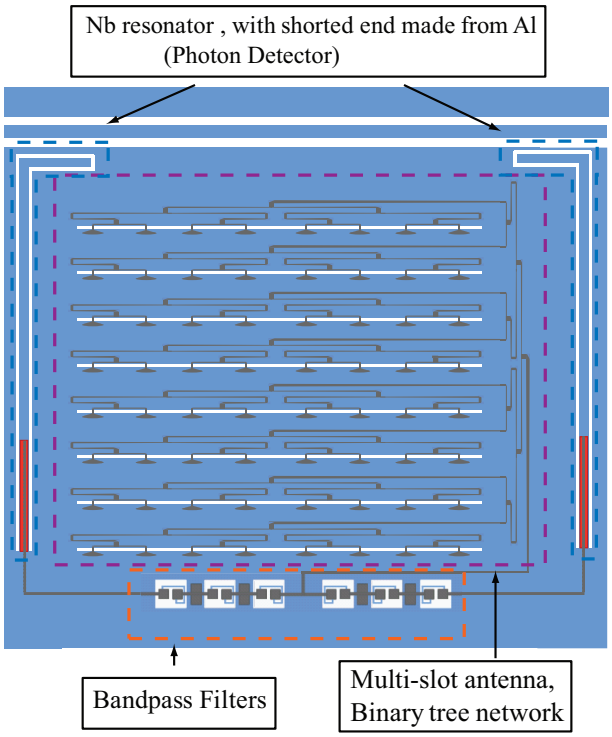

Figure 3.19: Schematic of the final pixel with all the sub-components put together. It shows 8 slots and 8 taps on each slot making up the antenna for clarity, the actual number is 16 for both (Figure 3.20).

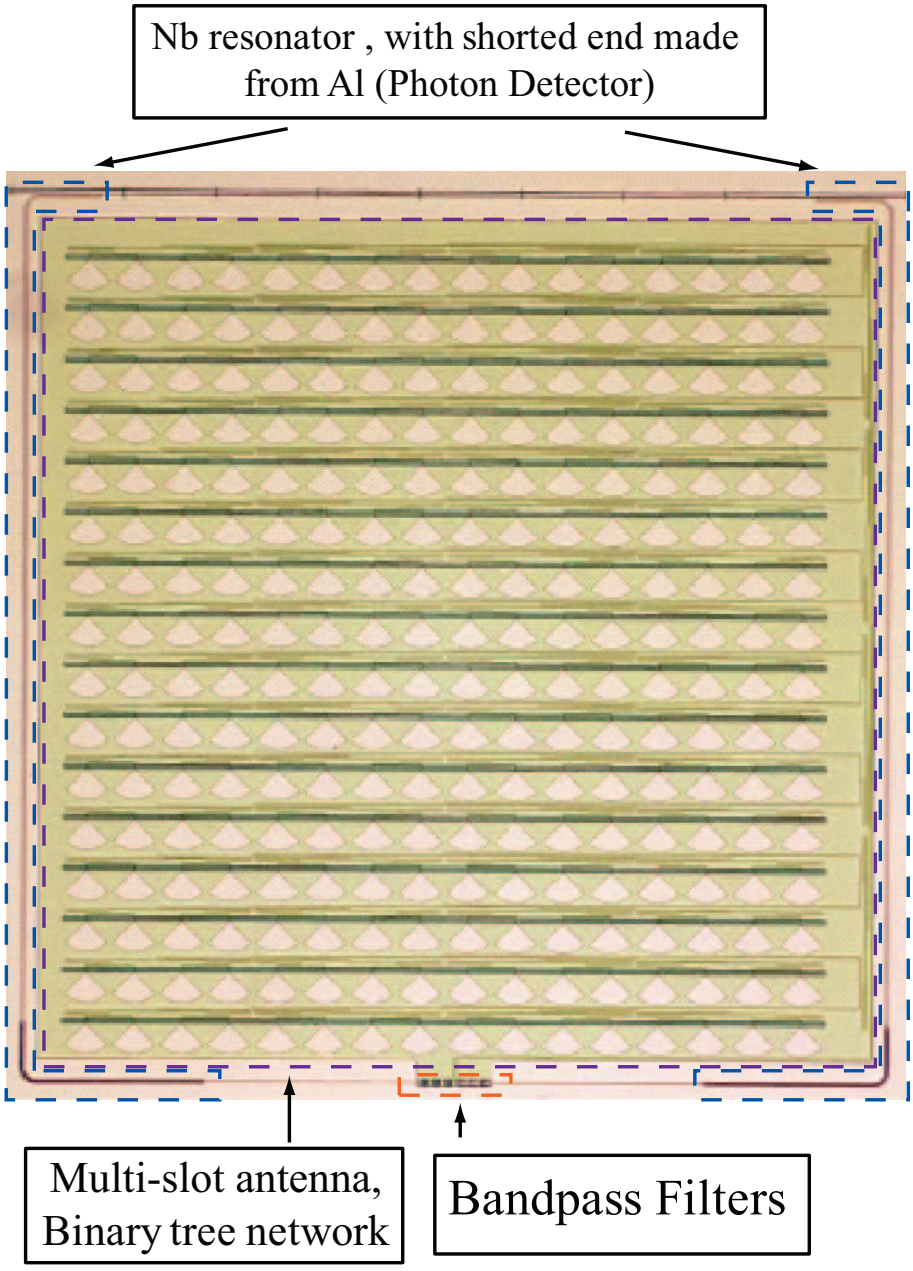

Figure 3.20: Picture of the two-color pixel taken under an optical microscope

CHAPTER IV

BANDPASS FILTER DESIGN

4.1 Introduction

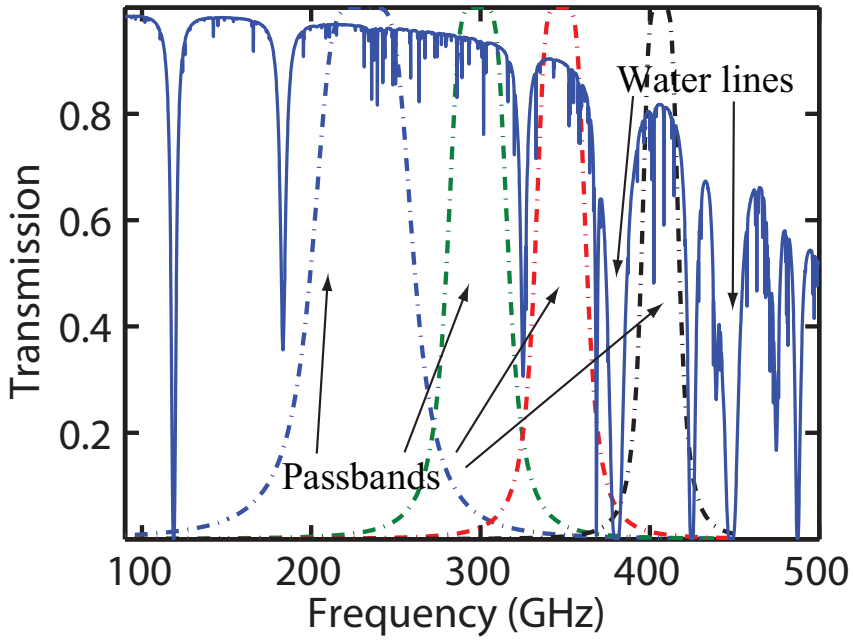

Figure 4.1: Atmospheric transmission spectrum (solid line) at CSO overlaid on the ideal filter responses (dotted lines) calculated using the inductor and capacitor values given in Table 4.1. The atmospheric spectrum was generated using the program atm_cso [74] (http://www.submillimeter.caltech.edu/cso/weather/atplot.shtml).

The opacity of the Earth's atmosphere obscures portions of the sub-THz sky to ground-based astronomical observation. This requires that band-defining filters be used in conjunction with broad-band antenna and detectors to construct pixels working at mm-submillimeter wavelengths to reduce the loading on the detectors from the Earth's atmosphere. This chapter presents the design and testing of superconducting, lumped-element, on-chip bandpass filters (BPFs), placed inline with the microstrip

connecting the antenna and the detector, covering the frequency range from 209-416 GHz. Four filters (BPF 1, 2, 3, and 4) were designed with passbands of 209-265 GHz, 274-315 GHz, 335-361 GHz and 397-416 GHz, corresponding to the atmospheric transmission windows shown in Figure 4.1. The first atmospheric window extends from 200-320 GHz and is divided into two roughly equal parts by BPFs 1 and 2. Fourier transform spectroscopy (FTS) was used to verify that the spectral response of the BPFs is well predicted by the computer simulations. Two-color operation of the pixels was demonstrated by connecting two detectors to a single broadband antenna through two BPFs. A new pixel design allowing four-color operation is also discussed.

There are various existing designs for defining the passbands of mm-submillimeter-wave pixels. Metal-mesh filters [64] have been used in conjunction with IR blocking materials such as teflon and fluorogold to make quasi-optical filters that can be mounted on the dewar windows or device box. This approach, however, has the disadvantage of preventing multi-color pixel operation, since the entire array is irradiated by the same frequency band. Multi-color pixel operation is desirable for upcoming camera designs [75] to increase the overall throughput for a wide field survey by capturing more photons in different frequency bands. This has many advantages, as listed in Chapter 1, and additionally uses the focal plane more efficiently. Further, the quasi-optical mesh filters are optimally designed for normally incident radiation. Obliquely incident radation may leak through and load the detector. Since these filters are mounted on the dewar windows they need to be carefully heat sunk to prevent detector loading due to radiation emitted by the filters themselves. Multiple filters and IR blockers in the optical chain also need to be coated with anti-reflection (AR) films to prevent non-uniform transmission as a function of frequency in the filter passband, due to standing waves present because of the refractive index mismatch at the interfaces of adjacent optical components.

Although we chose to use lumped-element designs, on-chip bandpass filters may

also be implemented using distributed circuit elements [39]. However, using distributed circuit elements causes the bandpass filters to leak at higher harmonic frequencies requiring a cascaded lowpass filter. This adds to the complexity of the circuit and takes up precious real estate on the chip. The lowpass filter may also be implemented using a metal mesh filter again leading to some of the issues mentioned above.

The lumped-element, on-chip bandpass filters presented in this chapter circumvent all the above problems.

4.2 Bandpass Filter Design

4.2.1 Lumped–Element Circuit Design

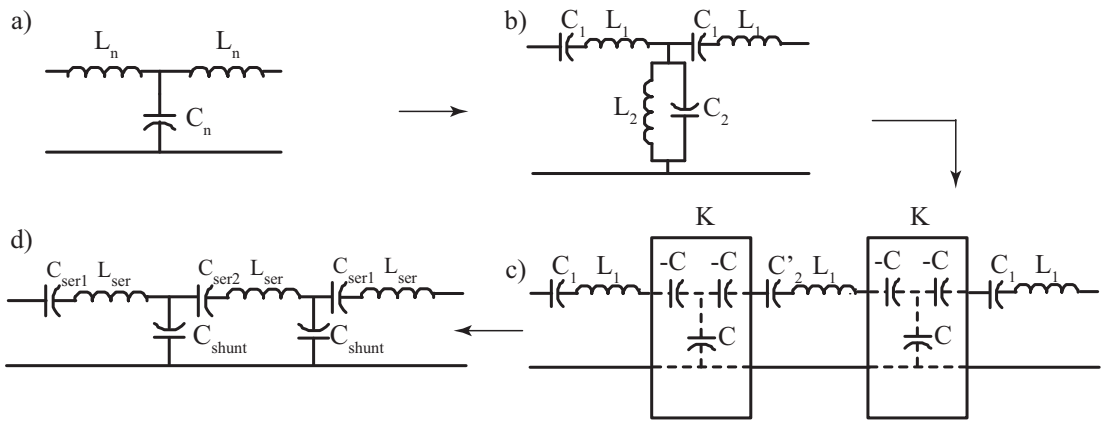

Figure 4.2: Steps for lumped-element bandpass filter circuit design: a) 3-pole Butterworth low-pass filter prototype. L_n and C_n are normalised inductor and capacitor, respectively. b) Bandpass filter with series LC and shunt parallel LC resulting from the prototype low-pass filter. c) Bandpass filter with impedance inverter blocks and no shunt inductors. d) Final lumped-element bandpass filter circuit with no shunt inductors

We use a three-element Butterworth lowpass filter prototype (Figure 4.2a) with cutoff at $\omega_c = 1$ and terminated in a 1 Ω load as a basis for design of our bandpass filters. Using a Butterworth prototype should minimise any ripples in the filter pass or stop bands. This normalised lowpass filter has element values $L_n = 1$, $C_n = 2$

Element values	BPF1 209–265 GHz	BPF2 274–315 GHz	BPF3 335–361 GHz	BPF4 395–416 GHz
L_{ser} (pH)	75	123.2	146.91	201.04
C_{ser1} (fF)	7.37	2.48	1.50	0.79
C_{ser2} (fF)	9.01	2.69	1.59	0.82
C_{shunt} (fF)	40.23	31.36	26.97	23.1

Table 4.1: Circuit element values for Figure 4.2 d) for the BPFs corresponding to the atmospheric transmission windows

(Figure 4.2a). It is converted to a lumped-element bandpass filter using the usual transformations [68], and replacing the series inductor by a series combination of inductor ($L_1 = \frac{Z_0 L_n}{\omega_0 \Delta}$) and capacitor ($C_1 = \frac{\Delta}{Z_0 L_n \omega_0}$), and shunt capacitor by a parallel combination of inductor ($L_2 = \frac{Z_0 \Delta}{C_n \omega_0}$) and capacitor ($C_2 = \frac{C_n}{Z_0 \Delta \omega_0}$) (Figure 4.2b). Z_0 is the embedding impedance set by the characteristic impedance of the microstrip transmission line which brings submillimeter power from the antenna and is equal to 20 Ω. Δ ($= \omega_{c2} - \omega_{c1}$) is the design bandwidth of the BPF and ω_0 ($= \sqrt{\omega_{c1}\omega_{c2}}$) is the center frequency of the BPF given by the geometric mean of the 3 dB cutoff frequencies of the BPF. ω_{c1} and ω_{c2} are the upper and lower cutoff frequencies of the bandpass filter, respectively.

For the ease of fabrication of the circuit it cannot have any shunt inductors to ground. For sufficiently narrow bandwidth (10−20%) impedance inverters can be used to replace a parallel shunt admittance (Y_p) by a series impedance (Z_s) for two-port networks [76] (Figure 4.2c). Using the identity $Z_s = K^2 Y_p$, where $Z_s = j\omega L_1 + \frac{1}{j\omega C_2'}$, $Y_p = j\omega C_2 + \frac{1}{j\omega L_2}$, and K is the impedance inverter, we get the value for K and series capacitance $K^2 = L_1/C_2$ and $C_2' = L_2 C_2 / L_1$.

The impedance invertor is implemented using a two-port T network with the series

branches containing capacitors $-C$ and shunt branch containing capacitor C where $C = 1/\omega_0 K$ (Figure 4.2c). The negative capacitance in the series branches can be absorbed into C_1 and C_2' to give the final circuit (Figure 4.2d). Here $L_{ser} = L_1$, $C_{shunt} = C$, $C_{ser1} = \dfrac{CC_1}{C - C_1}$, and $C_{ser2} = \dfrac{CC_2'}{C - 2C_2'}$.

The lumped circuit element values are then further optimised using HP-ADS [77], a circuit simulation software package, to give a power transmission of at most 10^{-4} in stop band, unity transmission in passband with sharpest possible rolloff. These optimised values for various lumped components for the four bandpass filters are listed in Table 4.1.

4.2.2 Circuit Layout and Fabrication

The schematic of the filter layout is shown in Figure 4.3. The integrated inline BPF circuit was fabricated on chip with the other pixel components using photolithography. The inductors were implemented using spiral geometry and the capacitors in the parallel plate configuration. The bottom layer is 200 nm thick niobium film deposited on the silicon substrate using DC magnetron sputtering. The ground plane, spiral inductors (Figure 4.3 shown in blue) and lower plate of the parallel plate capacitors (not visible in Figure 4.3) are patterned on this layer using photoresist and SF_6 Inductively Coupled Plasma (ICP) etching. Following this, a 400 nm thick SiO_2 dielectric layer is deposited on the bottom layer by RF magnetron sputtering with substrate bias. Subsequently, a 200 nm thick layer of niobium is deposited using DC magnetron sputtering and patterned using BCl_3/Cl_2 ICP etch to form the wiring layer of microstrip geometry (Figure 4.3, shown in pink). The dielectric is then removed using a CHF_3/O_2 ICP etch.

The input microstrip brings the broadband submillimeter power from the slot antenna to the filter (Figure 3.20). In order to avoid making a via between the bottom niobium layer and the top, the first series capacitor is divided into two series

capacitors each having double the design capacitance ($C_{LSer1} = 2\,C_{ser1}$) and placed on either side of the spiral inductor as shown in Figure 4.3a. The microstrip line connects the second series capacitor to the shunt capacitor. This design is then repeated for the remaining two series capacitor-inductor sections. Finally, the output microstrip takes the band limited submillimeter power to the detector.

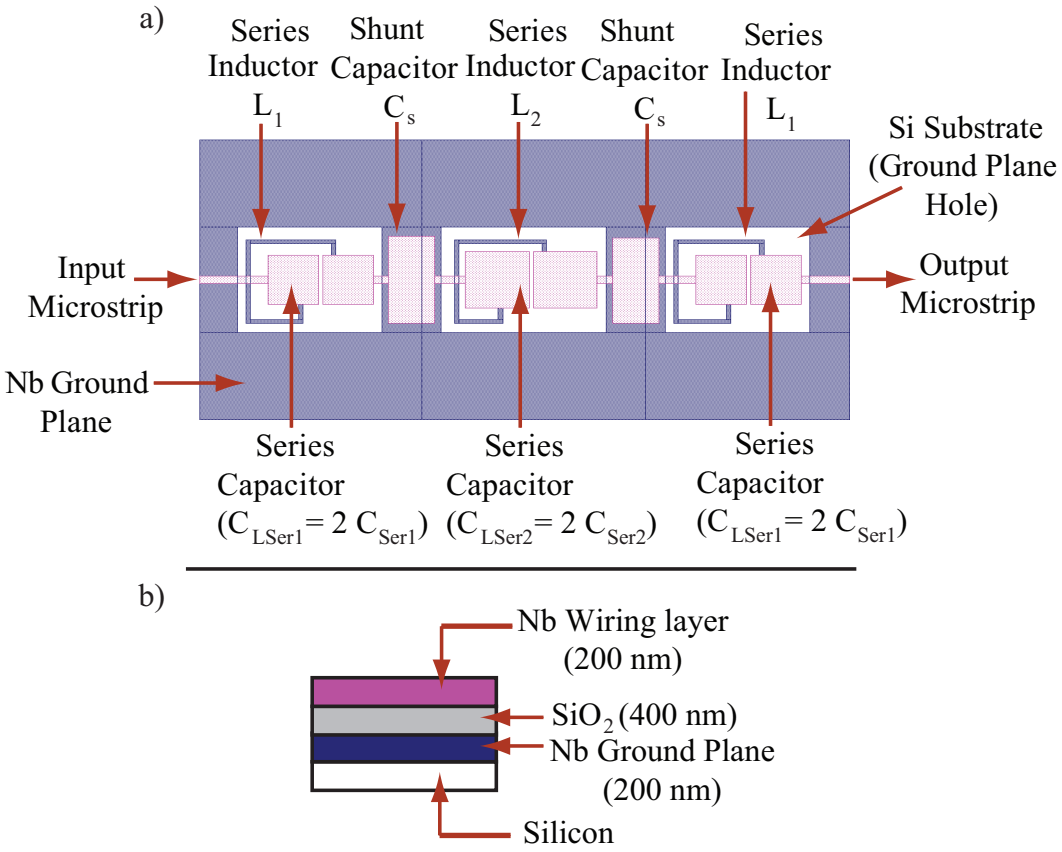

Figure 4.3: SONNET layout for the bandpass filters: (a) top view, b) side view. The top microstrip is made of niobium (pink). Below it is a layer of SiO_2 (grey, not visible in the top view), then niobium ground plane (blue). The series inductors and capacitors are fabricated on top of the sapphire substrate (white) directly in holes in the ground plane.

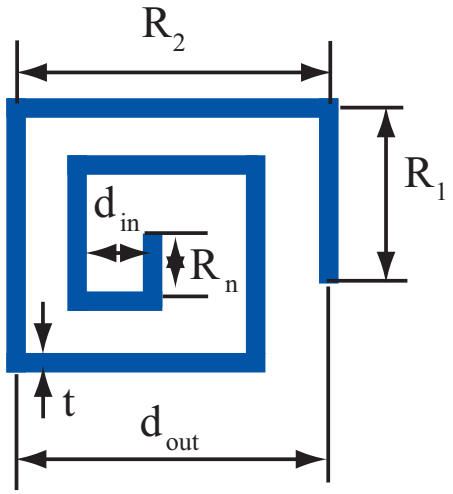

Figure 4.4: Spiral inductor schematic detailing the dimensions used in the inductor design. R_n is the length of the n^{th} arm of the spiral inductor with $n = 1$ for the outermost arm. d_{out} and d_{in} are the outermost and innermost dimension of the inductor, respectively. t is the trace width.

4.2.3 Component Design

4.2.3.1 Spiral Inductor Design

Correct design of the inductor is critical for the optimal performance of the bandpass filter. The inductor may either be implemented using the CPW geometry which is simpler to layout but can provide relatively smaller inductance values, or a spiral geometry, which was finally used for our design. To make the design choice we calculated the length of CPW required to provide the minimum required inductance of 75 pH, as follows.

Let Z_0 (= 20 Ω), Z_c (= 50 Ω), ε_d (= 10.5), f (= 250 GHz) be the characteristic embedding impedance of the external circuit, characterstic impedance of CPW used to implement the lumped inductor, substrate (sapphire) dielectric constant and the filter center frequency, respectively. The effective dielectric constant seen by the EM wave is close to $\varepsilon_{eff} = (\varepsilon_d + 1)/2 = 5.75$. This may be calculated more accurately using SONNET simulations.

Using equations for transmission line characteristic impedance and propagation

	BPF 1		BPF 2		BPF 3		BPF 4	
	L_1	L_2	L_1	L_2	L_1	L_2	L_1	L_2
R_1	3.5	2.5	5.5	5	7	7	7.5	7.5
R_2	19.5	20	17.5	17.5	15.5	15.5	15.5	15.5
R_3	21	21	21	21	17	17	16.5	16
R_4	12	10	14.5	14.5	12.5	12.5	12.5	12.5
R_5	4.5	2.5	8	8.5	13	13	12.5	12
R_6	0	0	2.5	2.5	5	5.5	9.5	9.5
R_7	0	0	0	0	3	3	8	8
R_8	0	0	0	0	0	0	3.5	3
t	1	1	1	1	1	1	1	1

Table 4.2: Spiral inductor dimensions for all the bandpass filters with schematic shown in Figure 4.4. L_1 and L_2 are shown in the SONNET layout for the BPF, in Figure 4.3a. The values for L_1 and L_2 are nominally equal (Table 4.1) and their dimensions are close to each other. However, they end up with slightly different dimensions while tweaking the layout in SONNET due to the small difference in geometry of the capacitors C_{LSer1} and C_{LSer2}. All the dimensions are in microns.

constant we can get the inductance per unit length:

$$Z_c = \sqrt{\frac{\mathcal{L}}{\mathcal{C}}},\ \beta = \omega\sqrt{\mathcal{L}\mathcal{C}} \tag{4.1}$$

$$\mathcal{L} = \frac{\beta Z_c}{\omega} = \frac{\sqrt{\varepsilon_{eff}} Z_c}{c} \tag{4.2}$$

where $\mathcal{L}, \mathcal{C}$ are inductance and capacitance per unit length, c is the speed of light, β is the propagation constant, and ω is the frequency in radians/sec. The wavelength of the EM wave in sapphire at 250 GHz is 500 μm. Using equation (4.2) the length of CPW line required to implement inductance ($L = 75$) pH lumped inductor is $l = \dfrac{Lc}{\sqrt{\varepsilon_{eff}} Z_c} = 187.67$ μm, which is a significant fraction of the wavelength. Hence, a 75 pH inductor implemented using CPW with the above Z_c will behave like a distributed element. This will cause the filter to leak at integral multiples of the transmission line fundamental mode.

Following [76] we can calculate the maximum inductance we can extract from CPW geometry with the above characteristic impedance at frequencies of interest ($\simeq$ 250 GHz) for a given error, as follows: The input impedance for the lumped element is given by:

$$Z_{in} = Z_c \frac{Z_0 + jZ_c t}{Z_c + jZ_0 t} \tag{4.3}$$

where $t = \tan(\beta l)$. Since we want to use sections of CPW much shorter than the wavelength and use high characteristic impedance sections to emulate inductors we can use the approximation $Z_0^2 t^2 << Z_c^2$. This gives us:

$$Z_{in} = Z_0 + Z_0 t^2 \left(1 - \frac{Z_0^2}{Z_c^2}\right) + jZ_c t \left(1 - \frac{Z_0^2}{Z_c^2}\right). \tag{4.4}$$

Comparing the real and imaginary parts of equation (4.4) to expression for input impedance of ideal lumped inductor $Z_{in} = Z_0 + jX_l$ we get $X_l = Z_c t \left(1 - \frac{Z_0^2}{Z_c^2}\right)$. To have the real part of the impedance match closely with the ideal case we need $t^2 \left(1 - \frac{Z_0^2}{Z_c^2}\right) \rightarrow 0$. Assuming, a 5% error in real part of the imepdance (i.e., $t^2 \left(1 - \frac{Z_0^2}{Z_c^2}\right) = 0.05$) we get $\beta l = 0.26$. Using equation (4.2) we get maximum value for lumped-element inductance using this scheme $L = 8.28$ pH, which is much less than the value needed.

A spiral geometry for the inductor can instead be used to provide the high values of the inductance needed for the bandpass filters. The rectangular spiral (Figure 4.4) was chosen for layout convenience and the geometry was guessed by calculating the inductance using the formulae available in the literature [78]:

$$L = \frac{\mu n^2 d_{avg} c_1}{2} (\ln(c_2/\rho) + c_3\rho + c_4\rho^2) \tag{4.5}$$

$$\rho = \frac{d_{out} - d_{in}}{d_{out} + d_{in}} \tag{4.6}$$

$$d_{avg} = \frac{d_{out} + d_{in}}{2} \tag{4.7}$$

Here L is the inductance and c_1, c_2, c_3, and c_4 are geometry dependent co-efficients with values 1.27, 2.07, 0.18, and 0.13, respectively, for rectangular spiral geometry. ρ is the filling fraction, with d_{in} and d_{out} the innermost and the outermost dimensions of the inductor (Figure 4.4), μ is the magnetic permeability, and n is the number of turns. This formula is not very accurate for large values of s/w where s is spacing between the traces and w is the trace width, but exhibits maximum error of $\sim 8\%$ when $s \leq 3w$ for regular spirals [78]. s is typically 2-4 μm, while w is 1 μm, and the formula works well as a zeroth order approximation since, in the final design, the s changes from one turn to the next. The final inductor geometry is obtained by laying it out in SONNET [79], simulating its impedance, and re-optimising the geometry to give the desired inductance value. The optimization is done keeping in mind the trends that decreasing the spacing between adjacent traces increases their coupling and hence the mutual inductance, and vice versa, and that the orthogonal traces are decoupled from one another. The trends suggested by the formulae in equation (4.5), such as dependence on the number of turns are also used. The exact final dimensions of each of the inductors finally used to implement the BPFs are tabulated in Table 4.2.

4.2.3.2 Capacitor Design

The dimensions for the capacitor with capacitance values tabulated in Table 4.1 can be estimated using parallel plate formula $C = \varepsilon_0 \varepsilon_d A/d$, where ε_0 is the free space permittivity, ε_d $(= 4)$ is the dielectric constant of SiO_2, A is area of the parallel plates, and d is the thickness of SiO_2 (which is same as distance between the plates). The capacitor dimensions were further optimised by laying out capacitor-inductor series combinations in SONNET and optimizing the dimensions of the layout so that it has a resonance at the same frequency as the series combination of lumped LC with values in the table 4.1.

The final dimensions of the capacitors for each of the filters are tabulated in Table 4.3. As can be seen, the values calculated using the parallel plate formula can be significantly different from the values finally obtained through simulations.

	BPF 1			BPF 2			BPF 3			BPF 4		
	C_{Lser1}	C_{Lser2}	C_{shunt}	C_{Lser1}	C_{Lser2}	C_{shunt}	C_{Lser1}	C_{Lser2}	C_{shunt}	C_{Lser1}	C_{Lser2}	C_{shunt}
Length	11.5	14.5	10.5	8	5	10.5	7	4.5	11.5	3.5	4.5	10
Width	13	15	23	9	7.5	19.5	6	7.5	17.5	5	5	10

Table 4.3: Dimensions of the capacitors in Figure 4.3a in microns assuming a 4000 Å thick SiO_2 dielectric ($\varepsilon_d = 4$). The actual capacitance value of these capacitors $C_{LSer1,2} = 2C_{Ser1,2}$, since two equal value series capacitors are being used to implement the series capacitor shown in circuit schematic Figure 4.2d. The dimensions of the parallel plate capacitors used to implement first and third series capacitor in Figure 4.2d are exactly the same. Length direction is assumed to be the direction of propagation of submillimeter radiation.

4.2.3.3 SONNET Simulations

The response of each of the circuit elements, and subsequently the entire layout, was simulated using SONNET [79] – a planar 3D electromagnetic simulator. The software uses method of moments calculation to compute the response of the circuit. The SONNET layout of the BPF is seen in Figure 4.3. Initial simulations assumed the niobium ground plane and wiring layers (seen in blue and pink respectively) to be perfectly conducting 2D sheets (zero thickness) with 400 nm SiO_2 dielectric between them. The lumped-element geometries were optimised to produce the required bandpass filter response.

4.2.4 Effect of Superconductivity on the Filter Response

Niobium is used to fabricate the bandpass filters superconducts at the detector operating temperatures (niobium $T_c = 9.2$ K, $T_{op} = 220$ mK). Superconductors have a

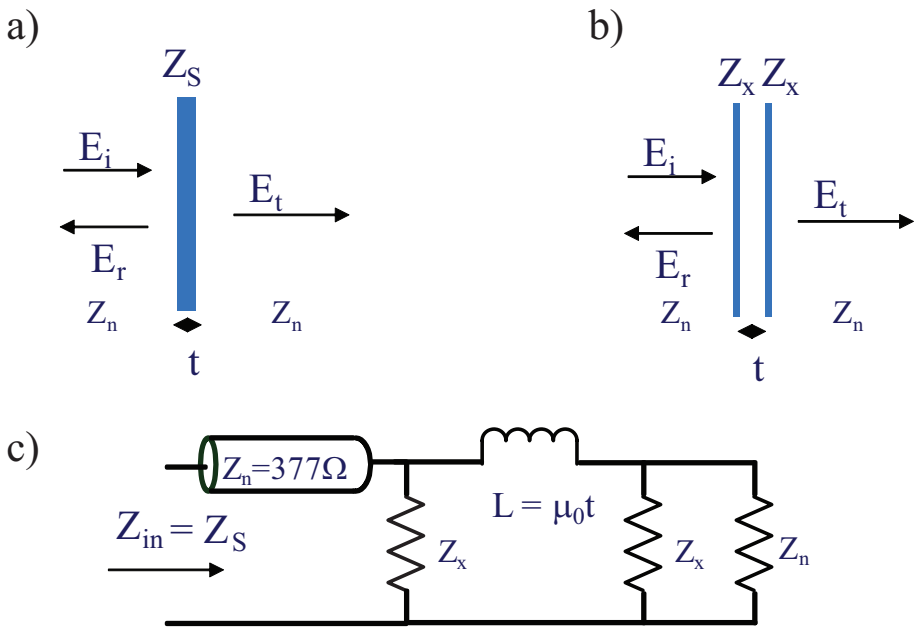

Figure 4.5: a) A superconducting film of thickness t with surface impedance Z_s. Z_η is the free space impedance, E_i, E_r, and E_t are the incident, reflected, and transmitted waves, respectively. b) A SONNET analog for schematic a)–two planar sheets separated by distance t having surface impedance Z_x where Z_x is related to Z_s by equation 4.9. c) Equivalent transmission line circuit for the schematics

finite surface impedance at microwave and submillimeter wavelengths [55], and simulating them as 2D planar films of perfect conductors can lead to significant errors in the bandpass filter response calculation.

SONNET can be used to accurately simulate the bandpass filter response by incorporating the effects of superconductivity and finite conductor thickness. This can be done by replacing a single perfectly conducting planar sheet with multiple planar sheets of a given surface impedance (Z_x), different from the the actual surface impedance (Z_s) of the superconducting film, as a model for thick superconducting film [65, 80]. For $\lambda_L \simeq t$ a two-sheet model is sufficient (Figure 4.5a,b) [80].

In the local limit, at temperature well below T_c and frequency well below the gap frequency, assuming $Z_\eta (= 377\Omega) >> \omega\mu_0\lambda_L (= 0.14\ \Omega)$ where Z_η is the free space impedance, and μ_0 is free space permeability, the surface impedance of the

superconductor is given by [80]:

$$Z_s = j\omega\mu_0\lambda_L \coth(t/\lambda_L). \tag{4.8}$$

The impedance seen by a TEM mode travelling along a transmission line is the same as the surface impedance seen by an EM wave normally incident upon a conductor [81]. Using this, the resulting equivalent circuit for the SONNET model in Figure 4.5b is shown in Figure 4.5c. If the distance between the sheets is much smaller than the wavelength of incident light, an inductor with a value of $\mu_0 t$ can be used to represent the impedance due to magnetic field energy stored between the sheets in Figure 4.5b.

Equating the input impedance Z_{in} of the transmission line equivalent circuit for the film is the surface impedance Z_s. We can solve for Z_x:

$$Z_x = Z_s \left[1 - \frac{t}{2\lambda_L \coth(t/\lambda_L)} + \left(1 + \frac{t^2}{4\lambda_L^2 \coth^2(t/\lambda_L)} \right)^{1/2} \right]. \tag{4.9}$$

Dividing Z_s and Z_x by ω gives us a surface inductance (L_s) of 88.5 fH and a modified surface inductance (L_x) of 0.1166 $pH/\square$.

The above changes in geometry and material properties were incorporated in the SONNET simulations done earlier with single perfectly conducting sheets. The dimensions of the bandpass filter layout were re-optimized to give the new corrected bandpasses (Figure 4.6). The final layout schematic is shown in Figure 4.7, and the corresponding dimensions are given in Table 4.4. The actual optical image of one of the bandpass filters (BPF 1) is seen in Figure 4.8.

4.3 Measurements and Results

Figure 4.9 shows the normalised, predicted and measured responses of the bandpass filters. The measurement was performed using a Fourier Transform Spectrometer (FTS). Details of the FTS construction are given in [82].

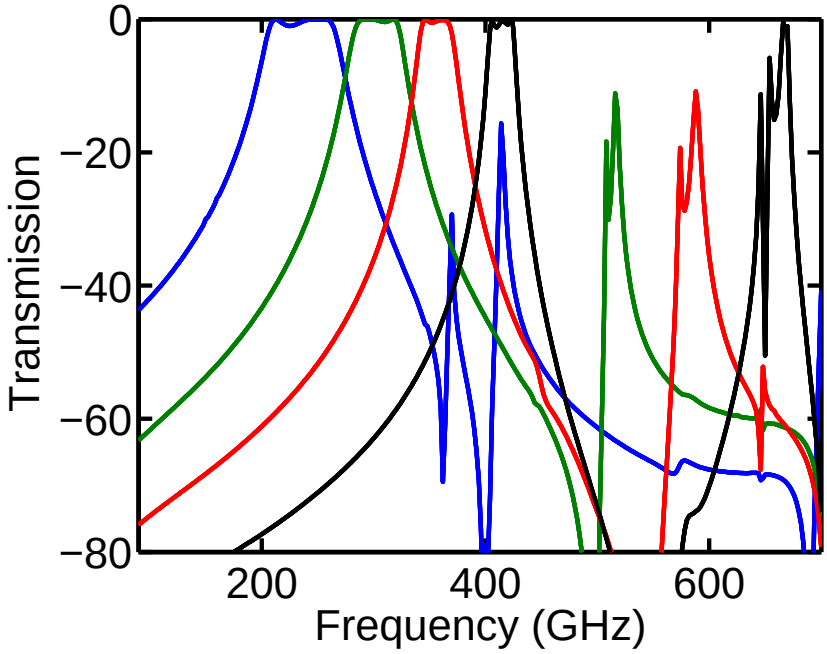

Figure 4.6: Bandpass filter response from 90 GHz, where the detector starts becoming responsive (Section 3.5) to 700 GHz where Niobium starts to become lossy.

There is excellent agreement between simulated and measured BPF responses for all 4 bandpass filters. The upper and the lower cutoff frequencies are close to their design values. The filters have sharp turn-ons and turn-offs, and the designed bandwidth also matches the measured value closely.

Fringing is observed in the passband of the filter, but this may be due to the dewar optics. Figure 4.10 shows the various dielectrics with their thicknesses used to make the dewar windows separating the different temperature stages. The fringing in the passband of the filter response may be occuring due to the standing waves in the optical chain due to dielectric constant mismatch between the windows. We further confirm that the fringing is not a characteristic of the filter passband by comparing it with the passband response of a pixel which does not have an inline filter between the antenna and the detector (Figure 4.11). Fringing is seen in the response of the bare pixel as well, and the fringe maxima and minima are located at the same frequencies in

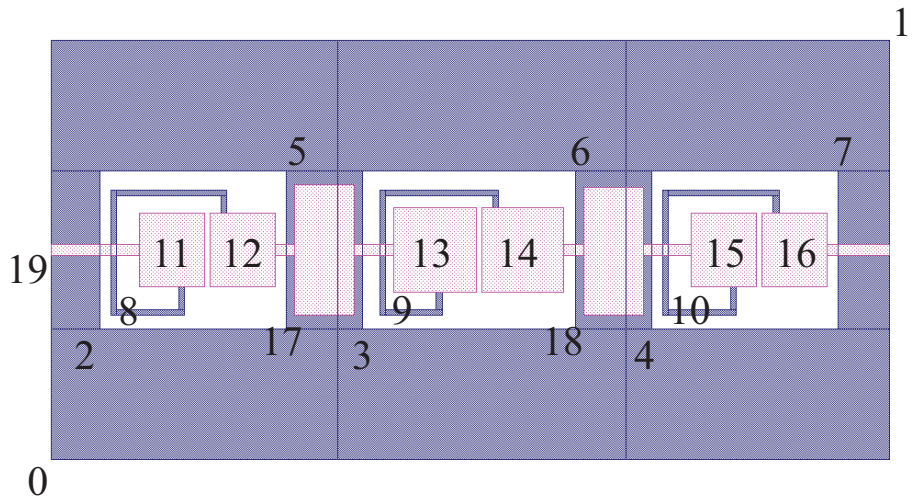

Figure 4.7: SONNET geometry layout schematic for the final filter. Numbers indicate points on the schematic as follows: 0 is the origin, 1 the upper-right corner of the layout. 2, 3, 4 and 5, 6, 7 are the lower-left and upper-right corners, respectively, of the holes in the niobium ground plane. 8, 9, 10 are the lower-left corners of the spiral inductor. 11, 12, 13, 14, 15, 16 are the lower-left corners of series capacitors $C_{Lseries1,2,3}$. 17, 18 are the lower-left corners of the two shunt capacitors. 19 is the lower-left corner of the input microstrip. The microstrip width is 2.5 μm.

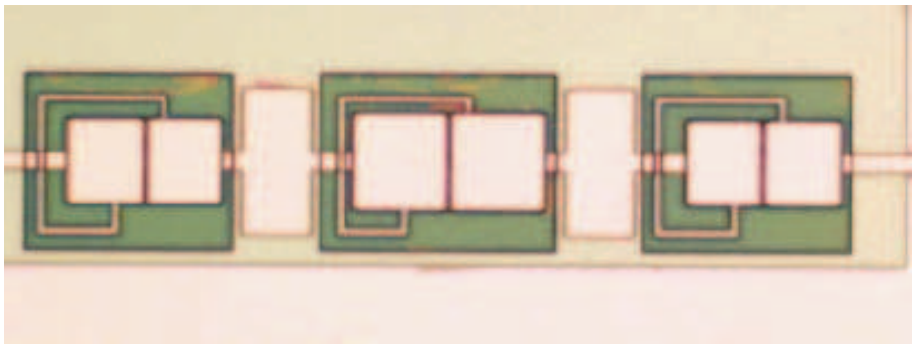

Figure 4.8: Photograph of bandpass filter taken under the microscope. Green is the hole in the niobium ground plane showing the substrate. Niobium ground plane and the wiring layer are seen in pink. The one-to-one correspondence between the photograph and the SONNET layout in Figure 4.7 is evident.

the response of the pixels containing the filters and ones without them. This strongly suggests that the fringes are not due to passband response of the BPFs. Furthermore, the electrical delays implied by the rapid fringing are much too long to be explained by the physical length of the filter. The source of the passband fringing is currently

	BPF 1	BPF 2	BPF 3	BPF 4
1	148,74	145.5,74	145.5,74	145.5,74
2	8.5,23	8.5,23	8.5,23	8.5,23
3	55,23	57,23	57,23	57,23
4	106,23	105.5,23	105.5,23	105.5,23
5	41.5,51	39.5,51	39.5,51	39.5,51
6	92.5,51	88,51	88,51	88,51
7	139,51	136.5,51	136.5,51	136.5,51
8	10.5,25.5	12.5,29.5	12.5,29.5	12.5,30
9	58,25.5	61,29.5	61,29.5	61,30.5
10	108,25.5	109.5,29.5	109.5,29.5	109.5,30
11	15.5,30.5	15,32.5	16,34	19.5,34.5
12	28,30.5	28,32.5	27.5,34	27.5,34.5
13	60.5,29.5	64,32	64,34	67.5,34.5
14	76,29.5	76.5,32	76,34	76,34.5
15	113,30.5	112,32.5	113,34	116.5,34.5
16	125.5,30.5	125,32.5	124.5,34	124.5,34.5
17	43,25.5	43,27	43,28.5	43.5,32.5
18	94,25.5	91.5,27.5	91,29	92,32
19	0,36	0,36	0,36	0,36

Table 4.4: The table gives x,y coordinate locations of points for the SONNET layout in Figure 4.7. All the dimensions are in microns.

under investigation.

Figure 4.11 also shows that the response of the pixel without a bandpass filter is limited by the detector on the low-frequency side. Since band gap for superconducting aluminum is 90 GHz, the kinetic inductance detector is unresponsive to radiation with frequency less than that. On the high-frequency side the FTS response is limited by the two 420 GHz (14 icm) filters in the optical chain. In the absence of these filters

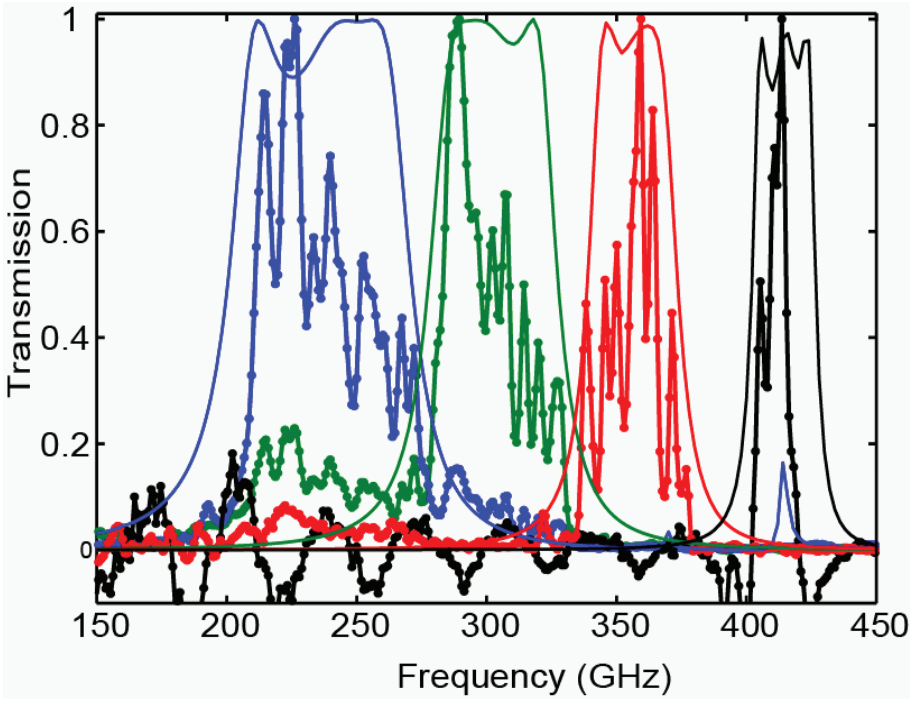

Figure 4.9: Normalised measured and predicted bandpass filter responses. Lines with dots are the actual data measured using a Fourier Transform Spectrometer normalised by the maximum transmission value for that filter. The lines without dots are the normalised response predicted using SONNET simulations.

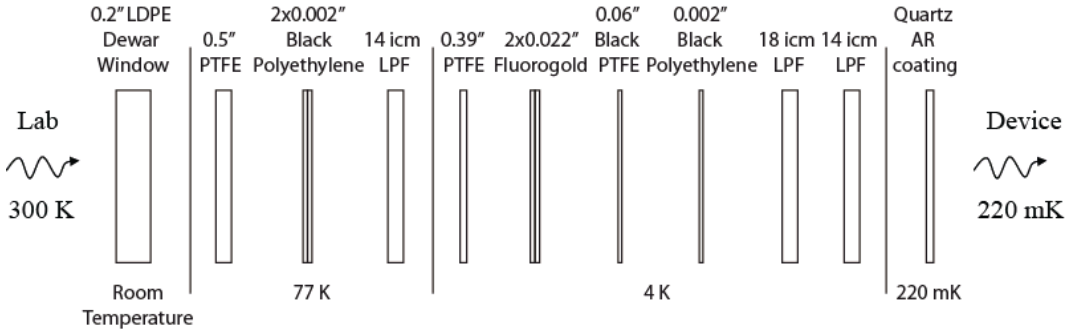

Figure 4.10: The optical chain mounted on the dewar windows with temperatures and thicknesses of various IR blockers and metal-mesh filters.

it would be limited by the high-frequency cutoff frequency of the multi-slot antenna. Beyond the niobium bandgap at 700 GHz for the antenna and microstrip, both would become lossy and would reduce pixel responsivity further.

The simulations predict that the filters should show an increased transmission

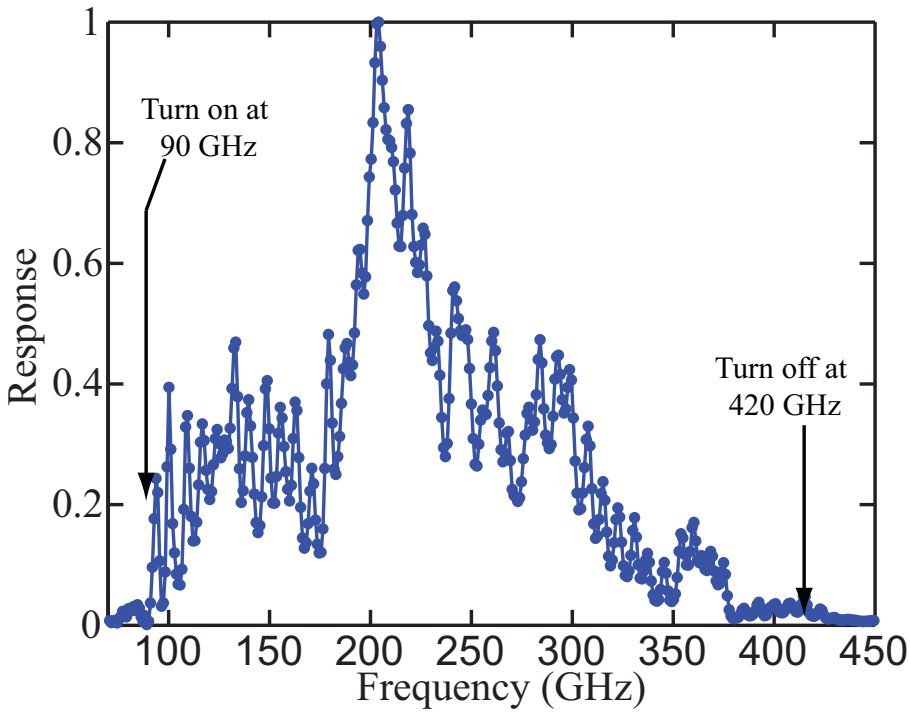

Figure 4.11: Normalised measured response of pixel with no inline bandpass filter between the antenna and the detector. The measurement was performed using an FTS. The response turns on at 90 GHz and turns off again at 420 GHz.

close to their second harmonic, possibly due to self-resonance of the series inductors. However, if this effect is present it is much smaller than is predicted by the simulations and is not clearly visible over the out of band baseline fluctuations in the measured filter responses.

4.4 Multi-Color Pixel Design

One of the primary advantages of fabricating an inline bandpass filter is the ability to make multi-color pixels. This can be done by connecting two (or more) filters of different frequency passbands in parallel to the microstrip coming from a single broadband antenna using very short microstrip line sections (see Section 4.4.2). The output microstrips from each of these filters couples power to different detectors allowing each pixel to see multiple colors, using single broad-band antenna and multiple

BPFs and detectors.

4.4.1 Two–Color Design and Results

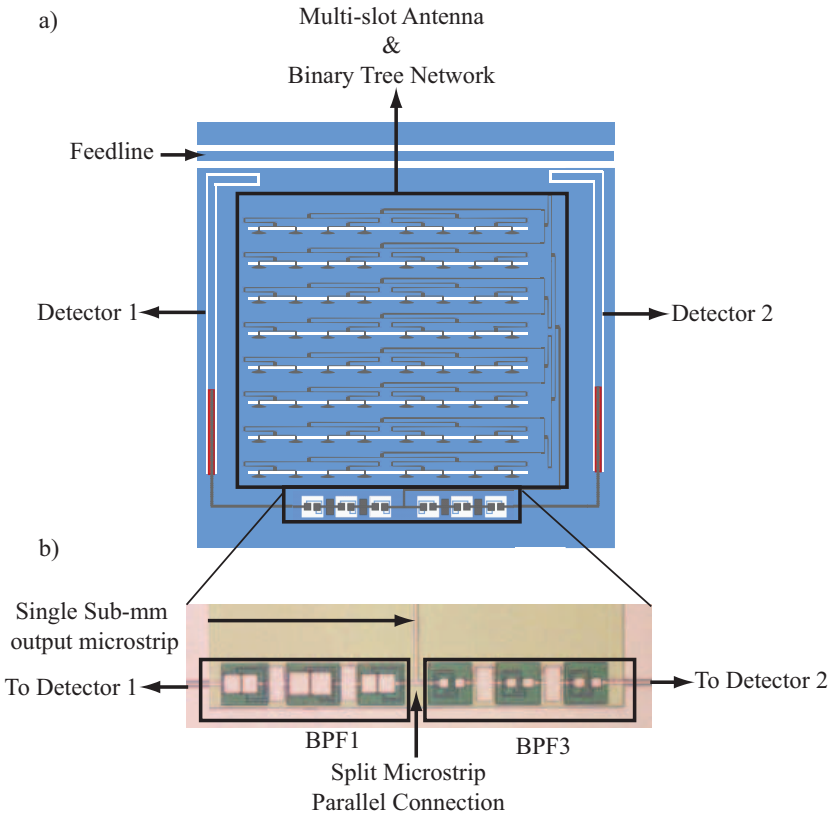

Figure 4.12: a) A schematic of the layout for a two-color pixel showing a single broadband, multi-slot antenna, single microstrip which splits in two and connects to BPF1 and BPF3 in parallel. The outputs of these bandpass filters are connected to different MKIDs made using resonators of different resonance frequency, and readout using a single feedline

Figure 4.12 shows the layout for a two-color pixel. For proper operation of the multi-color pixel it is essential that the filters connected in parallel present each other with high impedance outside their bands and don't load each other. Figure 4.13 shows the plot for input impedance for the bandpass filters vs the frequency. The plot shows that the filter input impedance is roughly the same as the input microstrip inside the filter band, resulting in high transmission, but high impedance out of band, resulting in low transmission due to the mismatch. However, the figure also shows that the

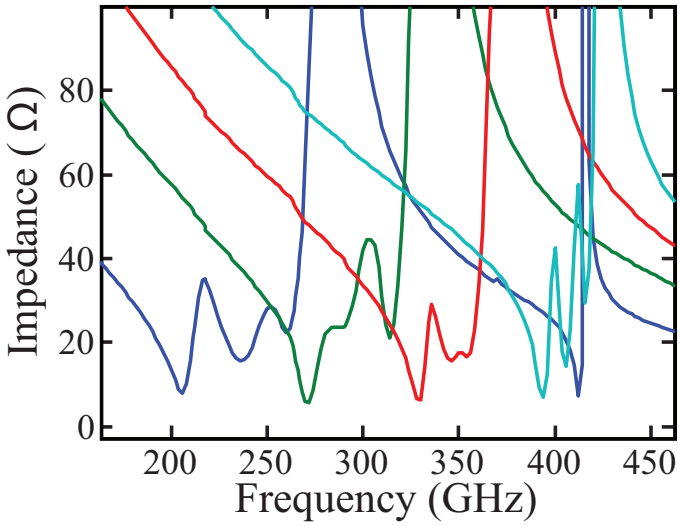

Figure 4.13: Input impedance of the bandpass filters simulated using SONNET

impedance of BPF 1 decreases to low values in the BPF 4 passband. The effects of this on multi-color pixel performance are discussed in Section 4.4.2.

We have tested two different two-color pixels, with passband of the first type of pixel defined by BPFs 1 and 2 and that of the second type of pixel by BPFs 1 and 3. The CSO demonstration camera (Chapters 1 and 5) was made using the second multi-color pixel, with the two colors corresponding to the passbands of BPFs 1 and 3. Results of this two-color pixel response function are plotted in Figure 4.14. It shows that the response of the two bandpass filters connected in parallel is close to the predicted response of single filters seen in Figure 4.9. The overplotted atmospheric transmission spectrum shows that the filter passbands lie well within the transmission windows and away from the water lines.

4.4.2 Four–Color Design

The four-color pixel is an extension of the two-color pixel design and can be constructed by connecting four detectors to a broadband antenna in parallel through four different bandpass filters (Figure 4.15a).

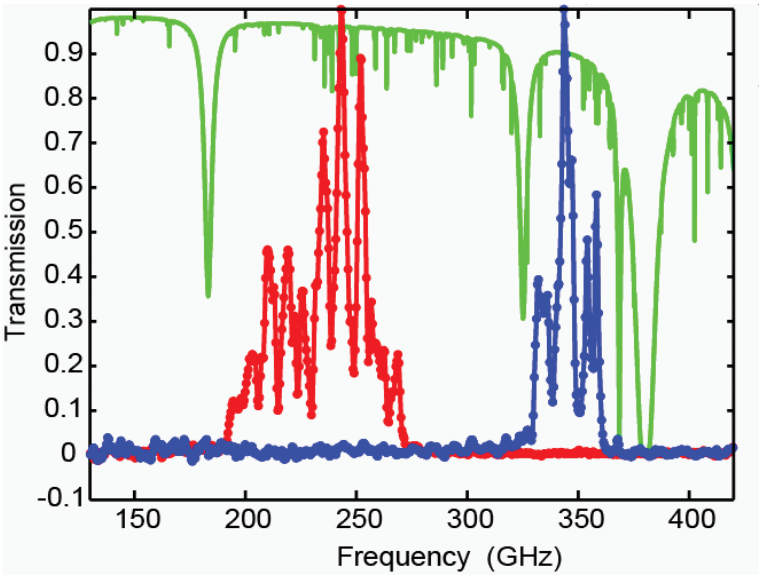

Figure 4.14: FTS response of the two-color pixel. Red and blue lines represent response of detector connected to BPF1 (209-265 GHz) and BPF3 (335-361 GHz), respectively. Green line shows the atmospheric transmission as a function of frequency for 0.5 mm precipitable water vapor plotted using AT (http://www.submillimeter.caltech.edu/cso/weather/atplot.shtml).

The equivalent microwave circuit for the schematic is shown in Figure 4.15b. Although the filters were designed to have high input impedance out of band, sections of transmission lines can act as impedance transformers. If the length of the microstrips connecting inputs of the filter is a signficant fraction of $\lambda/4$ it can transform the effective input impedance of the filter as seen by the other filters to a short. At the frequency at which this happens, the filter with low input impedance will load the other filters, resulting in the distortion of their passband. Hence, it is essential that the transmission line length be much less than $\lambda/4$, where λ is the wavelength at the higher cut off frequency of BPF4. Mathematically, this may be seen as follows: The input impedance of j^{th} BPF when transformed by a transmission line of characteristic imepdance Z_0 and length L is given by:

$$Z_j = Z_0 \frac{Z_{inj} + jZ_0 \tan(\beta L)}{Z_0 + jZ_{inj} \tan(\beta L)} \tag{4.10}$$

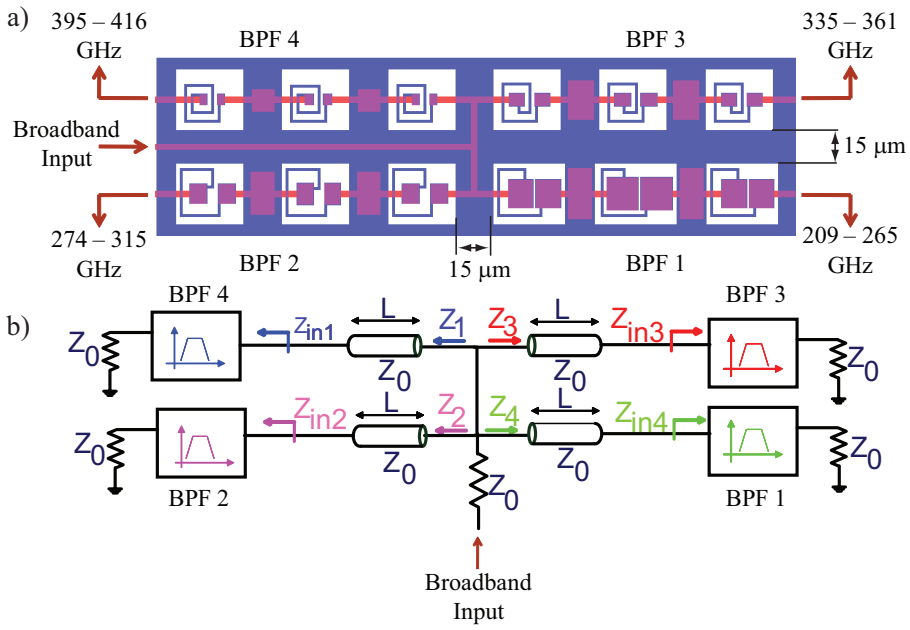

Figure 4.15: a) Layout schematic for networked bandpass filters in a four-color pixel. The broadband input comes from a wideband, multi-slot antenna. The input microstrip splits into 4 microstrips, which connect the bandpass filters in parallel. Output of each of the filters goes to a separate detector. b) A block diagram for the layout in a). The input microstrip bringing power from the antenna is idealized and represented by impedance Z_0 ($\simeq$ 20 Ω). It splits into 4 transmission line sections each, with characteristic impedance Z_0 in their respecitve bands and length l. These are connected to BPF inputs. The output of the BPF is connected to the detector, which itself is represented by a load of matched impedance Z_0 to ground.

where β is the propagation constant of the wave at a wavelength where $L = \lambda/4$, $\beta = \pi/2L$, and $Z_j = Z_0^2/Z_{inj}$. Hence, we see that for large Z_{inj} we get small Z_j, which can load other filters when connected using long transmission lines. In order to ensure short sections of connecting transmission lines, the ground plane of the filters adjacent to one another need to overlap such that the common ground plane is only $\sim$ 15 μm wide, as shown in Figure 4.15a. We expect that decreasing the ground plane overlap between the filters any further would cause increased mutual inductance between inductors in adjacent filters and result in degradation of filter response. No such effects were observed in simulations with the current dimensions.

Simulations were peformed using the layout shown in Figure 4.15a. The results

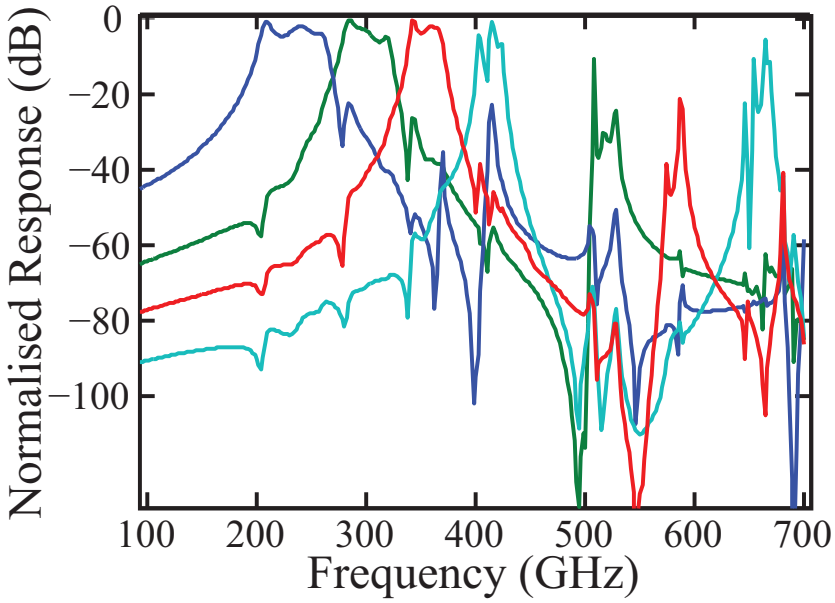

Figure 4.16: SONNET simulation for response of four bandpass filters connected in parallel using the feednetwork as shown in Figure 4.15a

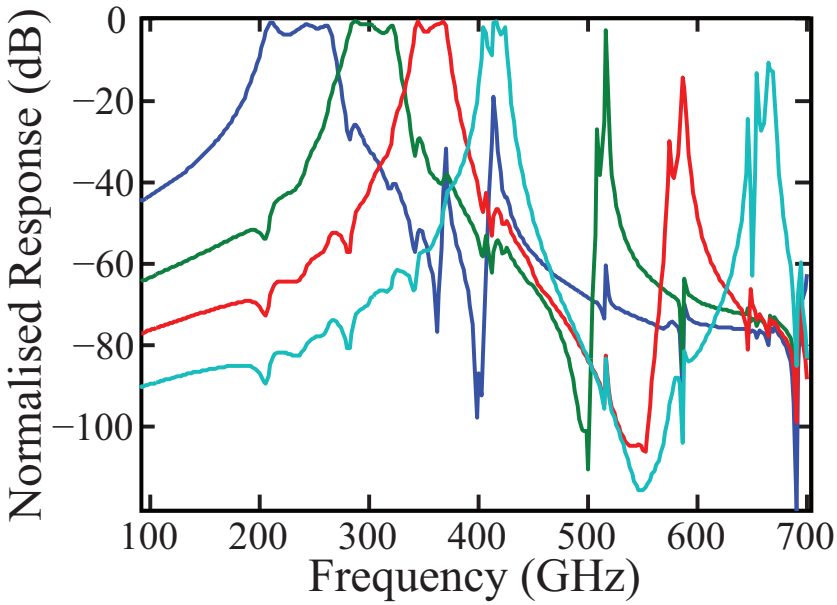

Figure 4.17: SONNET simulation for response of four bandpass filters connected in parallel directly to a common input port without a feednetwork inbetween

for the filter transmission for each of the four filters is shown in Figure 4.16. We find that that filter performance matches the stand-alone filter performance well for passbands 1, 2, and 3, and any out-of-band features remain well below -20 dB for all the four passbands. However, the BPF 4 response shows a notch in its passband as a result of connecting all the four filters in parallel. This is a result of band 1 input impedance reducing to $\simeq 20\ \Omega$ in the passband of filter 4 and loading it (Figure 4.13). To finally use this design in a 4-color pixel, the design for BPF 1 will have to be tweaked to prevent this. The dimensions used to make the feednetwork are shown in Figure 4.15. The resultant filter response is shown in Figure 4.16. This can be compared with the best that can be theoretically done with current design for BPF 1. For this, inputs of all the 4 BPF are connected directly to a common input port in SONNET without a feednetwork between them. The results for the filter response in this case are shown in Figure 4.17. The notch deepens from -9 to -16 dB due to the impedance transformation done by the feednetwork.

4.5 Conclusions

We have designed and tested on-chip, lumped-element bandpass filters with passbands corresponding to the atmospheric windows from 209-274 GHz, 265-315 GHz, 335-361 GHz, and 397-416 GHz. The performance of the filters is well predicted by computer simulations done using SONNET, implying that the fabrication process matches the estimated value for the thickness of SiO_2 dielectric (t = 400 nm) and its dielectric constant value ($\varepsilon_d = 4$) well. Further, we have fabricated pixels with a single antenna coupled to multiple bandpass filters and detectors and demonstrated their two-color operation.

Our measurements show no effects due to interaction between the bandpass filters connected to the same input microstrip other than due to loading from each other's input impedance. Furthermore, when networked to form a four-color pixel,

simulations do not show a change in response due to coupling between inductors of adjacent filters. Hence, it should be possible to integrate all the filters into a single pixel by simply scaling the filter network and using four detectors connected to each of the filters thereby operating a multi-color pixel with 4 colors, after tweaking BPF 1 response to prevent it from loading BPF 4.

CHAPTER V

A 16–PIXEL, TWO–COLOR, SUBMILLIMETER DEMONSTRATION CAMERA

5.1 Introduction

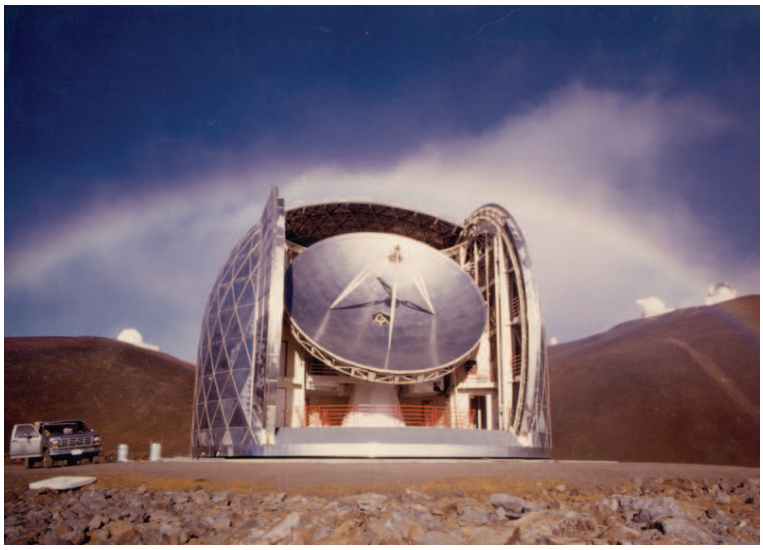

Figure 5.1: Photograph of Caltech submillimeter obervatory on Mauna Kea, Hawaii (http://www.submillimeter.caltech.edu/cso/)

This chapter elaborates the design and implementation of the 16-pixel, two-color DemoCam, which was used to show the submillimeter pixels developed using the novel technologies discussed in Chapter 3 and 4 their first light on a telescope (CSO). As mentioned in Chapter 1, the future generation of this camera – MKIDCam – will have 576 pixels, each with four-color imaging capability, and will be a superior-performance replacement for Bolocam as a CSO facility instrument. Further into the future this technology may be used to build cameras with still larger numbers of pixels and 4- or 5-color imaging capabilities for CCAT since designs for larger number of pixels and

colors are easily scalable from our current design.

5.2 Camera Design and Layout

Pixel	Detector A (Band 209-265 GHz)			Detector B (Band 335-361 GHz)		
	f_r (GHz)	L_c (µm)	L_t (µm)	f_r (GHz)	L_c (µm)	L_t (µm)
1	6.5	244.55	4560.98	6.54	243.05	4533.08
2	6.58	241.57	4505.52	6.59	241.21	4498.69
3	6.51	244.17	4553.97	6.55	242.68	4526.16
4	6.6	240.84	4491.87	6.61	240.48	4485.08
5	6.66	238.67	4451.4	6.67	238.31	4444.73
6	6.74	235.84	4398.57	6.78	234.45	4372.62
7	6.68	237.96	4438.08	6.69	237.6	4431.44
8	6.75	235.49	4392.05	6.79	234.10	4366.18
9	6.52	243.8	4546.99	6.56	242.31	4519.26
10	6.62	240.11	4478.3	6.63	239.75	4471.55
11	6.53	243.42	4540.02	6.57	241.94	4512.38
12	6.64	239.39	4464.81	6.65	239.03	4458.10
13	6.7	237.25	4424.83	6.71	236.89	4418.23
14	6.76	235.14	4385.56	6.8	233.76	4359.76
15	6.72	236.54	4411.66	6.73	236.19	4405.10
16	6.77	234.79	4379.08	6.81	233.41	4353.36

Table 5.1: Table of detector design parameters. The resonant frequency defines the resonator length, and the resonator quality factor determines the coupler length. The length of the submillimeter overlap between microstrip and CPW is uniformly 1 mm (Chapter 3). Bands for detectors A and B in each pixel refer to the BPFs used between the detector and antenna.

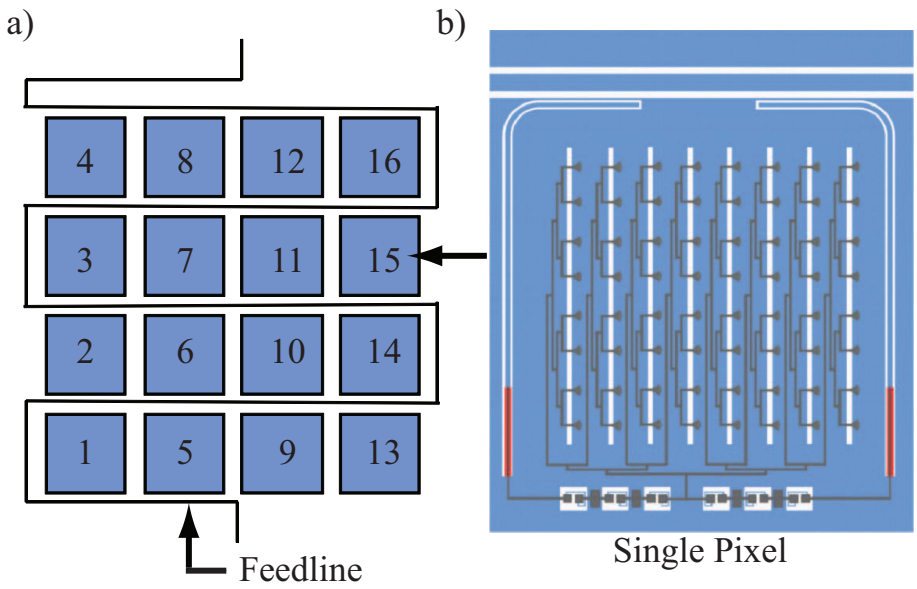

Figure 5.2: a) Layout of the 16-pixel, two-color camera chip, with pixels tiled in a 4×4 format with a shared feedline to readout all the pixels. b) Layout schematic of a single, two-color pixel. Schematic shows 8 slot and 8 taps on each slot for clarity. The design uses 16 slots and taps, as discussed in Chapter 3.

Two-color pixels with passbands in frequency ranges 209-265 GHz and 335-361 GHz were used to fabricate the array. The design dimensions for the antenna and microstrips are tabulated in Chapter 3 and for bandpass filters are tabulated in Chapter 4.

The photon detectors were implemented using MKIDs resonators. The specifications for the resonators are tabulated in Table 5.1. The resonators were designed to have resonance frequencies between 6.5-6.81 GHz with a gap of 10 MHz between any 2 consecutive resonators. The quality factor under 300 K load was empirically estimated to be close to 15,000, and coupling quality factor was designed to be the same value to maximise detector response (Chapter 3).

Once the pixels were designed with the two-color architecture (Chapter 4) using resonator dimensions tabulated in Table 5.1, they were laid out on the chip in a 4×4 array with a common feedline snaking through the array (Figure 5.2). The feedline carries a frequency comb with a tone at the resonance frequency of each of the

detectors for readout. This arrangement greatly simplifies the cryogenic electronics needed and allows for frequency division multiplexing schemes to readout all the detectors simultaneously using a single microwave co-ax, enabling the large arrays needed for future astronomical missions.

12 (6.61) --- 11 (6.6)	30 (6.79) --- 26 (6.75)	16 (6.65) --- 15 (6.64)	32 (6.81) --- 28 (6.77)
6 (6.55) --- 2 (6.51)	20 (6.69) --- 19 (6.68)	8 (6.57) --- 4 (6.53)	24 (6.73) --- 23 (6.72)
10 (6.59) --- 9 (6.58)	29 (6.78) --- 25 (6.74)	14 (6.63) --- 13 (6.62)	31 (6.8) --- 27 (6.76)
5 (6.54) --- 1 (6.5)	18 (6.67) --- 17 (6.66)	7 (6.56) --- 3 (6.52)	22 (6.71) --- 21 (6.7)

Figure 5.3: Layout of the resonators in different pixels according to frequency. Bracketed numbers are the resonator frequency, the non-bracketed numbers are the resonator order in frequency space. Different pixels are separated by solid lines, and dotted lines separate two detectors on the same pixel.

Figure 5.3 shows the layout of the resonators on the chip. Due to readout electronics constraint that only resonators within 50 MHz of one another can be readout simultaneously (see Section 5.3.1), 16 of the 32 resonators are laid out so that the pairs of adjacent frequency resonators are on the same pixel. This enables us to simultaneously readout both the detectors on the same pixel, which allows observation of submillimeter sources in both the frequency bands simultaneously as well. These detectors are on pixels 2, 4, 5, 7, 10, 12, 13, and 15. The remaining detectors are placed on the chip such that the pairs of adjacent frequency resonators corresponding to the same submillimeter frequency band lie far apart on the chip, allowing us to look at the source with one detector and the sky with another and use sky noise subtraction to get a better signal-to-noise ratio.

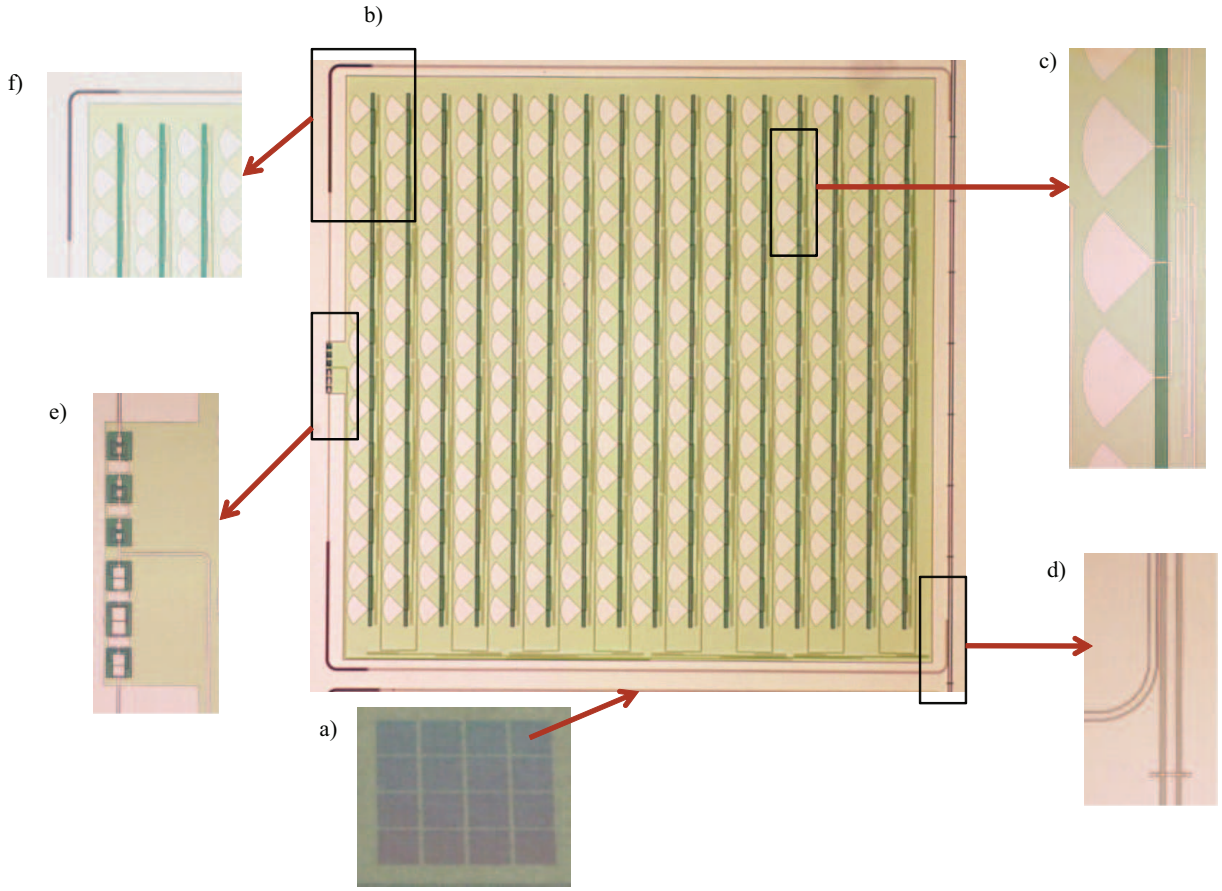

Figure 5.4: Picture of 16-pixel camera and different sub-components after zooming in. a) 16-pixel, two-color camera. b) Single camera pixel. c) Antenna Slots, taps, and feednetwork. d) Resonator coupler. e) Two submillimeter BPFs connected in parallel. f) Submillimeter microstrip and CPW overlap

Figure 5.4 shows a picture of the DemoCam chip. The figure also shows zoomed-in pictures of different components of the chip for clarity. Figure 5.5 shows picture of a single wafer with at least 12 usable 16-pixel cameras.

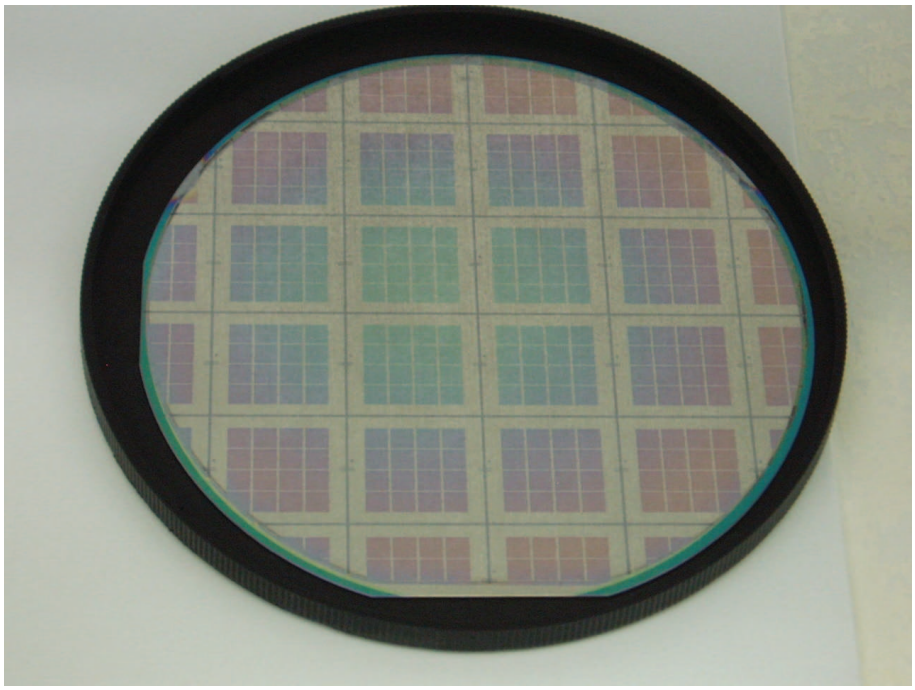

Figure 5.5: Picture of the wafer on which the camera was fabricated

5.3 Setup

5.3.1 Electronics

The electronics are implemented using a digital equivalent of the analog readout discussed in Chapter 2. The analog readout requires multiple copies of discrete and expensive microwave circuitry such as the frequency synthesizers – one for each resonator. The digital circuit discussed below integrates generation of frequency comb used to readout the resonators simultaneously and detection of different tones out onto a single board. Figure 5.6 shows the block diagram for the readout electronics. It is implemented using a software-defined radio [31]. In this method the required number of tones, each corresponding to a detector, are generated – separated by the

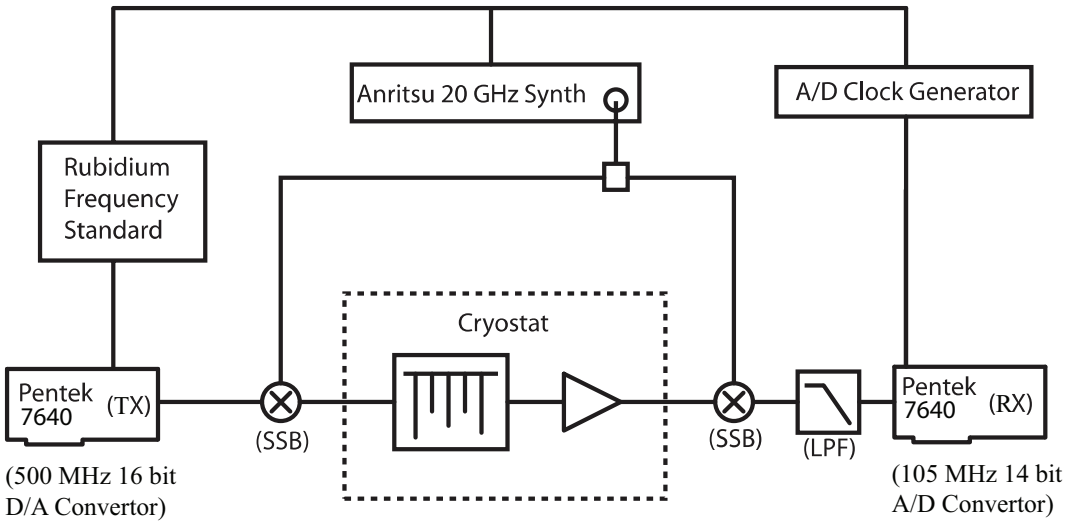

Figure 5.6: Schematic of the room-temperature electronics used to readout the camera

difference of the detector resonance frequencies. This is done using a 16-bit, 500 MHz digital to analog (D/A) convertor which resides inside a Pentek 7640 board. The entire frequency comb is then upconverted using a single side-band (SSB) mixer with the carrier generated by a Anritsu frequency sythesizer which can generate signal up to 20 GHz. The frequency synthesizer is stabilised using a rubidium frequency standard.

The frequency comb is then passed through the detectors and mixed back to baseband with another SSB mixer and signal from the frequency synthesizer. The baseband signal is anti-alias filtered and digitized using as 14-bit, 105 MHz analog to digital (A/D) converter which also resides on the Pentek 7640 board. The resulting tones are then individually mixed down to 0 Hz and the complex detector output is stored in a computer. This readout system currently allows us to read an arbitrary number of resonators with resonance frequencies within a 105 MHz band.

For this telescope run the detector phase response was measured because the resonator responsivity is higher in phase direction. However, the phase noise of the resonator is much higher than the amplitude noise as well (Chapter 2). Ideally, the

entire complex signal needs to be readout and the final measurement made along the direction with maximum signal-to-noise ratio [44]. However, this can be easily implemented using the same readout electronics by simply changing the software.

5.3.2 Optics

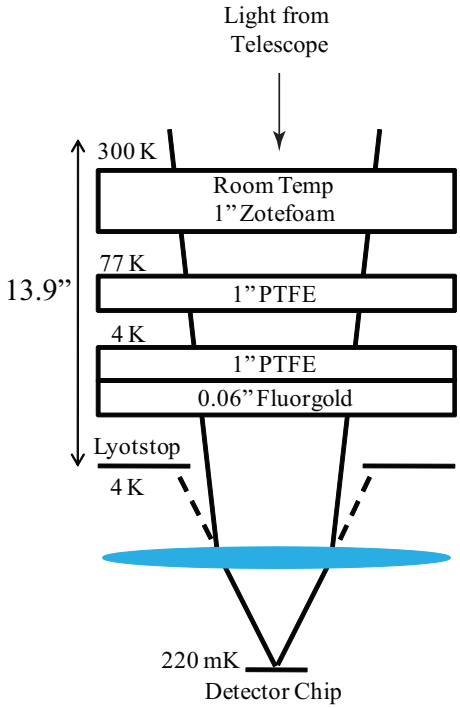

Figure 5.7: Optical chain used for filtering IR light to reduce the thermal load on the cold stage

Bolocam optics box [83] was used to couple light from the telescope to the dewar. Different temperature stages of the fridge were physically separated using the dewar windows (Figure 5.7). The fridge optical chain (Figure 5.7) consisted of a 1"-thick Zotefoam window at room temperature, 1"-thick PTFE window at 77 K, 1"' thick PTFE window at 4 K, followed by 0.060"-thick flurogold sheet. Subsequently, a PTFE lens (Chapter 3) is used to ensure the antenna beam can pass through the dewar windows. PTFE and fluorogold act as good IR blockers to reduce heat load on the fridge cold stage and allow cycling to base temperature. All PTFE components

and lens are AR coated using Zitex. No metal-mesh filters were used and filtering at submillimeter frequencies was completely implemented using on-chip filters discussed in Chapter 4. This allowed for multi-color pixel operation (Chapter 4).

5.3.3 Cryogenics

5.3.3.1 Cryostat

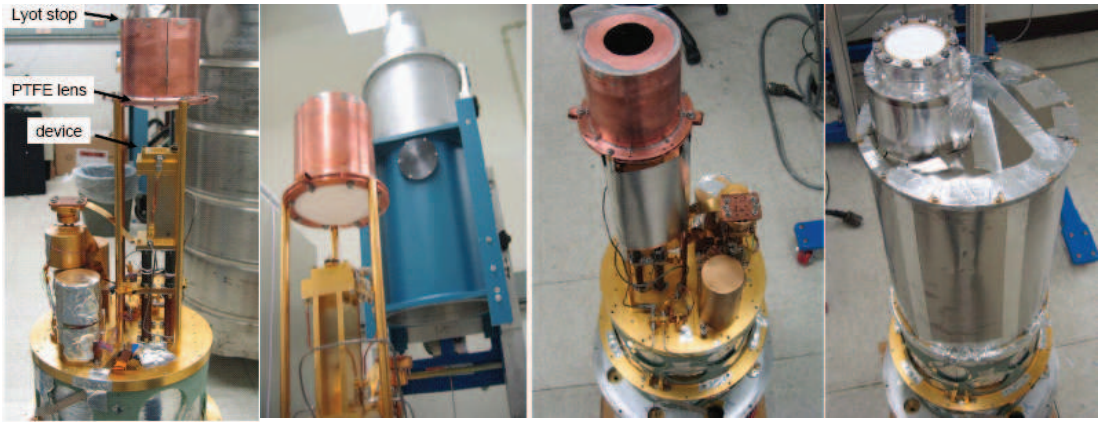

Figure 5.8: Photographs of the cryostat

Figure 5.8 shows photographs of the fridge used to cool down the DemoCam in the lab and at CSO (Figure 5.1). It is a closed-cycle, two-stage He-3/He-4 system similar to the one used to cool down Bolocam. The fridge has a base temperature of 220 mK with the windows open and the optical chain shown in Figure 5.7. The fridge has much lower cooling power compared to a dilution fridge and the material and geometry for readout microwave co-axes has to be carefully chosen and heat sunk in order to ensure it cools down to the base temperature. We used 0.085" co-ax made out of stainless steel from room temperature to 4 K. From 4 K to 220 mK stage 0.085" NbTi alloy coaxes were chosen for their better thermal properties close to 220 mK, compared to Nb. The cables were carefully heat sunk at 77 K, 4 K, and the intermediate stage. Heat sinking for the center conductor of the co-axes was ensured by connecting the co-axes bringing the signal into the stage and co-ax

taking signal out of the stage through a small valued attenuator (1-3 dB). This allows for a thermally conductive path from center conductor to the co-ax shield. These attenuators were held in custom designed heat sinks made out of gold-plated oxygen free high conductivity (OFHC) copper.

The device was magnetically shielded using Metglas 2705M tape at 4 K and 77 K. In spite of this, the device was seen to respond to the Earth's magnetic field. Future telescope runs will correct this by using niobium shielding can at 4 K (See 6.2.2.4).

5.3.3.2 Device Box

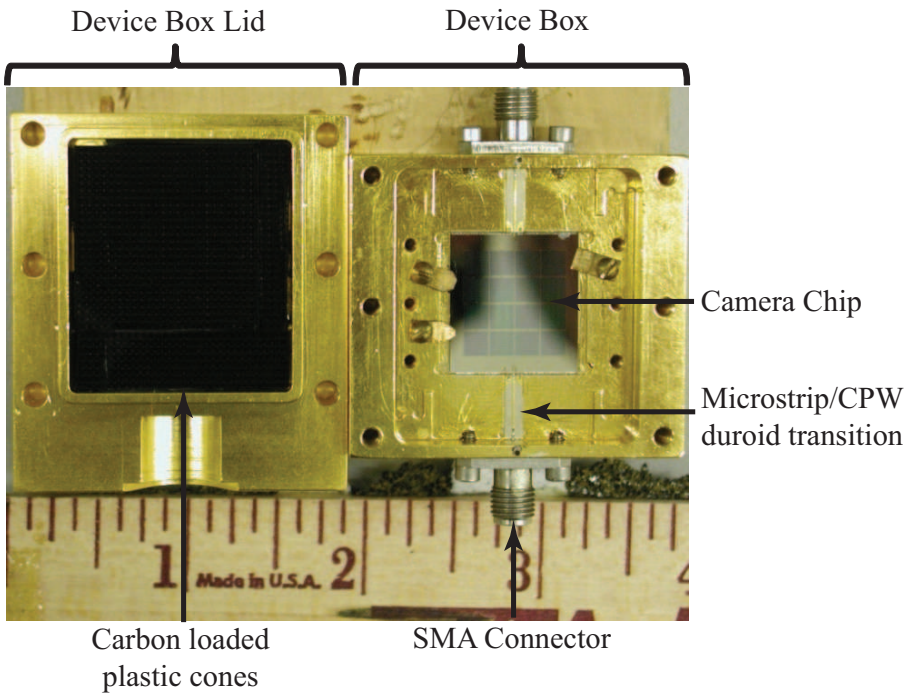

Figure 5.9: Photograph of the housing used to mount the camera chip in the cryostat

The device was mounted on the fridge ultra-cold stage housed in a gold-plated box (Figure 5.9) made out of OFHC copper. Gold plating ensured good thermal contact between the cold stage and the device box. Microwave readout circuit consisted of an SMA connector, followed by duroid microstrip-to-CPW transition [84], the feedline on the camera chip and then a duroid transition and an SMA connector again. The

different portions of microwave circuit were carefully designed to ensure that there was a 50 Ω impedance match all along, to prevent standing waves or losses due to reflections. This was further ensured by using a 1 mm wide ribbonised wirebond to minimise reflections due to the wirebond inductance. The depth of the channel for the duroid microstrip and the democam chip is carefully chosen such that the top surfaces are flush with each other to minimise the length of wirebond required for the connection.

The features on the chip are on the top surface (visible), and the device was illuminated using submillimeter radiation from the substrate side (Chapter 3) from a hole in the box below the device (not visible). Carbon loaded plastic cones were glued on to the box lid since they are good submillimeter loads and prevent excitation of box resonant modes at those frequencies. The box design is versatile and may be adapted to the study of other microwave frequency devices.

5.4 Results

The 16-pixel, two-color camera, along with the associated instrumentation discussed in this chapter was used to take maps of Jupiter, Saturn, and G34.4 using two pixels and in the two frequency bands corresponding to BPFs 1 and 3.

Figures 5.10a, and b show maps of Jupiter obtained by raster scanning over the source. This was accomplished soon (couple of hours) after beginning the on-sky observation for the first time. Jupiter is a bright source and was detected with high significance in both the bands. The sensitivity for this mode of operation are 1 $Jy/\sqrt{Hz}$ and 10 $Jy/\sqrt{Hz}$ for band 1 and 3, respectively [14].

The figure also shows the images of G34.3 – a galactic HII region. These were obtained by drift scanning over the source and as such we expected to see more 1/f atmospheric noise. The sensitivities in this mode of operation are 1.6 $Jy/\sqrt{Hz}$ and 14 $Jy/\sqrt{Hz}$ for band 1 and 3, respectively [14].

The sensitivities quoted in both cases are effective sensitivities limited by the efficiency of the optical chain rather than the efficiency of the detector itself (See Chapter 6).

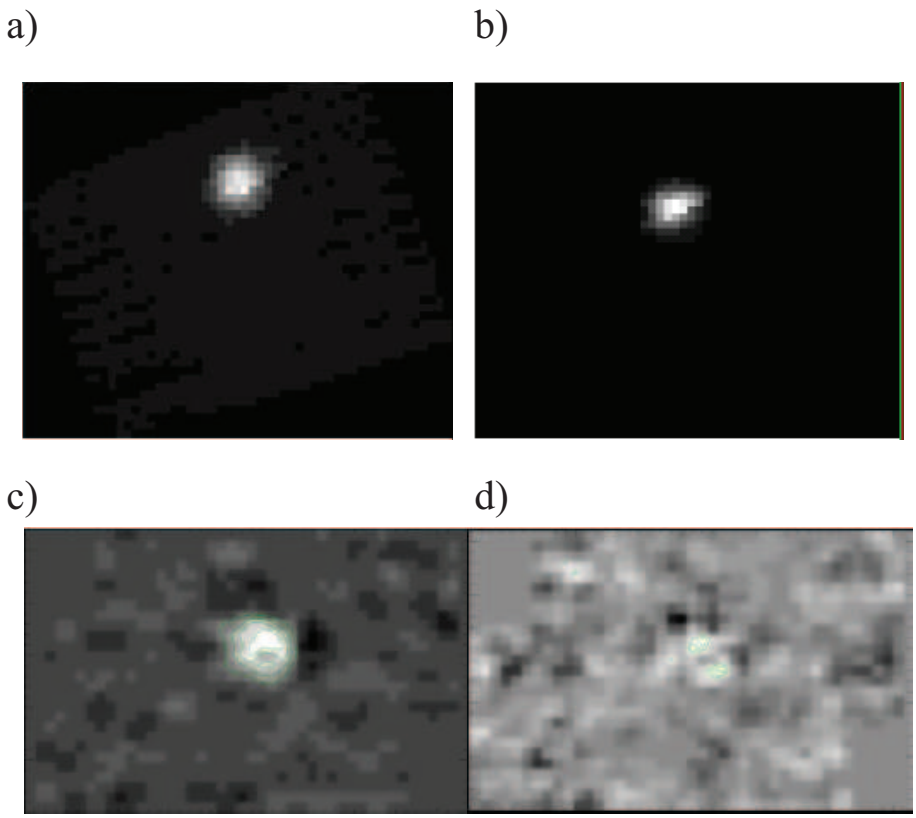

Figure 5.10: Images of Jupiter and G34.3 taken using the DemoCam [14]. a) Jupiter in Band 1. b) Jupiter in Band 3. c) G34.3 in Band 1. d) G34.3 in Band 3

5.5 Conclusion

In conclusion we have used the planar technology for making submillimeter wave antenna, microstrips, and bandpass filters to implement a multi-color submillimeter pixel. We have integrated the pixels on a single chip to make a 16-pixel, two-color camera – which along with the cryogenic, readout, and optical intrumentation – was mounted on top of CSO and used to take astronomical data. With this we have shown that the Microwave Kinetic Inductance Detectors are a viable technology for making

a full-fledged facility instrument in the submillimeter frequency range. Future steps involve realisation of a 24×24 pixel, four-color camera which can be used as a facility instrument on CSO and used to replace Bolocam.

CHAPTER VI

FUTURE SCOPE

6.1 Resonator Noise

6.1.1 Conclusions

We have studied the temperature and the power dependence of resonance frequency shift and frequency noise of superconducting resonators which are used to make the sensing element of our photon detectors. Our experiments indicate that the resonance frequency response of the resonator matches two-level system theory well, thereby indicating that these could be responsible for the resonator frequency noise as well. Due to the high readout power used for these measurements, the TLS dissipation was strongly saturated and the quality factor data cannot be explained using the TLS theory. The power law dependence of the resonator frequency noise, which is the dominant noise in our resonators, with the resonator readout power is $P^{-0.46}$ and matches the index of -0.5 in the literature [44]. The frequency noise was seen to decrease by close to two orders of magnitude as temperature was increased by an order of magnitude from 120 – 1200 mK, with the power law dependence well approximated as $T^{-1.73}$. This is a new and very interesting result with important implications for resonator design. The temperature dependence of this noise has important practical implications. For instance, if the two level system origin of the noise is correct, designing resonators to operate in the regime $f_r << 2kT/h$ could result in lower noise and improved performance.

6.1.2 Future Work

Future experiments could concentrate on repeating the measurements in a low-power regime to be able to reconcile the quality factor data as well. Gathering the data at lower temperatures, different resonance frequencies, and multiple harmonics of the same resonators would also provide deeper insights into behavior of two level systems and how to further optimize the resonator performance. From a scientific standpoint it is critical to not only understand that the two-level systems are causing the noise but also to understand the mechanism for noise generation. This would involve devising a theory that explains the noise spectrum along with the temperature and power dependence. It might also be necessary to evaluate the time scales for the mechanism and whether the generation mechanism is related to T_1 (dissipative processes) or T_2 (dephasing processes). Experimental data helping to corroborate or falsify such a theory would indicate new avenues to optimize the resonator performance parameters and the trade-offs involved in making good resonators for different applications from qubit readouts to photon detectors.

6.2 Camera Design

6.2.1 Conclusion

We have designed and tested a 16-pixel, two-color submillimeter wave, prototype camera. Each of the pixel components of the camera are implemented using novel planar technologies which allow for a monolithic architecture. The antenna is implemented using multi-slot architecture [62] allowing for large effective area and narrow beams. This obviates the need for interceding on-chip optics and enables scalability and integration. The multi-slot antenna uses a binary tree feed network [65] used to combine power from each of the slots and taps into a single output microstrip. On-chip superconducting, lumped-element, bandpass filters were designed and implemented and placed inline between the antenna output and the detector to prevent loading of the

detector due to atmospheric emissions. These remove the need to use complicated and bulky metal mesh filters reducing the heat load. These also make it possible to design multi-color pixels where a single broadband antenna is connected to multiple bandpass filters in parallel, output of each of which is detected by a separate photon detector. We have demonstrated the two-color operation of a 16-pixel camera and designed a four-color pixel. The photon detectors were implemented using Kinetic Inductance Detector technology [28] which uses superconducting microresonators as the sensing element. This is a powerful new approach to make very large arrays. The readout for the entire array can be easily accomplished by frequency division multiplexing the readout signal on just two microwave coaxes.

Our submillimeter pixel design conclusively addresses the problem of scalability to large arrays and four colors. Both these goals are scientifically significant. Sections below suggest some technical issues that need to be overcome while desigining the next generation instrument with four colors and 36 pixels before the final MKIDCam with four colors and 576 pixels can be implemented.

6.2.2 Future Directions

6.2.2.1 Coupling Quality Factor Design

To maximise the detector sensitivity the coupling quality factor, which may be adjusted by changing the coupler length (Section 3.5.2.2), needs to be equal to the internal quality factor of the resonator (Section 3.5.1). The internal quality factor can in principle be limited by various effects and for our designs it is limited by the resonator optical loading (Table 3.4). For the design of the DemoCam an optical loading due to 300 K was assumed for purposes of lab testing the camera. The resulting empirical value of Q_i was 15,000 and the coupler length was adjusted to give the same value for Q_c. However, the optical loading at the telescope through the optical chain is lower, resulting in a higher Q_i. Implementation of a sensitive next generation camera needs to account for lower optical loading at the telescope and proportionally

design for a higher coupling quality factor. Such a critically coupled resonator will respond optimally to astronomical sources [72].

6.2.2.2 Material and Geometry Exploration

The ultimate sensitivity of a device with ideal design Q_c is limited by its noise. In addition to the noise studies mentioned above the device design may be further improved by exploring different metals, substrates, dielectrics alongwith fabrication techniques such as passivisation of the superconductor using different metals. Different device geometries may also be explored such as microstrip based MKIDs or separation of the absorber and detector (resonator) section of the device to control more of device design parameters separately. The readout power handling abilities are limited by choice of metal and geometry as well. Experiments have shown lower fractional frequency noise at higher readout powers which gives incentives to explore this part of the design phase space as well. Both these directions materials and gemoetries can effect the ultimate noise equivalent power of the detector and will have consequences for further optimising device design [27].

6.2.2.3 Optical Chain

The optical chain used for the DemoCam instrument was low efficiency resulting in a higher detector noise. The background limited sensitivity is 50 mJy/$\sqrt{\text{Hz}}$ in 240 GHz band window but our achieved sensitivity is approximately 20 times worse. This is a result of contribution from multiple factors including - magnetic field sensitivity, sky noise (i.e. atmospheric emissivity fluctuations), and lower than expected detector frequency responsivity, all of which are currently under further investigation.

Recent lab tests have shown that the detectors themselves are working properly but one reason for the low responsivity can be attributed to thicker than desired aluminum film in sensing layer. Additionally, there is excess in-band optical loading reasons for which are being currently investigated. Latest lab experiments with

cryogenic black body show definitively that the optical efficiency of just the detector is actually quite high, 50% or better. Newer resonator designs which are much less susceptible to stray magnetic fields are also being tested.

For future engineering runs at the telescope, optimization of the optical chain performance is a very important area of performance improvement and will itself result in significant instrument sensitivity improvement. This will require a new filter stack with better dielectric constant matching, fewer layers and better AR coating to reduce reflections and increase in band transmission. A 420 GHz metal mesh filter will be incorporated in the filter chain to further reduce the leakage, obviating the need for some of the dielectric layers and resulting in fewer standing waves [14]. This will also require that the design of BPF 1 be tweaked so that its impedance does not reduce to transmission line characteristic impedance (20 Ω) in BPF 4 pass band. This effect causes BPF1 to load BPF 4 resulting in a strong notch in its passband and will add to lower optical efficiencies.

6.2.2.4 Magnetics

Design of better magnetic shielding for the instrument is critical to ensure a superior detector performance. With present system the detectors are sensitive to small changes in the earth's magnetic field. While raster scanning Jupiter, we noticed linear drifts in the detector response compared to large signal from Jupiter. Resultantly, with the present set up, mapping was done either using raster scans to alleviate sky 1/f noise or drift scans which elminates magnetic field effects by leaving the cryostat stationary for the scan duration. Better magnetic shielding would render the detectors insensitive to Earth's field allowing raster scans to reduce the sky noise. This can be achieved by using a niobium can or cryoperm at low temperatures and permalloy shielding at room temperature for the magnetic shielding [14]. Further, we can fabricate ground planes and resonators with holes in the superconducting films.

This will pin the magnetic flux lines that would otherwise be trapped in the MKID resonators and will lead to change in responsivity as they move [14].

6.2.2.5 Readout Electronics

The advent of very fast analog to digital (A/D) and digital to analog (D/A) convertors has made it possible to use software defined radio (SDR) technology for fabricating high performance and low cost boards that read out large pixel count cameras. The specific readout scheme used for our 16-pixel, two-color camera is outlined in Section 5.3.1. The scheme works by digitally generating tones separated in the frequency space by the difference in the resonance frequencies of the resonators. These tones are converted to an analog signal using the D/A convertor and then block upconverted to the readout frequencies of the different photon detectors using a frequency synthesizer stabilised using a rubidium frequency standard. This frequency comb is passed through the detectors and downconverted to the baseband. A fast A/D convertor is used to digitize the output and the signals from different readout channels are separated using a channelisation algorithm implemented using field programmable gate arrays (FPGAs).

This technology is an excellent candidate for building the readouts for future generations of camera. It is an economic solution which is also high performance - often exceeding the performance of the analog readout component which requires bulky expensive signal generators and other analog circuitry to readout each detector. Pentek 7640 board (Section 5.3.1) already incorporates the functionality to generate and detect the frequency comb to readout multiple resonators, on a single board. Future developments in the technology which would be relevant to reading out MKIDs arrays are an increase in the total bandwidth and the number of resonators that can be read out simultaneously using the SDR and changing the software to optimally measure the resonator signal in direction of maximum signal to noise in real time [85].

6.3 Outlook

A second engineering run is being planned in 2008 with 36 element, 4 color array. With the above changes in design we are anticipating a background limited performance for all the four frequency bands. The larger scale designs will require changing to focal plane architecture in which pixels are fabricated in octants and each octant is readout using a single feedline. Each feedline will require its own HEMT amplifier and a pair of co-axial cables, but will allow greater flexibility in terms of readout - resonance frequency design, and digital readout [14]. This architecture will also be simpler in terms of fabrication issues. With a limited stepper field currently being used for fabrication no more than 4x4 pixels can be accommodated without stitching together different fields of view. New designs will reduce the requirements for fabrication uniformity over large areas.

The previous observing run in March 2007 [14] shows an immense promise for submillimeter pixels made using the MKIDs, planarised multi-slot antenna and the lumped-element bandpass filters. While there still remain technical challenges that need to be overcome, it is to be expected that this technology will play a vital role in astronomical instrumentation and discoveries in the future.

REFERENCES

[1] J. D. Kraus, *Radio Astronomy* (McGraw–Hill: New York, 1966).

[2] J. L. Steinberg and J. Lequeux, *Radio Astronomy* (McGraw–Hill: New York, 1963).

[3] A. Unsld and B. Baschek, *The New Cosmos: An Introduction to Astronomy and Astrophysics*, fifth ed. (Springer, 2001).

[4] J. Carlstrom and J. Zmuidzinas, "Millimeter and submillimeter techniques,", in *Review of Radio Science 1993–1996*, edited by W. R. Stone pp. 839–882 Oxford University Press 1996.

[5] J. Zmuidzinas and P. Richards, "Superconducting detectors and mixers for millimeter and submillimeter astrophysics," *Proc. IEEE* **92**, 1597 (2004).

[6] Atacama Large Millimeter Array
URL: http://en.wikipedia.org/wiki/Atacama_Large_Millimeter_Array.

[7] CCAT Review, URL: http://www.submm.caltech.edu/∼sradford/ccat//mtg a/2007/2007-07-waterloo/07-Fich.pdf, 2007.

[8] H. Dole, G. Lagache, J. Puget, K. Caputi, N. Fernandez-Conde, E. L. Floc'h, C. Papovich, P. Perez-Gonzalez, G. Rieke, and M. Blaylock, "The cosmic infrared background resolved by Spitzer – Contributions of mid-infrared galaxies to the far-infrared background," *AA* **451**, 417 (2006).

[9] M. Birkinshaw, "The Sunyaev-Zel'dovich Effect," *PhysRep* **310**, 97 (1999).

[10] S. C. Chapman, A. W. Blain, I. Smail, , and R. J. Ivison, "A Redshift Survey of the Submillimeter Galaxy Population," *APJ* **622**, 772796 (2005).

[11] C. M. Baugh, C. G. Lacey, C. S. Frenk, G. L. Granato, L. Silva, A. Bressan, A. J. Benson, and S. Cole, "Can the faint submillimetre galaxies be explained in the Λ cold dark matter model?," *MNRAS* **356**, 1191 (2005).

[12] J. Siegrist, Overviews of SZ Effect, Dark Matter
URL: http://supernova.lbl.gov/ evlinder/SZetc.pdf, 1999.

[13] P. Coles and F. Luchin, *COSMOLOGY: The Origin and Evolution of Cosmic Structure* (John Wiley and Sons, Ltd., 2002).

[14] J. Schlaerth, A. Vayonakis, P. Day, J. Glenn, S. Golwala, S. Kumar, H. LeDuc, B. Mazin, J. Vaillancourt, and J. Zmuidzinas, "A millimeter and submillimeter kinetic inductance detector," in *Low Temperature Detectors* 2007, in press.

[15] J. Glenn, J. Bock, G. Chattopadhyay, S. F. Edgington, A. E. Lange, J. Zmuidzinas, P. D. Mauskopf, B. Rownd, and L. Yuen, "BOLOCAM: a millimeter–wave bolometric camera," *Proc. SPIE* **3357**, 326 (1998).

[16] C. D. Dowell, C. A. Allen, S. Babu, M. M. Freund, M. B. Gardner, J. Groseth, M. Jhabvala, A. Kovacs, D. C. Lisa, J. S. HarveyMoseley, T. G. Phillips, R. Silverberg, G. Voellmer, , and H. Yoshida, "SHARC II: a Caltech Submillimeter Observatory facility camera with 384 pixels," *Proc. SPIE* **4855**, 73 (2002).

[17] W. S. Holland, C. R. Cunningham, W. K. Gear, T. Jeness, K. Laidlaw, J. F. Lightfoot, and E. I. Robson, "SCUBA: a submillimeter camera operating on the James Clerk Maxwell Telescope," in *Advanced Technology MMW, Radio, and Terahertz Telescopes*, edited by T. G. Phillips volume 3357 pp. 305–318 1998.

[18] J. Williams, J. Aguirre, J. Bally, J. Glenn, N. Evans, M. Nordhaus, J. Walawender, E. Mills, and R. Chamberlin, "Anomalous low-temperature thermal properties of glasses and spin glasses," *AAS* **210** (2007).

[19] A sub-millimetre survey of the Galactic Plane
URL: http://www.astro.keele.ac.uk/ ae/index.html.

[20] S. C. Chapman, A. W. Blain, R. J. Ivison, and I. R. Smail, "A median redshift of 2.4 for galaxies bright at submillimetre wavelengths," *Nature* **422**, 695 (2003).

[21] G. Laurent, J. Aguirre, J. Glenn, P. Ade, J. Bock, S. Edgington, A. Goldin, S. Golwala, D. Haig, A. Lange, P. Maloney, P. Mauskopf, H. Nguyen, P. Rossinot, J. Sayers, and P. Stover, "The Bolocam Lockman Hole Millimeter-Wave Galaxy Survey: Galaxy Candidates and Number Counts," *Astrophysical Journal* **623**, 742 (2005).

[22] E. Komatsu, T. Kitayama, Y. Suto, M. Hattori, R. Kawabe, H. Matsuo, S. Schindler, and K. Yoshikawa, "Submillimeter Detection of the Sunyaev-Zeldovich Effect toward the Most Luminous X-Ray Cluster at z = 0.45," *Astrophysical Journal* **516**, L1 (1999).

[23] J. Glenn, "Internal Communication,", 2007.

[24] K. D. Irwin and K. W. Lehnert, "Microwave SQUID multiplexer," *Appl. Phys. Lett.* **85**, 2107 (2004).

[25] J. E. Mooij, T. P. Orlando, L. Levitov, L. Tian, C. H. van der Wal, and S. Lloyd, "Josephson Persistent-Current Qubit," *Science* **285**, 1036 (1999).

[26] A. Wallraff, D. I. Schuster, A. Blais, L. Frunzio, R.-S. Huang, J. Majer, S. Kumar, S. M. Girvin, and R. J. Schoelkopf, "Circuit quantum electrodynamics: Coherent coupling of a single photon to a Cooper pair box," *Nature* **431**, 162 (2004).

[27] B. A. Mazin, *Microwave kinetic inductance detectors*, PhD thesis Caltech 2004.

[28] P. K. Day, H. G. LeDuc, B. A. Mazin, A. Vayonakis, and J. Zmuidzinas, "A broadband superconducting detector suitable for use in large arrays," *Nature* **425**, 817 (2003).

[29] J. Lee, W. Oliver, T. Orlando, and K. Berggren, "Resonant Reasout of a Persistent Current Qubit," *ASC* **15**, 841 (2005).

[30] D. R. Schmidt, K. W. Lehnert, A. M. Clark, W. D. Duncan, K. D. Irwin, N. Miller, and J. N. Ullom, "A superconductor–insulator–normal metal bolometer with microwave readout suitable for large-format arrays," *Appl. Phys. Lett.* **86**, 053505 (2005).

[31] B. A. Mazin, M. E. Eckart, B. Bumble, S. Golwala, P. K. Day, J. Zmuidzinas, and F. A. Harrison, "A Position Sensitive X-ray Spectrophotometer using Microwave Kinetic Inductance Detectors," *Appl. Phys. Lett.* **89**, 222507 (2006).

[32] B. Abdo, E. Arbel-Segev, O. Shtempluck, and E. Buks, "Escape rate of metastable states in a driven NbN superconducting microwave resonator," *JAP* **101**, 083909 (2007).

[33] B. Yurke and E. Buks, "Performance of cavity-parametric amplifiers, employing Kerr nonlinearites, in the presence of two-photon loss,", arXiv.org:quant-ph/0505018 2005.

[34] E. Abrel-Segev, B. Abdo, O. Shtempluck, E. Buks, and B. Yurke, "Prospects of employing superconducting stripline resonators for studying the dynamical Casimir effect experimentally," *PLA* **370**, 202 (2007).

[35] D. I. Schuster, A. A. Houck, J. A. Schreier, A. Wallraff, J. M. Gambetta, A. Blais, L. Frunzio, J. Majer, B. R. Johnson, M. H. Devoret, S. M. Girvin, and R. J.

Schoelkopf, "Resolving photon number states in a superconducting circuit," *Nature* **445** (2007).

[36] R. H. Koch, G. A. Keefe, F. P. Milliken, J. R. Rozen, C. C. Tsuei, J. R. Kirtley, and D. P. DiVincenzo, "Experimental Demonstration of an Oscillator Stabilized Josephson Flux Qubit," *PRL* **96**, 127001 (2006).

[37] P. Rabl, D. DeMille, J. M. Doyle, M. D. Lukin, R. J. Schoelkopf, and P. Zoller, "Hybrid Quantum Processors: Molecular Ensembles as Quantum Memory for Solid State Circuits," *Phys. Rev. Lett.* **97** (2006).

[38] A. Andr, D. DeMille, J. M. Doyle, M. D. Lukin, S. E. Maxwell, P. Rabl, R. J. Schoelkopf, and P. Zoller, "A coherent all-electrical interface between polar molecules and mesoscopic superconducting resonators," *Nature Physics* **2** (2006).

[39] M. J. Myers, W. Holzapfel, A. T. Lee, R. O'Brient, P. L. Richards, H. T. Tran, P. Ade, G. Engargiola, A. Smith, and H. Spieler, "An antenna-coupled bolometer with an integrated microstrip bandpass filter," *Applied Physics Letters* **86**, 114103 (2005).

[40] B. A. Mazin, P. K. Day, J. Zmuidzinas, and H. G. LeDuc, "Multiplexable Kinetic Inductance Detectors," in *Ninth International Workshop on Low Temperature Detectors*, edited by F. S. Porter, D. McCammon, M. Galeazzi, and C. K. Stahle volume 605 of *AIP Conf. Proc.* pp. 309–312 AIP: New York 2002.

[41] J. Zmuidzinas, B. Mazin, A. Vayonakis, P. Day, and H. G. LeDuc, "Multiplexable Kinetic Inductance Detectors," in *Proceedings far–IR, sub–mm, and mm detector workshop*, edited by J. Wolf, J. Farhoomand, and C. R. McCreight volume NASA CP/211408 2002.

[42] B. A. Mazin, P. K. Day, H. G. Leduc, A. Vayonakis, and J. Zmuidzinas, "Superconducting Kinetic Inductance Photon Detectors," *Proc. SPIE* **5166** (2002), in press.

[43] M. E. Eckart, *Measurements of X-ray Selected AGN and Novel Superconducting X-ray Detectors*, PhD thesis Caltech 2007.

[44] J. Gao, J. Zmuidzinas, B. A. Mazin, P. K. Day, and H. G. LeDuc, "Noise Properties of Superconducting Coplanar Waveguide Microwave Resonators," *Appl. Phys. Lett.* **90**, 817 (2007).

[45] J. Martinis, K. Cooper, R. McDermott, M. Steffen, M. Ansmann, K. Osborn, K. Cicak, S. Oh, D. Pappas, R. Simmonds, and C. Yu, "Decoherence in Josephson Qubits from Dielectric Loss," *Phys. Rev. Lett.* **95** (2005).

[46] S. Hunklinger, W. Arnold, S. Stein, R. Nava, and K. Dransfeld, "Saturation of the ultrasonic absorption in vitreous silica at low temperatures," *Phys. Lett. A* **42**, 253 (1972).

[47] M. von Schickfus, S. Hunklinger, and L. Pich, "Anomalous Dielectric Dispersion in Glasses at Low Temperatures," *Phys. Rev. Lett.* **35**, 876 (1975).

[48] B. D. Laikhtman, "General theory of spectral diffusion and echo decay in glasses," *Phys. Rev. B* **31**, 490 (1985).

[49] W. A. Phillips, "Two–level states in glasses," *Rep. Prog. Phys.* **50**, 1657 (1987).

[50] Model Kelvinox 25 Dilution Refrigerator, Oxford Cryosystems Ltd. URL: www.lakeshore.com.

[51] Model RX-202A-CD RuO_2 thermometer, Lake Shore Cryotronics, Inc. URL: www.lakeshore.com.

[52] Model 370 AC resistance bridge, Lake Shore Cryotronics, Inc. URL: www.lakeshore.com.

[53] Model MG3692A microwave synthesizer, Anritsu Corp. URL: www.us.anritsu.com.

[54] Model FS725 rubidium frequency standard, Stanford Research Systems, Inc. URL: www.thinksrs.com.

[55] D. C. Mattis and J. Bardeen, "Theory of the anomalous skin effect in normal and superconducting metals," *Phys. Rev.* **111**, 412 (1958).

[56] W. Mason and R. Thurston, *Physical Acoustics : Principles and Methods*volume 12 (Academic Press, New York; San Francisco; London, 1976).

[57] J. Gao, J. Zmuidzinas, B. A. Mazin, P. K. Day, and H. G. Leduc, "Experimental study of the kinetic inductance fraction of superconducting coplanar waveguide," *Nucl. Instrum. Methods Phys. Res., Sect. A* **559**, 585 (2006).

[58] J. Martinis, private communication 2007.

[59] ACBAR , URL: http://cosmology.berkeley.edu/group/swlh/acbar/.

[60] J. H. Goldstein, P. A. R. Ade, J. J. Bock, J. R. Bond, C. Cantalupo, C. R. Contaldi, M. D. Daub, W. L. Holzapfel, C. Kuo, A. E. Lange, M. Lueker, M. Newcomb, J. B. Peterson, D. Pogosyan, J. E. Ruhl, M. C. Runyan, and E. Torbet, "Estimates of Cosmological Parameters Using the Cosmic Microwave Background Angular Power Spectrum of ACBAR," *APJ* **599**, 773 (2003).

[61] C. Kuo, P. Ade, J. Bock, C. Cantalupo, M. Daub, J. Goldstein, W. Holzapfel, A. Lange, M. Lueker, M. Newcomb, J. Peterson, J. Ruhl, M. Runyan, and E. Torbet, "High-Resolution Observations of the Cosmic Microwave Background Power Spectrum with ACBAR," *Astrophysical Journal* **600**, 32 (2004).

[62] A. Goldin, J. Bock, H. Leduc, A.Lange, A. Vayonakis, and J. Zmuidzinas, "High-Directivity Planar Multi-slot Antenna Arrays for Sensitive Imaging at Millimeter Wavelengths,".

[63] T. Buttgenbach, "An Improved Solution for Integrated Array Optics in Quasi-Optical mm and Submm Receivers: the Hybrid Antenna," *MTT* **41** (1993).

[64] P. A. R. Ade, G. Pisano, C. Tucker, and S. Weaver, "A review of metal mesh filters," in *Millimeter and Submillimeter Detectors and Instrumentation for Astronomy III. Edited by Zmuidzinas, Jonas; Holland, Wayne S.; Withington, Stafford; Duncan, William D.. Proceedings of the SPIE, Volume 6275, pp. 62750U (2006).* 2006.

[65] A. Vayonakis, H. Leduc, C. Luo, and J. Zmuidzinas, "Precision Measurements of the Millimeter Wave properties of Superconducting Thin-Film Microstrip Lines,".

[66] M. C. Runyan, P. A. R. Ade, R. S. Bhatia, J. J. Bock, M. D. Daub, J. H. Goldstein, C. V. Haynes, W. L. Holzapfel, C. L. Kuo, A. E. Lange, J. Leong, M. Lueker, M. Newcomb, J. B. Peterson, C. Reichardt, J. Ruhl, G. Sirbi, E. Torbet, C. Tucker, A. D. Turner, and D. Woolsey, "ACBAR: The Arcminute Cosmology Bolometer Array Receiver," *APJS* **149**, 265 (2003).

[67] SUPERMIX URL: http://www.submm.caltech.edu/supermix/.

[68] D. M. Pozar, *Microwave Engineering* (John Wiley and Sons Inc., c1998, 1998).

[69] A. Vayonakis, "Internal Communication,", 2006.

[70] ZEMAX Development Corporation URL: http://www.zemax.com/.

[71] A. Vayonakis, "Internal Communication,", 2002.

[72] J. Zmuidzinas, "Internal Communication,", 2006.

[73] J. Gao, "Internal Communication,", 2003.

[74] E. Serabyn, E. Weisstein, D. Lis, and J. R. Pardo, "Submillimeter FTS Measurements of Atmospheric Opacity above Mauna Kea," *Applied Optics* **37**, 2185 (1998).

[75] R. F. Silverberg, B. Campano, T. C. Chen, E. Cheng, D. A. Cottingham, T. M. Crawford, T. Downes, F. M. Finkbeiner, D. J. Fixsen, D. Logan, S. S. Meyer, T. Perera, E. H. Sharp, and G. W. Wilson, "A bolometer array for the SPEctral Energy Distribution (SPEED)Camera," *Proc. SPIE* **5498** (2004).

[76] R. E. Collins, *Foundations of Microwave Engineering* (New York : IEEE Press, c2001, 2001).

[77] Agilent Advanced Design System
URL: http://eesof.tm.agilent.com/products/ads_main.html.

[78] S. S. Mohan, M. del Mar Hershenson, S. P. Boyd, and T. H. Lee, "Simple accurate expressions for planar spiral inductances," *IEEE Journal of Solid-State Circuits* **34**, 1419 (1999).

[79] SONNET Software Inc. URL: http://www.sonnetusa.com/.

[80] A. Kerr, Surface Impedance of Superconductors and Normal Conductors in EM Simulators URL: http://www.alma.nrao.edu/memos/, 1999.

[81] R. Matick, *Transmission Lines for Digital and Communication Networks* (McGraw-Hill, 1969).

[82] M. Bin, D. J. Benford, M. C. Gaidis, T. Buttgenbach, J. Zmuidzinas, E. Serabyn, and T. Phillips, "A large throughput high resolution Fourier Transform

Spectrometer for submillimeter applications," *International journal of infrared and millimeter waves* **20**, 383 (1999).

[83] J. Glenn, J. Bock, S. Edgington, A. Lange, J. Zmuidzinas, P. Mauskopf, B. Rownd, L. Yuen, and P. Ade, "A Millimeter-Wave Bolometric Camera," volume 3357 Proc. SPIE. vol. 3357 1998.

[84] J. S. Ward, *Observations of carbon monoxide in the starburst galaxy M82 with a 690 GHz wide spectral bandwidth receiver*, PhD thesis Caltech 2001.

[85] B. A. Mazin, P. K. Day, K. D. Irwin, C. D. Reintsema, and J. Zmuidzinas, "Digital Readouts for large microwave low-temeprature detector arrays," *Nuclear Instruments and Methods in Physics Research* **559**, 799 (2006).